Optical properties of ZnGeP2 and CdGeP2.

Miller, Alan

Award date:
1974

Awarding institution:
University of Bath

Optical Properties of $ZnGeP_2$ and $CdGeP_2$

submitted by Alan Miller

for the degree of Ph.D

of the University of Bath

1974

Copyright

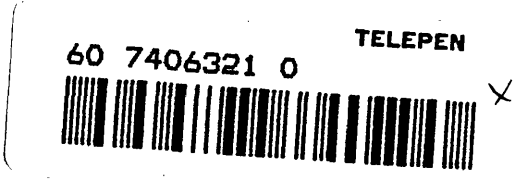

 Alan Miller

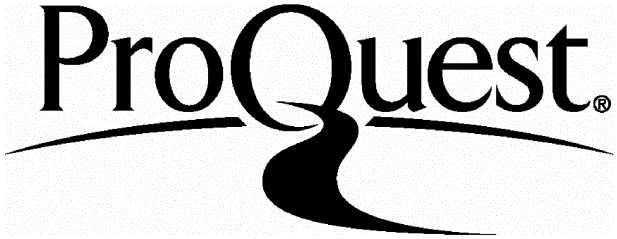

74-0

Declaration

This is to certify that

Alan Miller

has carried out the research reported in this thesis under my supervision between 1st October 1971 and 30th September 1974.

W.C. Clark B.Sc. Ph.D. M.Inst.P.
University of Bath, 1974.

W. C. Clark

Abstract

Single crystals of the ternary chalcopyrite semiconductors, $ZnGeP_2$ and $CdGeP_2$, space group $I\bar{4}2d$, were grown by slow cooling in a 20 mol % lead solution. Room temperature lattice parameters were determined for both compounds, and the variations of the lattice parameters with temperature up to the melting point of $ZnGeP_2$ were studied. Hall effect and resistivity measurements showed $ZnGeP_2$ to be p-type while $CdGeP_2$ changed from p-type to n-type conduction at $11^{o}C$. Polarised infrared reflectivity measurements were made in the range 40 to 700 cm^{-1}. The spectra were analysed using both classical dispersion theory and Kramers-Krönig integration, yielding four modes in $ZnGeP_2$ and five in $CdGeP_2$ with E irreducible representation and two modes in both materials with B_2 irreducible representation. Raman measurements in the backscattering configuration using a Krypton laser determined all thirteen group theoretically predicted modes in $CdGeP_2$ while two were unobserved in $ZnGeP_2$. These modes were interpreted in terms of the atomic motions of the III-V zinc blende analogues. The fundamental absorption edges of the two compounds were studied at room and liquid nitrogen temperatures, and the lowest direct transitions were determined at room temperature by electroreflectance. The polarisation modulation technique was also used to study the higher energy structure at 5K and 300K. It was deduced that $CdGeP_2$ has a direct gap at 1.7eV, while $ZnGeP_2$ is either indirect or "pseudo-direct" at about 2.0eV.

Acknowledgements

I would like to thank Dr. W.C. Clark for his continual help and encouragement throughout this work and Professor S.H. Ayliffe for the provision of laboratory facilities. The Science Research Council is acknowledged for financial support.

My thanks are also due to Mr. R.G. Humphreys, Mr. R.C.J. Draper, Mr. B. Chapman and Dr. B.R. Pamplin for many helpful and stimulating discussions and much experimental assistance. The technical assistance of Mr. B. Ring and his staff is gratefully acknowledged, in particular Mr. E. Lambson and Miss W. Horler.

Much of the work of this thesis was carried out at other establishments, so I must thank Professor S.D. Smith of Heriot-Watt University, Edinburgh and Professor M. Cardona of the Max Planck Institut für Festkörperforschung, Stuttgart for their invitations and the hospitality received. It is a pleasure to acknowledge Dr. G.D. Holah, Dr. C.R. Pidgeon and Mr. M. Bettini for arranging these visits and for their assistance in carrying out the experiments.

I am particularly indebted to Dr. H. Montgomery of Edinburgh University for invaluable help in the group theory of chalcopyrite crystals. I also benefited from fruitful discussions with Mr. W.H. Koschel and Dr. J. Baars at the Institut für Angewandte Festkörperphysik der Fraunhofer-Gesellschaft, Freiburg.

My thanks also go to June McGregor for typing the manuscript.

Contents

Figure Captions

List of Tables

CHAPTER 1 Introduction

1.1 Derivation of the II-IV-V_2 compounds

Semiconductors with crystal lattices deriving from the diamond structure have become a much studied group of materials since active electronic devices were first made from silicon and germanium in the late 1940's (1). The semiconducting properties of these materials originate in the tetrahedral bonding of the diamond structure, which consists of two interpenetrating face centred cubic lattices, with a relative displacement of $\left[\frac{1}{4}, \frac{1}{4}, \frac{1}{4}\right]$. Silicon, germanium and tin are found in this structure, while binary III-V compounds give twelve compounds with the sphalerite or zinc blende structure in which the group III cations and the group V anions occupy each of the interpenetrating f.c.c. sub-lattices of the diamond structure, figure 1.1. Indium antimonide was the first of these compounds to show semiconducting properties in 1950 (2) (3), and experiments since then have shown that in general the properties of III-V compounds are similar to their group IV parents. III-V nitrides take the closely related wurtzite structure favoured by more ionic compounds, while II-VI compounds have either the wurtzite or the zinc blende structures.

The tetrahedral bonding of all these compounds derives from the predominantly covalent nature of the bonds. Group IV atoms have the quadrivalent sp^3 electron configuration in the crystalline state, and combine with other atoms in four tetrahedral bonds with wave-functions which are linear combinations of the spherically symmetric s- like states, and the three directional p- like states, p_x, p_y, p_z. Electron overlap is large in this configuration, and so the bonds are strong and directional at the tetrahedral angle of 109.47°.

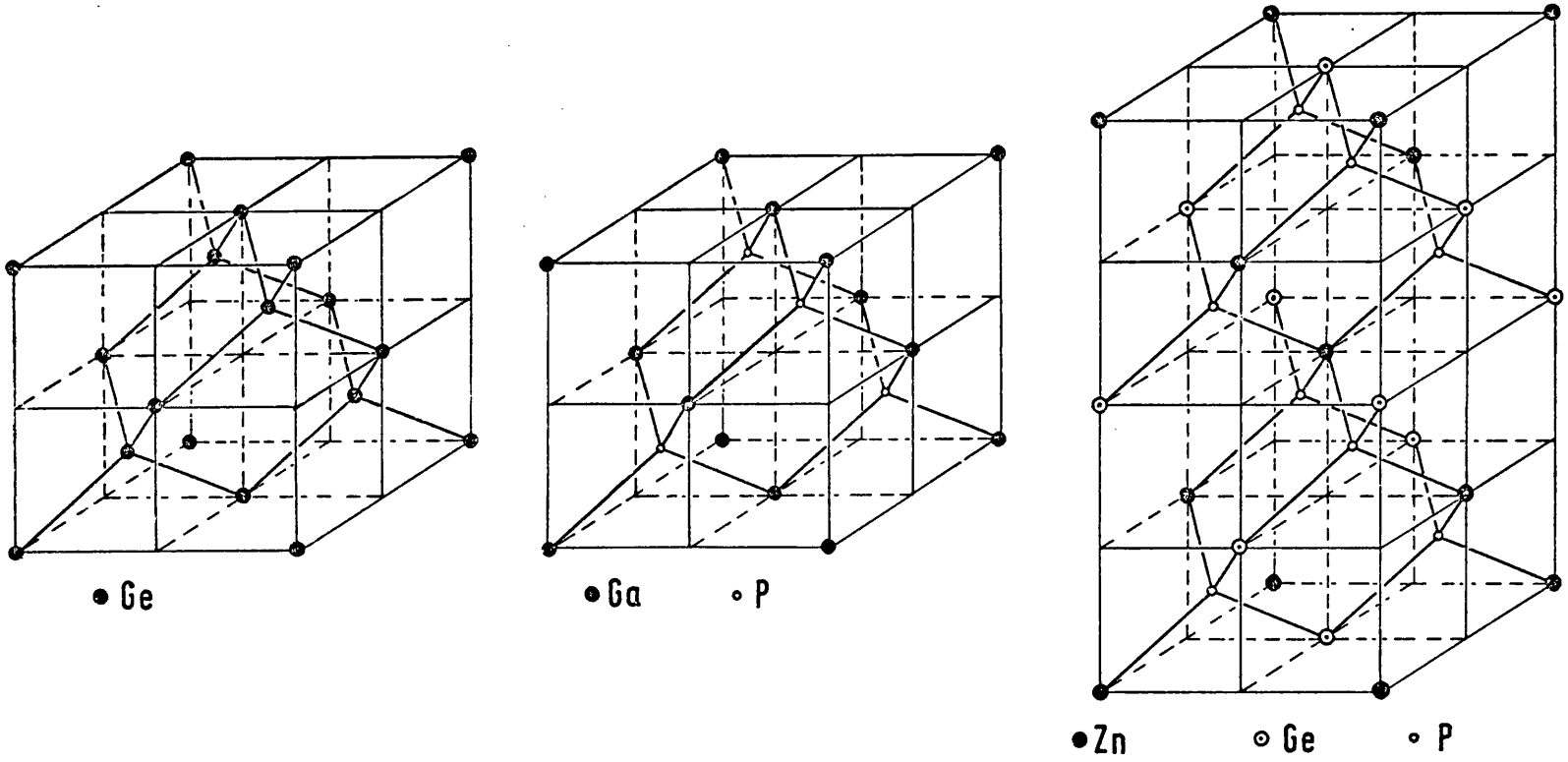

Figure 1.1 (a) Diamond, (b) Zinc Blende, (c) Chalcopyrite

Table 1.1 Some basic properties of II-IV-V_2 compounds

	a (Å)	c	melting points (^{o}C)	band gaps* (eV)	elec.type	d_{14}/d_{14}(GaAs)
$ZnSiP_2$	5.399	10.435	1370	2.07(p)	n & p	-
$ZnSiAs_2$	5.611	10.886	1096	1.74(p)	p	0.81
$ZnGeP_2$	5.464	10.708	1025	1.99(p)	p	0.83
$ZnGeAs_2$	5.672	11.153	850	1.15(d)	p	-
$ZnSnP_2$	5.651	11.302	930	1.66(d)	p	-
$ZnSnAs_2$	5.852	11.703	775	0.73(d)	p	-
$CdSiP_2$	5.680	10.431	1120	~2.1 (p)	n	-
$CdSiAs_2$	5.885	10.881	850	1.55(d)	p	-
$CdGeP_2$	5.741	10.770	795	1.72(d)	n & p	1.21
$CdGeAs_2$	5.943	11.216	670	0.57(d)	n & p	2.62
$CdSnP_2$	5.902	11.512	570	1.17(d)	n & p	-
$CdSnAs_2$	6.094	11.918	593	0.26(d)	n & p	-

* d = direct gap ; p = pseudodirect

The III-V and II-VI binary compounds derive from the group IV diamond structure compounds according to the Grimm-Somerfeld rule (4). This states that a related structure may exist if the average number of valence electrons per atom is the same as for the parent. In this case there are four electrons per atom. The derivation process is called cross substitution and can be extended to predict other groups of materials such as II-IV-V_2 and I-III-VI_2 compounds in which cross substitution is made on the metal ions of III-V and II-VI compounds respectively. Hahn et al. (5) synthesised the first I-III-VI_2 samples with chalcopyrite structure, figure 1.1, in 1953. Goodman showed that II-IV-V_2 compounds should exist and prepared several of them in 1958 (6,7). To date, about twenty four II-IV-V_2 compounds have been prepared. Table 1.1 lists the most studied of these along with some of their basic properties.

Several reviews (8,9,10,11) and bibliographies (12,13) have been written and there is a recent monograph by Shay and Wernick (14) which discusses growth, electronic structure and applications of II-IV-V_2 and I-III-VI_2 compounds.

1.2 Structure

II-IV-V_2 compounds normally crystallise in the chalcopyrite structure, space group $I\bar{4}2d$ (15), shown in figure 1.2. The name chalcopyrite comes from the mineral $CuFeS_2$, but will be used throughout this work to denote the structure. This is similar to the zinc blende structure, but the group II and IV atoms are ordered on the cation sites along the c-axis, giving a tetragonal unit cell. The unit cell would be doubled in volume (c = 2a) if the lengths of the two types of bond were identical, but the difference in the two cations tends to distort the lattice such that the lattice acquires

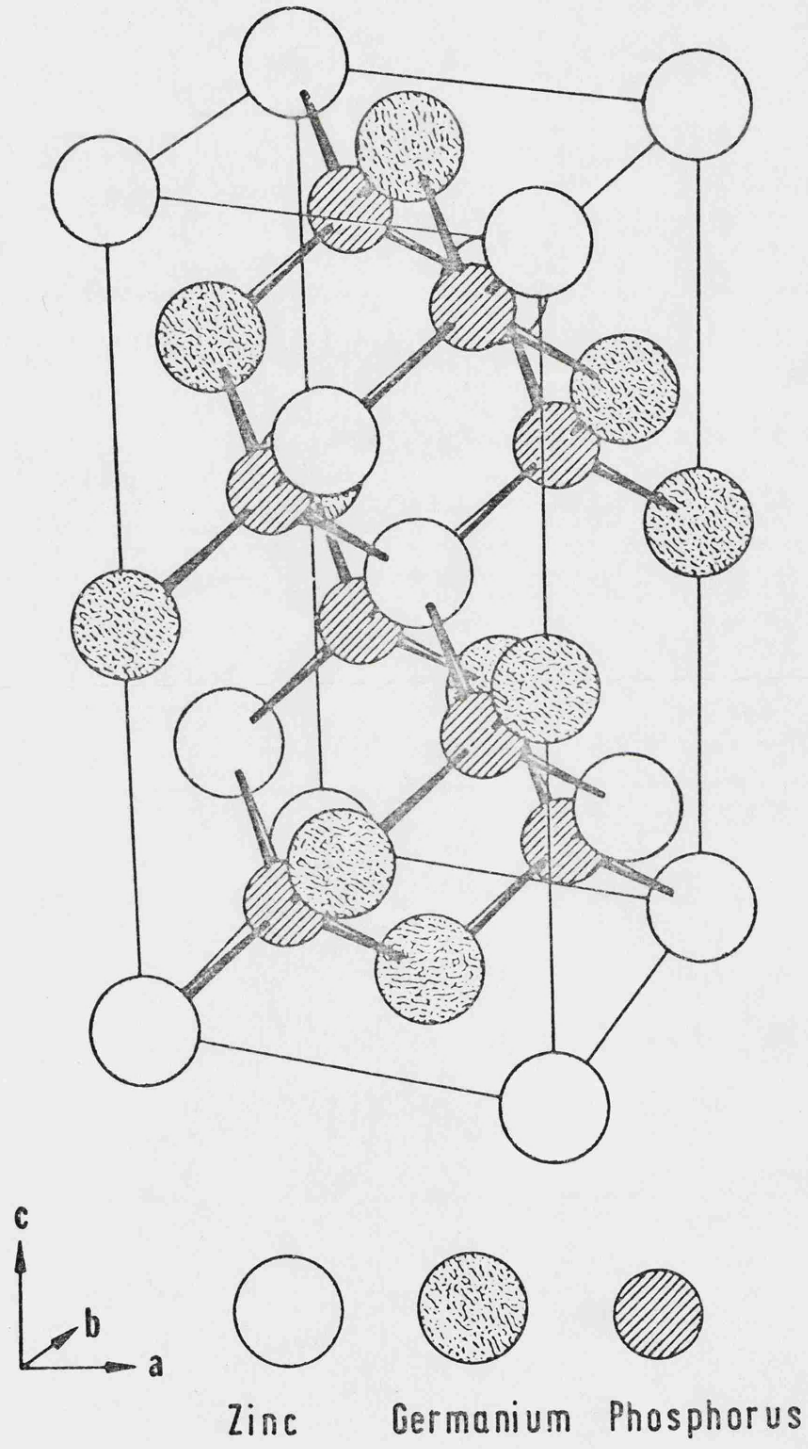

Figure 1.2 Unit cell of chalcopyrite structure

a tetragonal compression in the c-direction given by the parameter, $2 - {}^{c}/_{a}$. This is always positive for II-IV-V_2 compounds.

The effect of a shorter B-C bond length is shown in figure 1.3 (11). In $ZnGeP_2$ for instance, each phosphorus atom is bonded to two germanium and two zinc atoms. Thus, if the phosphorus moves closer to the germanium pair, it remains in the same x-y plane. The result is opposite rotations, τ_A and τ_B about the c-axis centred on zinc or germanium atoms when viewed along $[00\bar{1}]$.

The displacement of the phosphorus is given by $(\frac{1}{4} - x)$, where $\tan \tau_A = (1-4x)/(1+4x)$ and $\tan \tau_B = (4x-1)/(3-4x)$. The x parameters, bond lengths and bond angles have been measured in $ZnSiP_2$ (15), $CdSiP_2$ (16) and $CdGeAs_2$ (17) by Abrahams and Bernstein in an x-ray investigation. This was extended to $ZnGeP_2$ and $ZnSiAs_2$ by Lind and Grant (18), while less precise measurements have been made on $CdGeP_2$(19). The results are shown in Tables 1.2 and 1.3.

These analyses conclude that the BC_4 tetrahedra are very nearly perfect with bond angles close to 109.47° (Table 1.2). Thus, from geometry, the x-parameter can be defined in terms of ${}^{c}/_{a}$ by assuming a perfect tetrahedron,

$$x = \tfrac{1}{2} - \left[\frac{c^2}{32a^2} - \frac{1}{16}\right]^{\frac{1}{2}} \qquad 1.1$$

From this, Abrahams and Bernstein (16) derived expressions for A-C and B-C bond lengths (equations 2.2 and 2.3) and showed that the IV-V bond length is given by,

$$c = \frac{8}{\sqrt{3}} \text{ (B-C)} \qquad 1.2$$

Figure 1.4 shows the agreement which this gives with measured B-C bond lengths in chalcopyrite compounds. Good comparison is found for Ge-P bonds in $ZnGeP_2$ and $CdGeP_2$.

Abrahams and Bernstein also compared measured bond lengths with those calculated from tetrahedral radii given by either Pauling and

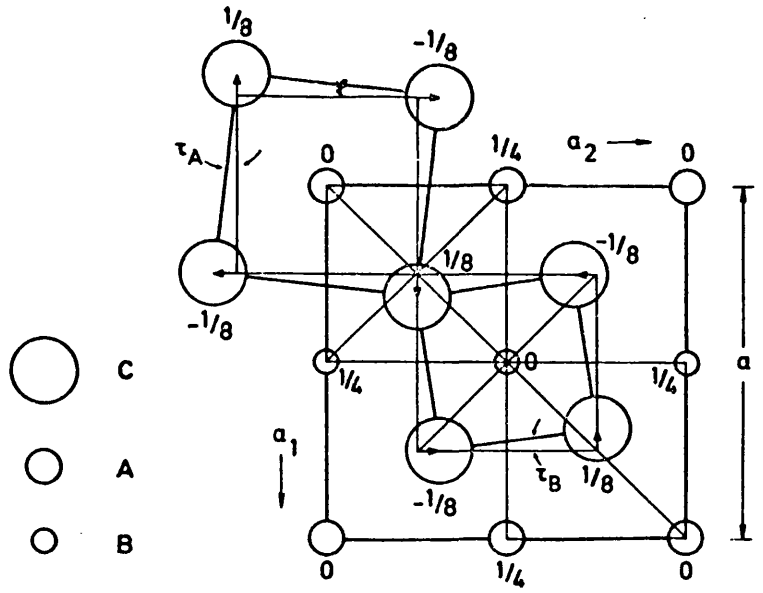

Figure 1.3 Atomic arrangement in the chalcopyrite structure for $x > 1/4$

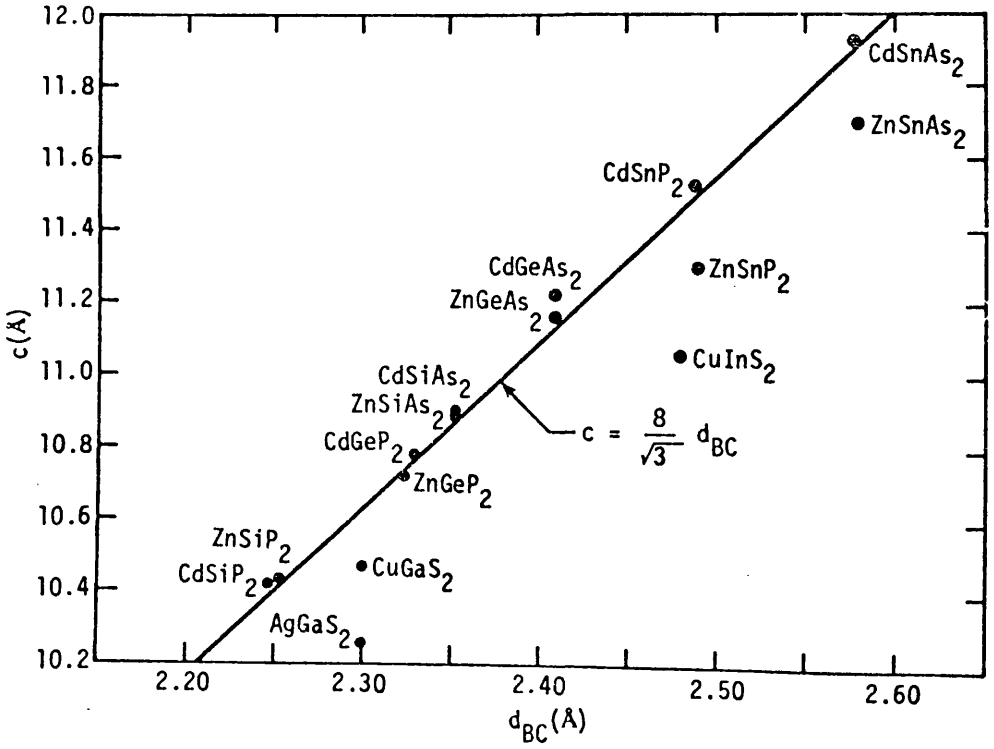

Figure 1.4 Lattice constants c vs. B-C bond lengths.

Table 1.2 Measured bond distances and angles

Distance or Angle	Multiplicity	$ZnGeP_2$ (18)	$CdGeP_2$ (19)	$ZnSiP_2$ (15)	$CdSiP_2$ (16)	$CdGeAs_2$ (17)	$ZnSiAs_2$ (18)
A C_4 tetrahedra							
A - C	4	2.375Å	2.55	2.375	2.561	2.629	2.454
C - C	4	3.856	4.08	3.832	4.064	4.214	3.968
C - C	2	3.924	4.34	3.968	4.407	4.449	4.086
C - A - C	4	108.5°	106.2°	107.6°	105.0°	106.5°	107.9°
C - A - C	2	111.4°	116.3°	113.3°	118.8°	115.6°	112.7°
B C_4 tetrahedra							
B - C	4	2.324Å	2.33	2.254	2.247	2.430	2.352
C - C	4	3.792	3.81	3.684	3.674	3.968	3.842
C - C	2	3.798	3.80	3.674	3.661	3.966	3.837
C - B - C	4	109.3°	109.5°	109.6°	109.7°	109.5°	109.5°
C - B - C	2	109.6°	109.3°	109.3°	109.1°	109.4°	109.3°

Table 1.3 Measured and calculated bond lengths (Å)

	a	c		Meas.	Calc. for perfect tetra.	Calc. from covalent radii(18)
$ZnGeP_2$	5.464*	10.708*	x	0.2582	0.2602	--
			A - C	2.375	2.383	2.353
			B - C	2.324	2.318	2.353
$CdGeP_2$	5.741*	10.770*	x	0.283	0.2821	--
			A - C	2.55	2.549	2.533
			B - C	2.33	2.331	2.353
$ZnSiP_2$	5.399	10.435	x	0.2692	0.2671	--
			A - C	2.375	2.367	2.353
			B - C	2.254	2.259	2.301
$CdSiP_2$	5.680	10.432	x	0.2968	0.2929	--
			A - C	2.561	2.546	2.533
			B - C	2.247	2.258	2.301
$CdGeAs_2$	5.943	11.216	x	0.2785	0.2791	--
			A - C	2.629	2.631	2.630
			B - C	2.430	2.429	2.450
$ZnSiAs_2$	5.606	10.890	x	0.2658	0.2646	--
			A - C	2.454	2.453	2.450
			B - C	2.352	2.358	2.398

* Values obtained in this work - see Chapter 2

All other values taken from references cited in text.

Huggins (20) or Van Vechten and Phillips (21). The latter values give the better results and are listed in Table 1.3, however, the difference between these values and the measured ones indicates that charge transfer plays a significant part in determining the bond lengths. Note that the predicted IV-V bond lengths are consistently too large. This may be explained by the fact that a covalent Ge-P bond in $ZnGeP_2$ will have $^9/_4$ valence electrons, which give a bond with strong directional character, and reduces the bond length compared to that calculated from tetrahedral radii. The Zn-P pairs have only $^7/_4$ electrons, giving the opposite effect.

Phillips (22) compares the trends in the tetragonal compression with the electronegativities of the components derived from his dielectric electronegativity scale (23). The compression may be due to second nearest neighbour cation (A) - cation (B) electronegativity differences. The relation,

$$2 - {}^c/_a = -0.60\chi_A + 0.25\chi_B + 0.15\chi_c + 0.01 \qquad 1.3$$

yields agreement for small distortions.

According to Phillips, the size of the coefficients in eq. 1.3., show that charge transfer to the group II atom produces three times as great an effect on $2 - {}^c/_a$ as charge transfer to group IV and V atoms. The sign of the coefficients show that charge gained by, for instance, germanium and phosphorus, is lost by zinc.

Varae de Alvarez et al. (24) have calculated the charge density contours in $ZnGeP_2$ from ESCA measurements and pseudopotential band structure calculations. Six energy levels were observed down to 14.5eV below the valence band edge. The electron distribution of the upper levels indicate that the Ge-P bond is the stronger covalent bond as expected.

Levine (25) has recently generalised the dielectric description of ionicity developed by Phillips and Van Vechten (26, 27) for $A^N B^{8-N}$ compounds, to materials containing more than one type of bond. Ionicities of the individual bonds in chalcopyrite compounds calculated from bond lengths and macroscopic linear susceptibilities successfully predict the values of the nonlinear optical susceptibilities (28).

The similarity between chalcopyrite and zinc blende structures causes some II-IV-V_2 compounds to undergo a solid state phase transition at high temperatures (29). The zinc blende structure can often be retained by quenching from above the transformation temperature to room temperature. $MgGeP_2$ is always found in the zinc blende form at room temperature (30). Quenching of $CdGeP_2$, $CdGeAs_2$ and $CdSiAs_2$ from the melt can produce an amorphous phase (31).

1.3 Growth and physical properties

Three principle techniques of crystal growth have been used to grow II-IV-V_2 materials. (1) Directional synthesis from stoichiometric amounts of the elements.

Bridgman and Stockbarger methods involve mechanical lowering of a sealed ampoule containing the constituent elements in a temperature gradient through the melting point to provoke nucleation and growth of a single crystal from one end. The directional cooling method has the same effect by simply cooling the material from above the melting point in a temperature gradient. The best method, widely used in the semiconductor industry for growing very high quality crystals, is Czochralski pulling of a seed crystal from the melt. The growth can be precisely controlled and is not constrained by an ampoule. The high vapour pressure of the group V elements has

precluded this method to date.

Crystals with melting points below the softening point of silica have been grown from the melt. These are, $ZnGeP_2$(32), $CdGeP_2$(33), $ZnSiAs_2$(34), $CdGeAs_2$(37), $CdSnAs_2$(36), $ZnSnAs_2$(35) and $ZnGeAs_2$(35).

(2) Vapour transport

Sublimation of the elements or prereacted starting material to a cooler part of an ampoule can produce single crystal growth. Zinc, cadmium, phosphorus and arsenic are all fairly volatile, but the group IV element often has to be transported with the aid of a carrier such as chlorine or iodine. One attempt has been made to grow $ZnSiP_2$ using an open flow system, but only polycrystalline layers were obtained (38). Closed tube systems have grown single crystals of $ZnSiP_2$(39), $CdSiP_2$(40), $ZnGeP_2$(41), $CdGeP_2$(33) and $ZnSiAs_2$(39).

(3) Solution growth

Attempts have been made to grow most II-IV-V_2 compounds by slow cooling from solution in a low melting point metal. Many solvents have been tried with various degrees of success. Mughal (42) has given details of an attempt to use the Czochralski pulling technique for $ZnSiP_2$ growth from solution in tin with boric oxide encapsulation.

Solution growth by slow cooling has been used in this work to grow single crystals of $ZnGeP_2$ and $CdGeP_2$ and will be discussed in detail in Chapter 2.

The crystal morphology of the chalcopyrite crystals is fairly insensitive to the growth method. Growth is invariably reported to be in the $[111]$ direction with {112} and {101} the best developed faces. Solution or vapour transport methods tend to give needle shaped crystals with cross section shown in figure 1.5. Both (112)

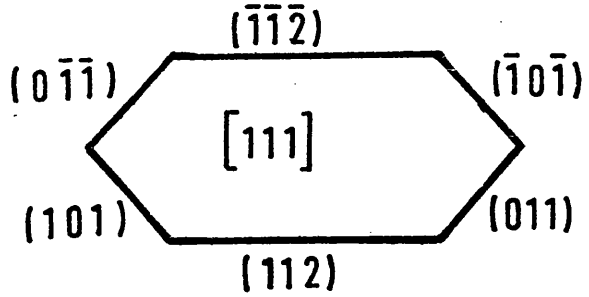

Figure 1.5 Crystal habit

and $(\bar{1}\bar{1}\bar{2})$ faces are not always developed and different growth methods or conditions may favour larger {101} faces than {112}.

The melting points of several II-IV-V_2 compounds are shown in table 1.1. The process of melting is complicated because of the existence of binary phases between the constituents and the high vapour pressure of the group V elements. This leads to incongruent melting points in some of the materials. Variation from stoichiometry is a major problem in the growth. The solubility of group IV elements in II-IV-V_2 compounds is known to be high (43). Solid solutions of III-V and II-IV-V_2 compounds have also been investigated (9).

Another problem of the growth of II-IV-V_2 compounds is the formation of cracks. Borshchevskii reports the absence of cracks in compounds produced in the sphalerite structure by quenching (9). This suggests that cracks may be due to the high temperature phase transition and the anisotropic thermal contraction of the chalcopyrite structure.

1.4 Electrical properties

The electrical properties of II-IV-V_2 compounds have been under active investigation due to the interest in their semiconducting nature and also as a means of crystal purity assessment. Hall effect, conductivity, photoconductivity, photovoltaic and thermoelectric measurements have been made on a variety of the materials.

Most of the compounds only grow as a single conducting type and resist change by introduction of a dopant impurity during growth, suggesting self compensation, perhaps due to deviations from stoichiometry. $ZnGeP_2$ for instance has always been reported as p-type, while $CdGeP_2$ in contrast has been grown both p-type and n-type without intentional doping during growth. Table 1.1 gives the majority carriers for a number of II-IV-V_2 compounds.

Electron mobilities are typically 100cm^2/V.sec. for the high band gap materials, but the low band gap $CdSnAs_2$ has been reported to have an electron mobility of 11,000 cm^2/V.sec. Hole mobilities range from 20 to 1,500 cm^2/V.sec.

The chalcopyrite structure, being noncentrosymmetric, is piezoelectric. Turner has measured coefficients for $ZnGeP_2$(44).

The amorphous phases of $CdGeP_2$, $CdGeAs_2$ and $CdSiAs_2$ have been studied for possible use in switching devices and memory applications and current oscillations have been observed in crystalline $CdSnP_2$ in high electric fields (45, 46).

1.5 Optical properties of II-IV-V_2 compounds

The similarity of the chalcopyrite structure to that of zinc blende gives a good basis for the study of the optical properties of II-IV-V_2 materials. The larger number of compounds possible gives a greater variety of properties than for III-V compounds, and

the approximate doubling of the unit cell along the c-axis introduces several interesting properties which are not observed in III-V compounds.

Since the structure is uniaxial, the optical properties become anisotropic. In the visible region of the spectrum at energies below the band gap, all II-IV-V_2 compounds investigated have shown a positive birefringence (14). It is less obvious that the ordering of the anions gives rise to optical activity. Opposite rotations of plane polarised light are obtained along x and y axes, but the effect is normally screened by the larger birefringence. Optical activity has been studied in $AgGaS_2$ by Hobden (47).

For a study of the absorption region due to lattice vibrations in the far infrared and electronic transitions in the visible region of the spectrum, the Brillouin zone of the chalcopyrite structure must be considered. The chalcopyrite structure consists of two interpenetrating body centred tetragonal lattices, displaced by $\left[a/2,\ 0,\ c/4\right]$. The basis vectors of the primitive cell are shown in figure 1.6 in which only the zinc atoms are shown for clarity,

$$\underline{a}_1 = \tfrac{1}{2}\ (-a.\ a.\ c);\quad \underline{a}_2 = \tfrac{1}{2}\ (a,\ -\ a,\ c);\quad \underline{a}_3 = \tfrac{1}{2}\ \ (a,\ a,\ -c)$$

This gives the basis for the reciprocal lattice,

$$\underline{b}_1 = 2\pi(0,\ \frac{1}{a},\ \frac{1}{c});\quad \underline{b}_2 = 2\pi(\frac{1}{a},\ 0,\ \frac{1}{c});\quad \underline{b}_3 = 2\pi(\frac{1}{a},\ \frac{1}{a},\ 0)$$

which is a face centred tetragonal lattice with unit cell sides of length $4\pi/a$, $4\pi/a$, $4\pi/c$. The Wigner-Seitz cell defines the first Brillouin zone shown as part of figure 1.7. Two chalcopyrite zones are illustrated for comparison with a larger zinc blende Brillouin zone, such that the zone centre, Γ- point of the zinc blende zone coincides with the Γ- point of one of the chalcopyrite zones. The volume of the zinc blende zone is four times that of

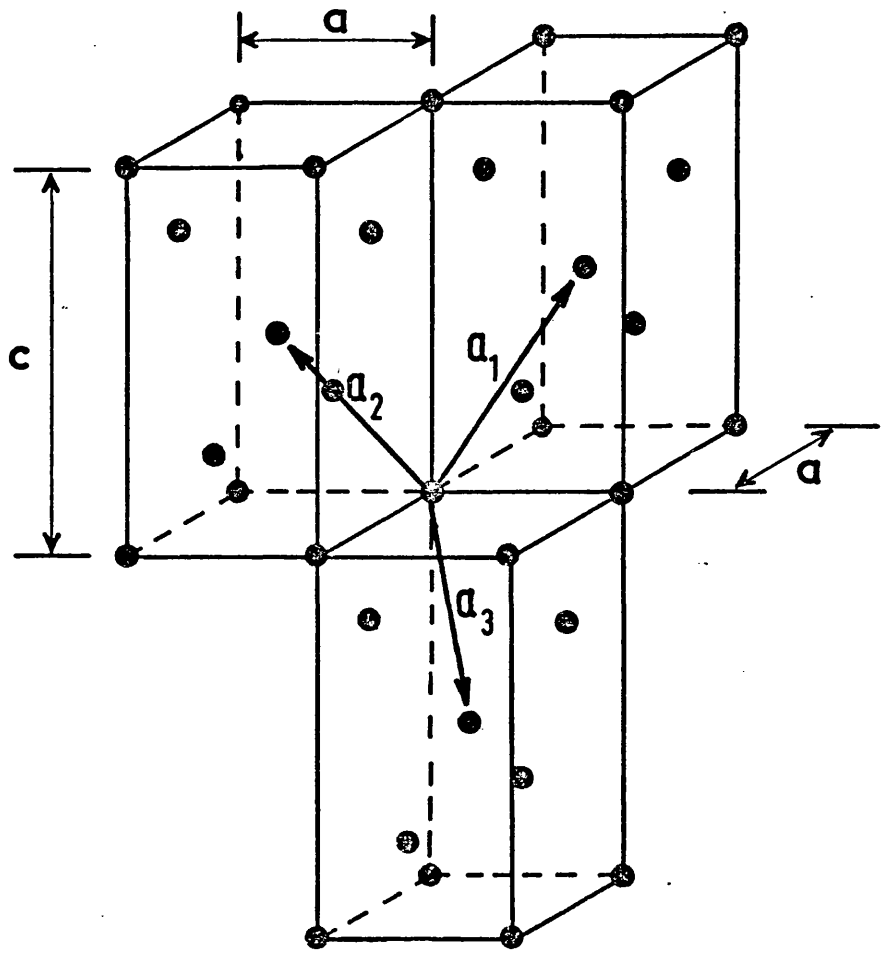

(a) Real lattice

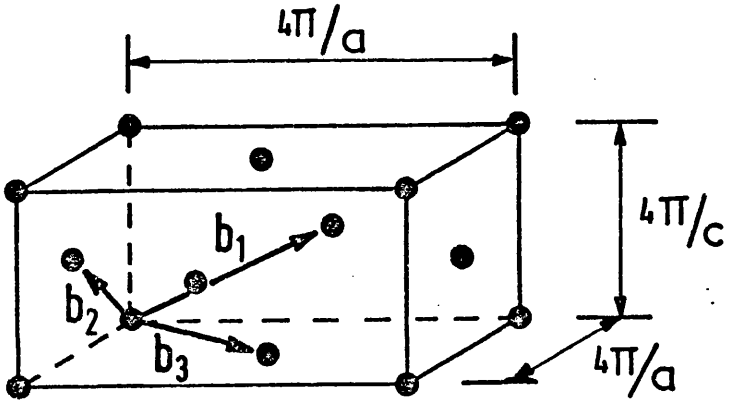

(b) Reciprocal lattice

Figure 1.6 Basis vectors for real and reciprocal lattices

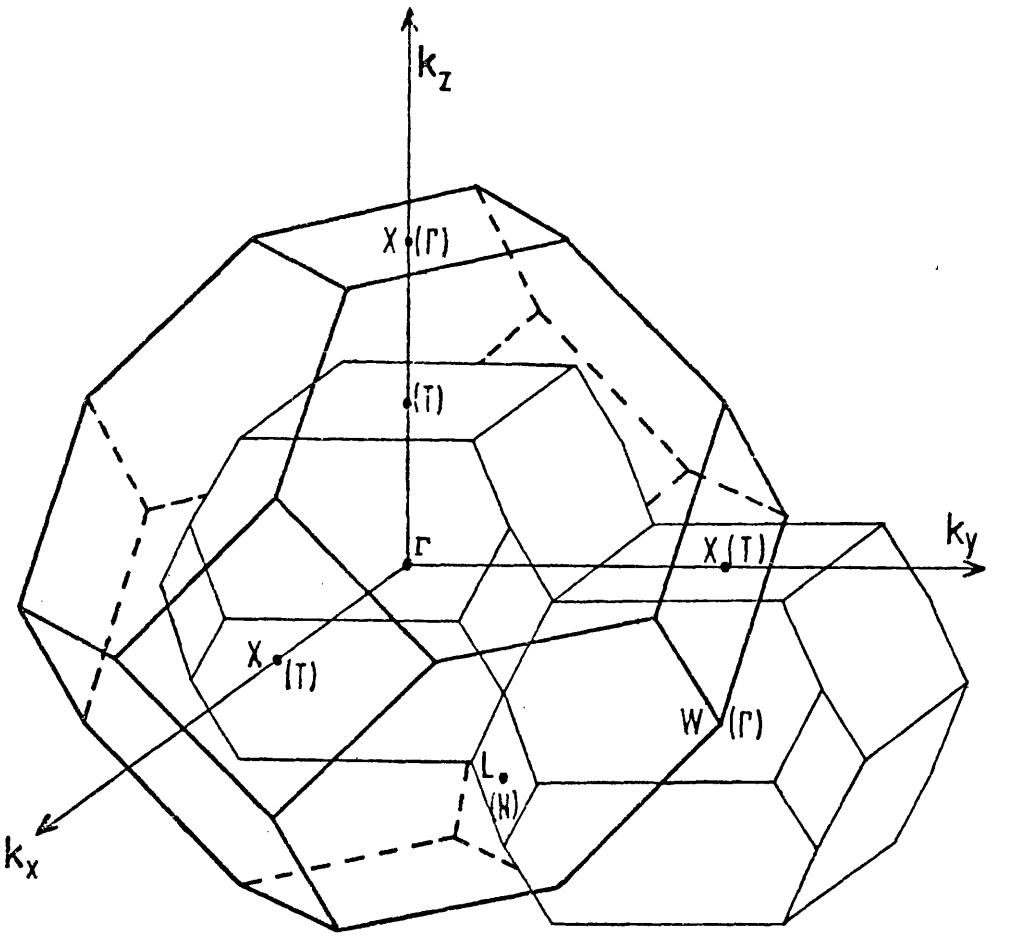

Figure 1.7 Zinc Blende and Chalcopyrite Brillouin zones

the chalcopyrite zone, assuming no tetragonal compression. The main symmetry points of zinc blende are Γ, L, X and W, while those of chalcopyrite are Γ, T and N, shown in parenthesis in figure 1.7.

Some X and W points of zinc blende coincide with Γ-points in either the second chalcopyrite zone shown, or other corresponding zones around the central one. Chaldeshev lists all equivalent symmetry points of the two structures (48, 49). The most important corresponding points are the following,

Zinc Blende	Chalcopyrite
Γ (0,0,0) X (0,0, $2\pi/a$) W (0, $2\pi/a$, π/a) W ($2\pi/a$, 0, π/a)	Γ (0,0,0)
L (π/a, $-\pi/a$, $-\pi/a$) Σ (π/a, π/a, 0)	N (π/a, π/a, 0)
X (0, $2\pi/a$, 0) X ($2\pi/a$, 0,0) Δ (0, 0, π/a)	T (0, 0, π/a)

Infrared radiation only interacts with phonons which have zero wavevector, and produce finite dipole moments due to the relative displacement of positive and negative ions. In III-V compounds, a one phonon absorption band is observed due to the antiphase motions of anions and cations with zero wavevector (50). Chalcopyrite materials should also have this mode of vibration, but in addition, there will be absorption due to phonons which map from the X and W points in zinc blende, to the zone centre in chalcopyrite. This results in a fairly complex absorption spectrum which will be considered in detail in Chapters 3, 4 and 5.

Most work on II-IV-V_2 compounds has concentrated on an analysis of the electronic energy band structure, usually by optical measurements, and interpretation of the result has been made by comparison with the energy band structures of III-V compounds. A first approximation can be made by embedding the band structure of a III-V isoelectronic analogue into the chalcopyrite Brillouin zone. Figure 1.8 shows the band structure calculated for GaP neglecting spin orbit coupling. Mapping X and W points to the zone centre can lead to two different zone centre situations.

If the III-V analogue is a direct band gap material, then the lowest band gap in the corresponding ternary compound will be direct at the zone centre, $\Gamma_{15} - \Gamma_1$. If on the other hand, the III-V compound is indirect with the lowest conduction band minimum in the X-direction, as it is in GaP (X_1 in figure 1.8), then the chalcopyrite zone will have lowest minima at both the Γ and T points. The question then arises as to which of these will be the lower, as one will give a direct gap material, and the other an indirect. One may consider measurements on III-V compounds, compressed along [001], which gives a tetragonal compression similar to that in ternaries. These measurements (187) give the result that the minimum at the X point (0, 0, $^{2\pi}/a$) is moved to lower energy. This corresponds to the zone centre in chalcopyrite, indicating in this case, that the ternary compound will have a direct gap, which has been called pseudo-direct by Shay (53). The strength of a transition to this zone centre band depends on the difference between the two cations, thus the absorption may still be dominated by indirect transitions.

This is the expected situation in the higher band gap II-IV-V_2 compounds, $MgSiP_2$, $ZnGeP_2$, $ZnSiP_2$, $CdSiP_2$ and $ZnSiAs_2$, while the

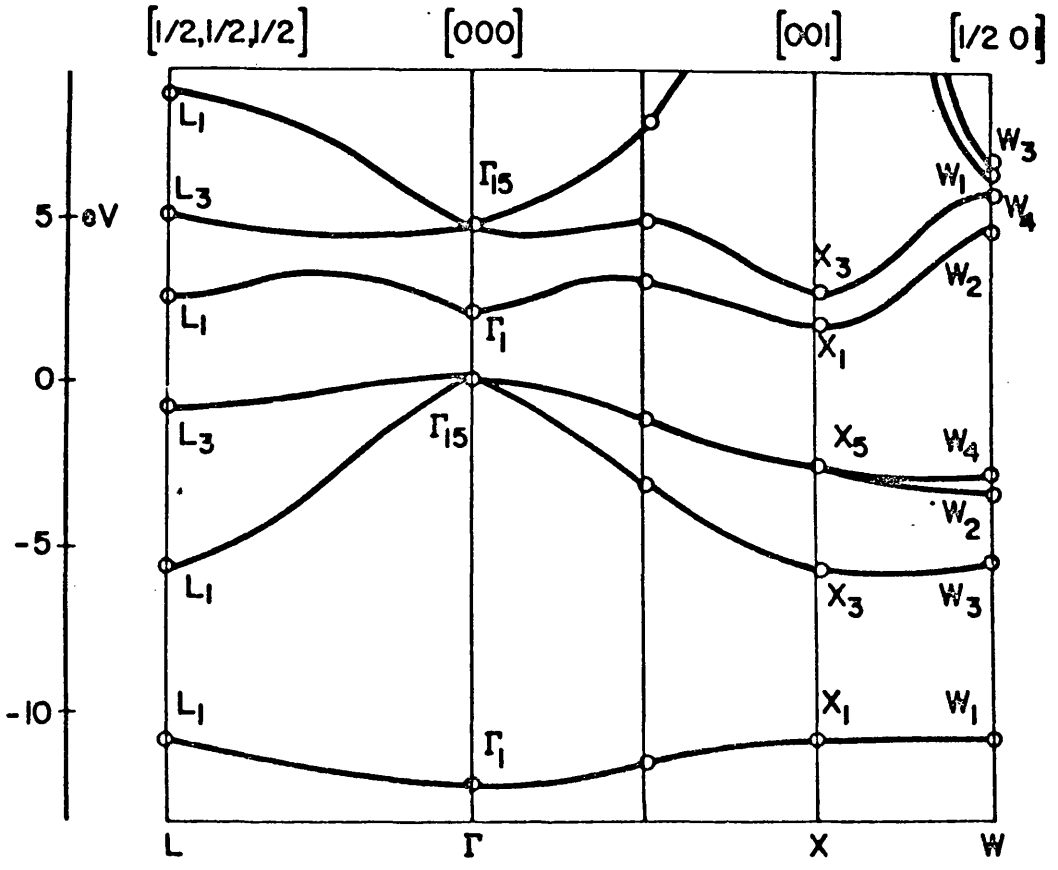

Figure 1.8 Energy band structure of GaP neglecting spin-orbit spitting.

lower band gap compounds, including $CdGeP_2$, will have a direct gap (10).

Direct band gaps should lead to efficient radiative recombination in the infrared region for possible use in light emitting diodes and infrared detectors. Only $CdSnP_2$, $CdSiAs_2$, $ZnSiP_2$ (14) and $CdGeAs_2$ (52) have been reported to give band to band recombination by either laser or electron beam excitation. Stimulated emission has been observed in $CdSnP_2$(53), $CdSiAs_2$(14) and $CdGeAs_2$(52). A $CdSnP_2$ - InP heterodiode has been constructed by Shay et al. (54), with an emission spectrum peak at 1.4μm.

Ternary chalcopyrite compounds may be most useful in nonlinear optical devices. Noncentrosymmetric crystals such as zinc blende ($\bar{4}3m$) and chalcopyrite ($\bar{4}2m$) compounds can have non zero components in the second order polarisability tensor, d_{ijk}. For instance, two applied electric fields $E_j(\omega_2)$ and $E_k(\omega_1)$ with frequencies ω_2 and ω_1 may produce a polarisation varying with frequency ω_3, such that,

$$P_i(\omega_3) = d_{ijk}(\omega_3,\omega_2,\omega_1)\, E_j(\omega_2)\, E_k(\omega_1)$$

If the applied fields are plane waves, with wavevectors $\underline{k}_2$ and $\underline{k}_1$, then the induced polarisation will have frequency ω_3 and wavevector, $\underline{k}_3$ given by,

$$\omega_3 = \omega_1 \pm \omega_2 \qquad 1.4$$

and

$$\underline{k}_3 = \underline{k}_1 \pm \underline{k}_2 \qquad 1.5$$

Radiation with frequency ω_3 can be emitted by virtue of this oscillating polarisation, but efficiency is restricted by the conditions 1.4 and 1.5, since radiation from different parts of the crystal will in general cancel due to the phase difference. Since $|\underline{k}_i| = n_i.\omega_i/c$, where n_i is the refractive index at frequency, ω_i,

these conditions cannot be met for isotropic media due to dispersion of the refractive index. The conditions can be met however in certain directions for materials which have a large enough birefringence. Boyd measured refractive indices in ternaries and concludes that $ZnGeP_2$(55), $CdGeAs_2$, $ZnSiAs_2$(56), $AgGaS_2$ and $AgGaSe_2$ (57) have birefringences large enough to allow three frequency phase matching.

There are two second order components for the chalcopyrite structure which are equal by symmetry. The magnitude of the component, d_{14}, is compared with the equivalent component in GaAs for several II-IV-V_2 compounds in table 1.1. $ZnGeP_2$ compares well with GaAs. Its use is restricted in the near infrared to the transmission range between 0.64μm at the energy band gap, and 12μm when the absorption increases due to multiphonon processes. Boyd et. al. (55) have produced second harmonic generation of a CO_2 laser line ($\omega_1 = \omega_2$), phase matched upconversion of 10.6 and 1.06μm radiation (58) ($\omega_3 = \omega_1 + \omega_2$), and difference frequency mixing of two CO_2 laser lines into the far infrared region between 70 and 110cm^{-1}(59), ($\omega_3 = \omega_1 - \omega_2$).

Stimulated polariton scattering may also be possible as pointed out by Holah (60). Tunable far infrared radiation using stimulated Raman scattering from polaritons in $LiNbO_3$ has already been accomplished (61). The far infrared wavelength regions free from lattice absorption in $ZnGeP_2$ and $CdGeP_2$ will be considered in Chapter 4, and the polariton dispersion curves given in section 4.4.4.

CHAPTER 2 Crystal Growth and Assessment

2.1 Introduction

A great deal of effort has been expended on the growth of single crystals of II-IV-V_2 materials since 1958. The aim has been to produce crystals of quality and purity required for semiconductor applications. Nonlinear optical applications have added incentive for large, optically perfect crystals. High melting points, which may be incongruent, the large vapour pressure of the group V element at the temperature of the melting point and a high temperature zinc blende phase in many of the materials make production of large crackfree stoichiometric crystals difficult.

A growth method found to overcome some of these problems has been by slow cooling of the constituent elements in a low melting point metal. This chapter describes the growth of $ZnGeP_2$ and $CdGeP_2$ from solution in lead. An assessment of the crystals was made by X-ray analysis and electrical measurements.

2.2 Review of previous work on the growth of $ZnGeP_2$ and $CdGeP_2$

$ZnGeP_2$ has a congruent melting point at about 1025°C (32,34,62), while $CdGeP_2$ has been reported by various groups to melt congruently at, 776°C(63), 779°C(62), 790°C(33) and 800°C(34, 64). Buehler has measured the vapour pressure of $ZnGeP_2$ as a function of temperature and finds that the pressure is 3.5 atmospheres just below the melting point, but this jumps to 7.1 atmospheres by 1060°C in the liquid phase (65). The vapour pressure of $CdGeP_2$ is just above 2 atmospheres at 800°C and shows no abrupt change at the melting point (66). In both cases, the vapour was found to be essentially phosphorus with detectable amounts of zinc or cadmium, found by analysis of the

condensate on cooling. Thus, although slow heating is necessary to avoid explosions due to build up of the vapour pressure of unreacted red phosphorus, the pressure can be maintained by a silica ampoule for growth from the melt, in contrast to the silicon phosphides, $ZnSiP_2$ (m.p. 1370°C; > 18 atm.) and $CdSiP_2$(m.p. 1120°C ; 19.4 atm).

Buehler et. al. have also investigated the phase diagram of both the ZnP_2 - Ge system (32) and the CdP_2 - Ge system (33) by differential thermal analysis, X-ray analysis and metallographic observations. The results are shown in figures 2.1 (a) and (b) respectively. Figure 2.1 (b) agrees well with recent Russian work on $CdGeP_2$ by Borshchevskii et al (64).

In the $ZnGeP_2$ case, in addition to the peaks showing liquidus and eutectic temperatures, D.T.A measurements showed a broad peak at 950°C, which has been interpreted as a solid state phase transition. Quenching to room temperature did not retain the high temperature modification however. This is consistent with other work (41, 34), and will be considered further in section 2.4.2. The $CdGeP_2$ phase diagram is similar to $ZnGeP_2$, but the βCdP_2 melting point is below that of germanium. From this work, Buehler gives the melting point of $CdGeP_2$ as 790 ± 5°C, while Borshchevskii quotes 800 ± 3°C. No peaks associated with a high temperature phase transition could be observed, but in this case, a zinc blende phase could be prepared by quenching from the melt at rates above 15°C/sec and an amorphous phase at rates greater than 25°C/sec (67). Thermochemical investigations of $ZnSiP_2$ and $CdSiP_2$ (65) have not been extended to the germanium compounds.

$ZnGeP_2$ has been grown mostly by direct synthesis. Early attempts by Masumoto et al (34) and Mughal et al (62) produced polycrystalline ingots which were used for electrical analysis. Masumoto used the Bridgman technique in a high pressure furnace, while Mughal

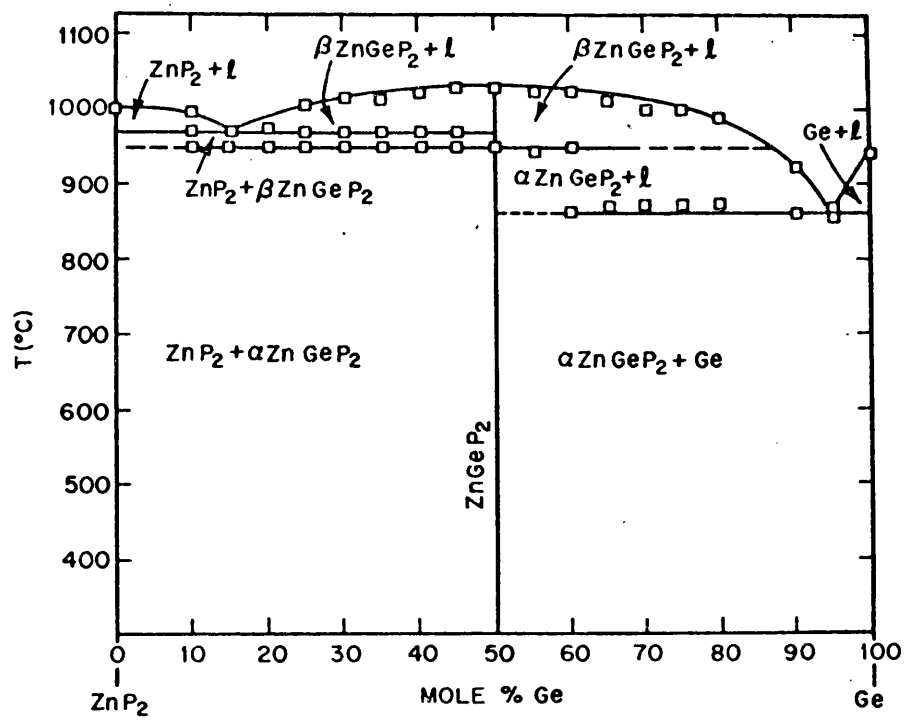

(a)

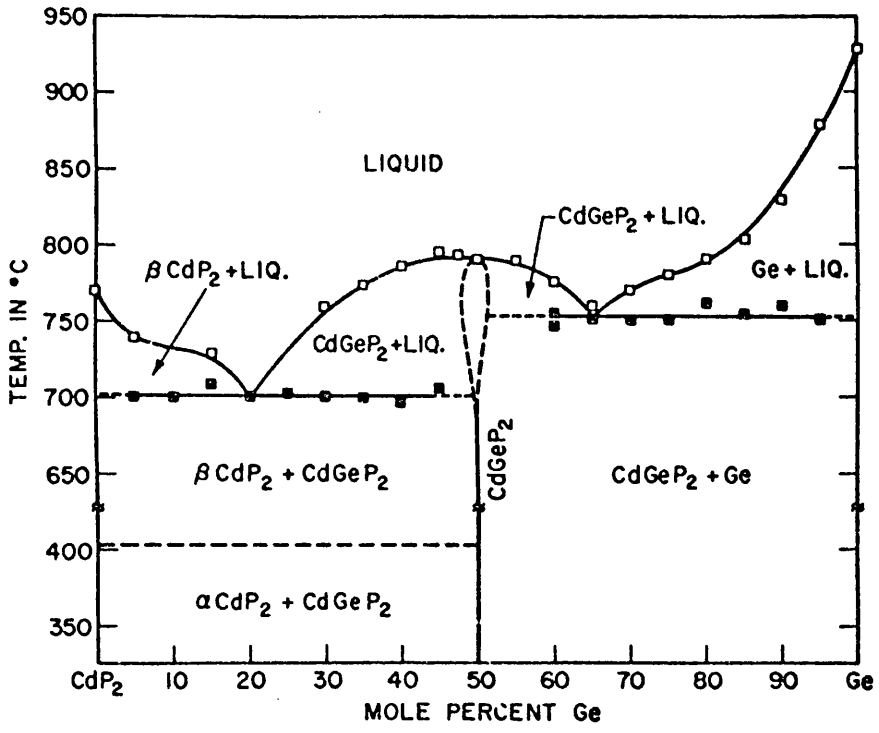

(b)

Figure 2.1 Pseudo-binary phase diagrams.

favoured directional solidification and obtained polycrystalline ingots at cooling rates above 20°C/hr, while at 4°C/hr., the ingots contained single crystals of size 10mm^3 in volume. Ivanova (68) has reported single crystal ingots 20-27mm long and 3-5mm in diameter by the vertical Bridgman method, and Buehler gives details of the successful growth of single crystals of similar dimensions by horizontal directional solidification with a very small temperature gradient, 0.4°C/cm, and a cooling rate of 25°C/day (32). Gentile et al (69) have recently reported growth of large single crystals by the vertical Bridgman technique with a lowering rate of 0.06 in/hr.

Attempts have also been made to grow $ZnGeP_2$ by vapour transport. Mughal et al (62) produced platelets of several cubic millimetres surface area, by 10 to 20μm thickness using a horizontal ampoule with a temperature profile, 1050°C - 1150°C - 450°C, and included a phosphorus reservoir at the cold end. This gave crystals of both $ZnGeP_2$ and ZnP_2. Buehler (65) used a 12°C/cm. gradient to produce crystals of size 1 x 1 x 0.5mm^3. Nucleation on germanium gave no better results. Vapour transport may be inhibited by the formation of a liquid Zn-Ge alloy, as pointed out by Valov (40). In contrast to silicon, the germanium can completely dissolve in the zinc or cadmium charge.

Solution growth has also been tried for $ZnGeP_2$. Tin solution growth has been successful in producing crystals of $ZnSiP_2$, $ZnSnP_2$, and $CdSiP_2$ (39), but extension of this technique to $ZnGeP_2$ (39) has given polyhedral crystals of the alloy $ZnSn_x Ge_{1-x}P_2$, where x is in the range 0 to 0.25 (70). Bertoti et al (71) have grown $ZnGeP_2$ crystals from Bi-Pb eutectics with more success. Cooling rates of 12-17°C/hr. gave platelets of size 6 x 5 x 1 mm^3 as well as large agglomerations

of triangular cross section with maximum dimensions of 10x10x20 mm^3. Oriented single crystals of size up to 10x8x1 mm^3 could be separated.

Very few details of the crystal growth of $CdGeP_2$ have been published. Masumoto et al (34) and Mughal et al (62) grew polycrystalline ingots with a few fine cracks by the vertical Bridgman and directional cooling methods, while Borshchevskii et al (72) reported single crystals of average dimensions 0.5 x 1 x 7 mm. by Stockbarger and zone recrystallisation methods. Crystal growth by Buehler has successfully grown large single crystal ingots with 3 to 10 large cracks by directional cooling of 10 to 20°C/day in a 4°C/cm temperature gradient with excess phosphorus (33). Buehler et al also grew $CdGeP_2$ by vapour transport with crystals of size $8mm^3$ forming after 10 to 30 days (33). In this case 15% excess germanium was added over the stoichiometric amount. Growth from 8 mol % cadmium and tin solutions by the same group gave crystals of size 2-4 mm^3(33).

This survey does not exhaust the reports of the growth of $ZnGeP_2$ in the literature, but includes those papers in which some details of the method have been given.

2.3.1 Solution growth technique

Melt growth has been the most popular technique used for $ZnGeP_2$, while $CdGeP_2$ seems to have been grown almost exclusively by this method. Solution growth by slow cooling does have certain advantages over melt techniques when there is difficulty in producing large crystals (73).

Crystals grown from solution usually have well formed faces of low index, which is beneficial for optical measurements, especially when polishing or etching can be eliminated. Solution growth lowers the temperature at which solidification takes place, so that cracks which have often been reported in melt grown crystals may be avoided

by growth from below the high temperature structure modification.

The main disadvantages of the solution growth method are that it is slow; growth stability is difficult to attain; the solvent may have a significant solubility in the crystal either as an impurity or in large enough quantities to form an alloy. As growth by slow cooling may be over a region of several hundred degrees, an impurity gradient is likely to result along the growth direction of the crystal due to the variation of the growth conditions with temperature.

A suitable cooling rate must be chosen which is slow enough to give a stable growth rate. The rate of growth at any temperature depends on the solubility of the compound in the solvent at that temperature and the surface area of the crystal. The limit to the rate is set by the time for diffusion of the solute to the growing crystal face. As the crystal forms, a layer will exist around the growing face, which is deficient in solute. Thus, if any protrusions appear on the surface, these may enter a more concentrated, or super-saturated region, and grow preferentially. This is called constitutional supercooling. II-IV-V_2 crystals grown from solution are normally reported to contain solvent inclusions caused by this effect. There will also be a temperature gradient in this region of the growing interface, giving a variation of the solubility with position. As the solution cools, the solvent and grown crystals must give up heat, while latent heat is expended at the interface as the crystal solidifies. The temperature gradient may reduce the constitutional supercooling depending on the relative specific heats and thermal conductivities of the crystal and solvent. Convection or stirring are possible ways of reducing supercooling. If these difficulties can be overcome, seeding or local cooling may be used to reduce random nucleation.

The process of growth is thus very complex and a full investigation of it in a particular case is not normally made until growth from a given solvent is found to be successful. For adamantine compounds, choice of solvent is limited by the high growth temperatures required. A metal with as low a melting point as possible is normally chosen to give a low eutectic temperature and to lower the growth temperature. Tin has been a popular choice, and crystals of $ZnSiP_2$, $CdSiP_2$, $ZnSnP_2$ and $CdSnP_2$ have been grown successfully from 10 to 20 mol % solutions. The only experimentally determined solubility curves seem to be for $ZnSiP_2$ and $ZnGeP_2$ in tin (31, 39) and $ZnSiP_2$ in zinc (74). Tin has also been used for the growth of $ZnGeP_2$ and $CdGeP_2$, but in both cases, the material obtained has been an alloy with the corresponding tin compounds, shown by the larger lattice parameters compared to melt grown compounds. Other solvents which have been used for growth of II-IV-V_2 compounds are Zn, Cd, Pb, Bi, Sb and In. There is reduced risk of incorporation of the solvent as an impurity if one of the constituents such as zinc or cadmium is used, but Bertoti (71) favoured a Pb-Bi eutectic for growth of $ZnGeP_2$, since no chemical binary compounds have been found for these materials with Zn, Ge or P, neither have they been involved in the formation of II-IV-V_2 compounds.

The present work is similar to that of Bertoti, but uses only Pb as the solvent. $CdGeP_2$ was also grown successfully from lead solution, but attempts to grow $CdSiP_2$ failed due to broken ampoules. The growth method described here also differs from the previous work using Bi-Pb eutectics in that it employed the accelerated crucible rotation technique (75). This has been successfully used to improve crystal quality for many materials, and has been employed recently to the growth of $ZnSiP_2$ from Sn and Zn (76).

2.3.2 Experimental method

A silica ampoule, 15cm long and 2 cm in diameter, having an open 1 cm silica tube on one end was cleaned in detergent followed by a soak in 1 HNO_3: 1 HCℓ for several hours. The ampoule was rinsed out with distilled water many times and then flame polished by heating to just below the softening point of the silica, while a vacuum was maintained inside. The constituent elements were weighed accurately in stoichiometric quantities and transferred to the ampoule, together with enough lead to make up a 20 mol % solution. The total charge was about 100 gms. Materials were high purity to at least 99.999%, obtained from Koch-Light Laboratories Ltd. or Mining and Chemical Products Ltd. The lead, zinc and cadmium were in shot form while germanium was added as powder and phosphorus in small lumps. The zinc and cadmium were etched in concentrated nitric acid for a few seconds to remove surface oxides and then rinsed well in distilled water. The 1cm tube was necked down to leave only a small hole just above the ampoule, and the open end coupled to a vacuum system with a liquid nitrogen trap. The ampoule was left to de-gas for several hours, this being aided in the initial stages by gentle heating of the ampoule. The final pressure was about 10^{-4} torr, and the ampoule was sealed by heating the neck causing it to collapse. The ampoule was then placed in a kanthal wire basket and thermocouples attached as near as possible to the contents.

The basket was placed in the central uniform temperature region of a furnace. The furnace was initially placed horizontally on a rocking device to improve mixing during heating. Power was supplied by a Eurotherm temperature controller governed by a platinum thermocouple placed inside the furnace. Linear heating and cooling rates were obtained by driving a potentiometer which backed off the thermo-

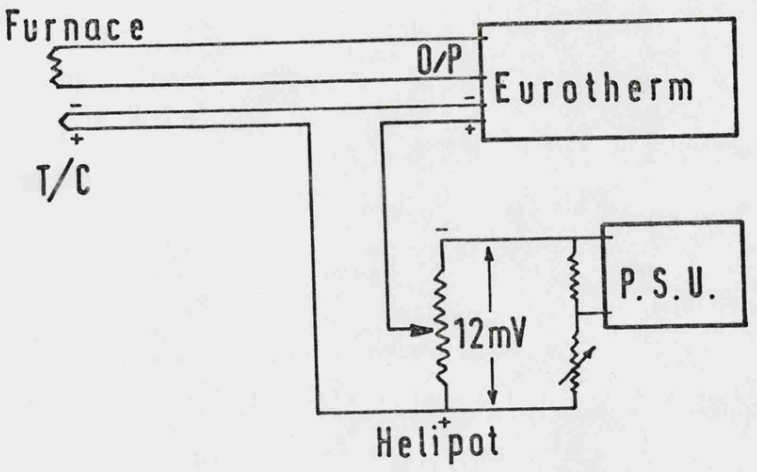

Figure 2.2 Thermocouple back-off circuit used to control the cooling rate of the furnace

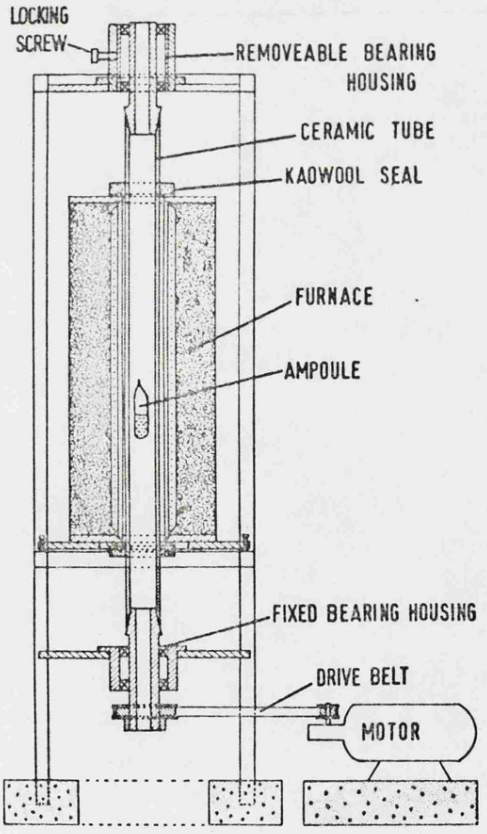

Figure 2.3 Accelerated crucible rotation furnace

couple voltage using the circuit shown in figure 2.2. The heating rate was 60°C/hr. to just below the melting point of the compound ($ZnGeP_2$ m.p 1025°C, $CdGeP_2$ m.p. 800°C). The furnace was left rocking for two hours after this temperature had been reached, and then it was returned to its vertical position and left to come to equilibrium. A 1.5°C/hr. cooling rate was used in all growth runs and the ampoule rotated by means of the apparatus shown in figure 2.3. As no details of the solubility curve of either $ZnGeP_2$ or $CdGeP_2$ in lead are known, this rate of cooling was maintained until 50°C above the melting point of lead, 327°C. At this point. the cooling and stirring were stopped, and the central tube of the furnace removed with the ampoule inside. This was inverted in order to decant the lead to avoid cracking the crystals as the lead solidified. The ampoule was returned to the furnace with the power switched off and allowed to cool to room temperature.

The ampoule was broken open to extract the crystals, and the remaining lead holding the crystals together dissolved by treatment in CH_3COOH: H_2O_2 = 1:5. This had no observable effect on the crystal surfaces.

2.3.3 Growth assessment

Both $ZnGeP_2$ and $CdGeP_2$ nucleated randomly from the lead solution on the walls of the ampoule. Growth produced a large mass of crystals from which single crystals, generally in the form of platelets of size up to 8 x 6 mm^2, could be separated. Figures 2.4 and 2.5 show typical single crystals of $ZnGeP_2$ and $CdGeP_2$. $ZnGeP_2$ is a deep red colour while $CdGeP_2$ is a metallic grey although it shows a very deep red when a thin platelet is viewed in transmission of intense white light. The choice of solvent can alter the crystal habit because of the different surface energy between the crystal and

Figure 2.4 Crystals of $ZnGeP_2$

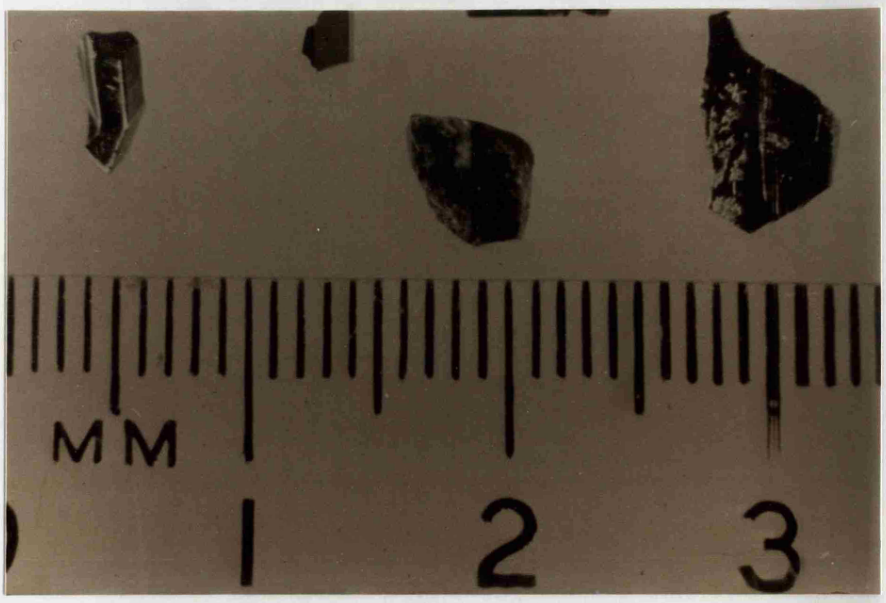

Figure 2.5 Crystals of $CdGeP_2$

the solvent, but in both cases the usual {112} and {101} faces were the most developed with the growth direction along [111] . Laué back reflection determined the largest faces to be (112) with smaller (101) and (011) faces on the edges. The $(\bar{1}\bar{1}\bar{2})$ faces were not developed and often gave rise to nucleation for other crystals.

A complete study of the effect of crucible rotation on the crystal growth was not undertaken, but from the growth runs made, rotation seemed to broaden the crystal faces from a more needle shaped habit to platelets and the quality of the faces was improved. In particular, $CdGeP_2$ grown without stirring cracked very easily and the faces were not very well developed. With a slow stirring rate of 4 osc./min. and 270° rotation on each cycle, crystals with faces suitable for optical measurements were obtained. Very few solvent inclusions were found in $ZnGeP_2$ crystals, although they were quite common in $CdGeP_2$. No overall increase in the size of the crystals was apparent due to stirring.

2.4.1 Lattice parameter determination

To check the structure and lattice parameter size of the grown crystals against previously reported material, X-ray powder diffraction analysis was employed. A Phillips X-ray diffraction camera was used with Straumanis film configuration. Copper K_α radiation was used to irradiate the finely powdered sample.

The distance, d, between planes with Miller indices (h, k, ℓ) for the tetragonal space group, $I\bar{4}2d$, is, given by,

$$\frac{1}{d^2} = \frac{h^2 + k^2}{a^2} + \frac{\ell^2}{c^2} = \frac{4.\sin^2\theta}{\lambda^2}$$

The lattice is non-primitive so there will be systematic absences. Conditions limiting possible reflections are (77),

hkℓ: $h + k + \ell = 2n$

0kℓ: $k + \ell = 2n$

hhℓ: $(\ell + 2n)\ \ 2h + \ell = 4n$

h00: $(h = 2n)$

hh0: $(h = 2n)$

A computer programme was written to calculate d and θ for copper K_{α_1}, K_{α_2} radiation and the weighted mean, from previously published lattice parameters for $ZnGeP_2$ and $CdGeP_2$ in order to index the powder photographs. The indexed films are shown in figure 2.6 and 2.7. Resolution of the K_{α_1} and K_{α_2} doublets are clearly observed at high θ values. The films were measured accurately using a vernier ruler and film shrinkage errors corrected for.

If the camera constants are known accurately, there are two main sources of systematic error. Absorption of the X-rays tends to shift the lines to higher θ values. Eccentricity of the sample in the direction of the X-ray beam will increase or decrease θ depending on the sense of the displacement. Both of these effects become zero for backscattering ($\theta = 90^\circ$), so that a least squares fit to a correction function in θ which extrapolates the calculated values of the lattice parameters from the various lines to $\theta = 90^\circ$ gives an accurate determination of the lattice constants. Various correction functions including the Nelson-Riley formula for absorption (78) were tried in a computer programme written by Y.L. Lee (79). The resulting lattice parameters are shown in Table 2.1, and are compared with those published.

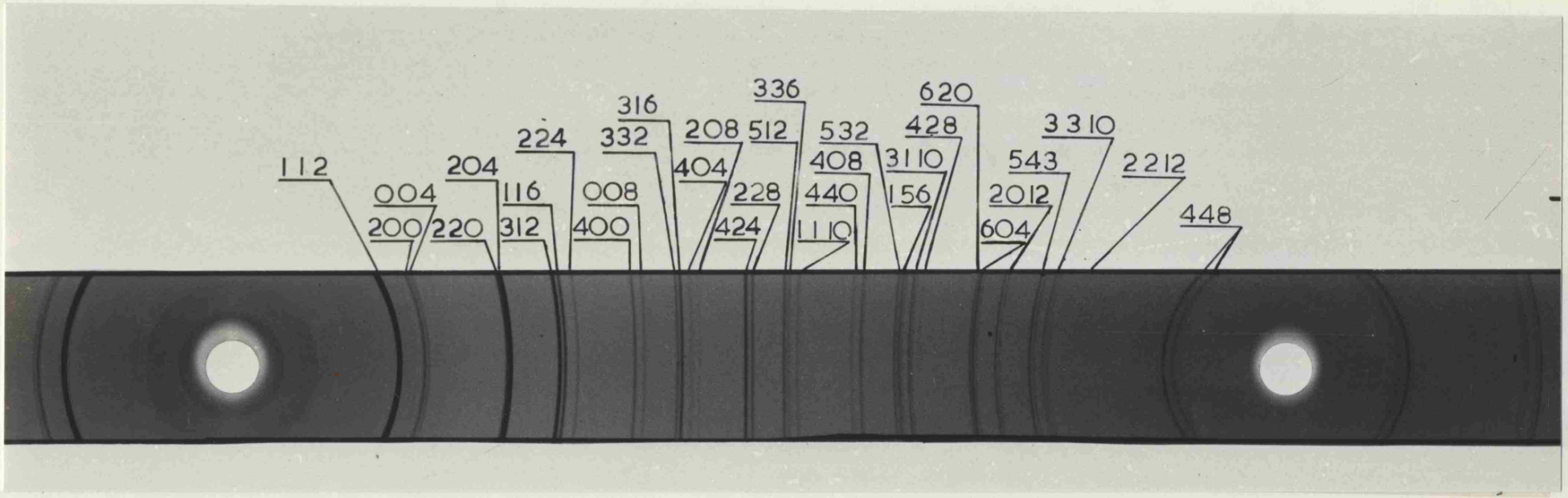

Figure 2.6 Indexed X-ray powder photograph of $ZnGeP_2$

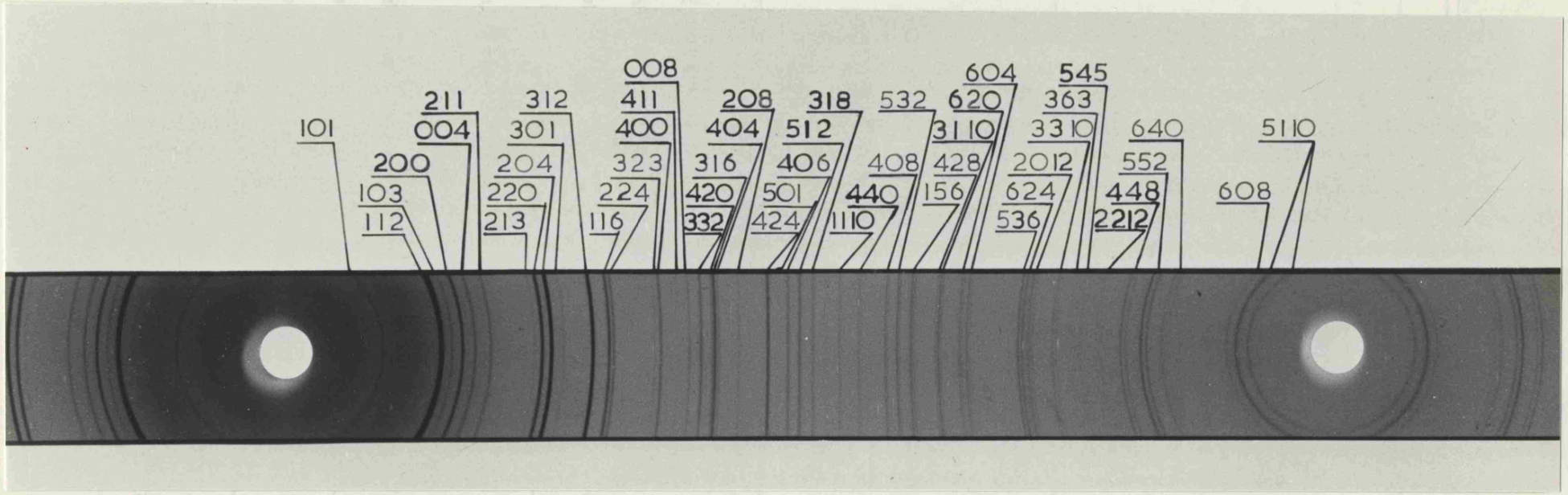

Figure 2.7 Indexed X-ray powder photograph of $CdGeP_2$

Table 2.1 Lattice parameters

	a (Å)	c (Å)	c/a	Growth	Ref.
$ZnGeP_2$					
	5.464	10.708	1.960	This work	
	5.465	10.771	1.971	?	(9)
	5.466	10.719	1.961	M	(34)
	5.465	10.707	1.959	M	(32)
	5.465	10.710	1.959	S (Pb-Bi)	(71)
	5.466	10.722	1.961	M	(41)
	5.491	10.800	1.970	S (Sn)	(39)
$CdGeP_2$					
	5.741	10.770	1.876	This work	
	5.741	10.775	1.877	?	(9)
	5.738	10.776	1.878	M	(30)
	5.740	10.775	1.877	M	(33)
	5.740	10.777	1.878	M	(80)
	5.741	10.770	1.876	M (A)	(81)

M = melt ; s = solution ; A = annealed.

In this work a is ± 0.001Å, c = ± 0.002 Å.

There is some scatter in these results particularly in the measured c values which may be due to stoichiometry differences. The measured values of this work compared to melt grown crystals show that no appreciable quantity of the solvent has entered in solid solution with the compounds. It is interesting to note that the lattice parameters for $CdGeP_2$ agree exactly with these quoted by Vaipolin (81) for melt grown crystals which had been annealed, and yet all other reported parameters for melt grown crystals have had significantly larger values of c. Vaipolin studied the effect of annealing of melt grown crystals and found that the lattice parameters changed from the range a = 5.739 - 5.740 Å, c = 10.774 - 10.777 Å before

annealing, to a = 5.741 - 5.742 Å, c = 10.770 - 10.772 Å after annealing.

2.4.2. High Temperature Lattice Parameters of $ZnGeP_2$

As mentioned in section 2.2, D.T.A. measurements have shown a peak which has been associated with a high temperature phase transition in $ZnGeP_2$ (32, 34, 41), but the phase has not been retained on quenching. A high temperature X-ray camera was employed to determine this structure.

The camera was a 19cm. Unicam S150 high temperature powder camera with films mounted in the Van Arkel configuration. Since two separate films are used on either side of the X-ray beam, the θ values of the images of pins located in front of the films were calibrated first of all by four measurements of Al_2O_3 at room temperature. Powdered $ZnGeP_2$ was then sealed in a silica tube of 0.3 mm. diameter and placed in the cavity at the centre of the camera. Heating was by radiation from elements surrounding the cavity, and a thermocouple placed near the sample recorded the temperature. Exposures were made at 200°C intervals up to 1020°C, that is 5° below the melting point, but the chalcopyrite structure was retained. Just above 1025°C, the silica tube disintegrated.

The lattice parameters were calculated as described in section 2.4.1 and the results are shown as a function of temperature in figure 2.8. Agreement with room temperature results of section 2.4.1, were within ± 0.001Å. A positive coefficient of thermal expansion is obtained with the value of a increasing more quickly than c. Thus, the tetragonal compression increases with temperature. This is opposite to the results reported by Mughal et al (62).

To understand the nature of this effect, the x parameters

were calculated from a and c values, assuming a perfect Ge-P_4 tetrahedron, section 1.2, with bonding angle 109.47° as suggested by Abrahams and Bernstein (16). From geometry,

$$x = 0.5 - \left[\frac{c^2}{32a^2} - \frac{1}{16} \right]^{\frac{1}{2}} \qquad 2.1$$

The variation of the calculated x parameter with temperature is shown in figure 2.9. Lind and Grant (18) measured the room temperature x parameter as 0.25816, which is to be compared to the calculated room temperature value of 0.26019. Thus, although the assumption of a perfect Ge-P_4 tetrahedron gives good correspondence of calculated and measured values when different II-IV-V_2 compounds are compared, the error is larger than the change due to temperature over 1000°C. Nevertheless, the change in the length of the Zn-P and Ge-P bonds were calculated from the geometrical expressions,

$$A - C = \left[a^2 x^2 + \frac{4a^2 + c^2}{64} \right]^{\frac{1}{2}} \qquad 2.2$$

$$B - C = \left[a^2 (\tfrac{1}{2} - x)^2 + \frac{4a^2 + c^2}{64} \right]^{\frac{1}{2}} \qquad 2.3$$

to show the trends in the changes of the bond lengths, figure 2.9. It is assumed that the near perfect Ge-P_4 tetrahedral structure will be maintained to high temperature. The thermal expansions in figure 2.9 are, Zn-P = 2.15×10^{-5} Å/K and Ge-P = 1.16×10^{-5} Å/K. This can be compared to similar work done in this laboratory by Humphreys on $ZnSiP_2$(82). He finds that the thermal expansion of the Zn-P bond calculated in the same way is 2.25×10^{-5} Å/K. The very good agreement between the thermal expansions of the Zn-P bonds in both materials is taken to justify this approach. The thermal expansions of the bonds of similar materials can also be compared. The value for GaP in this temperature range is 1.25×10^{-5} Å/K (83) and is comparable with the covalent - like Ge-P bond. Data for ZnS,

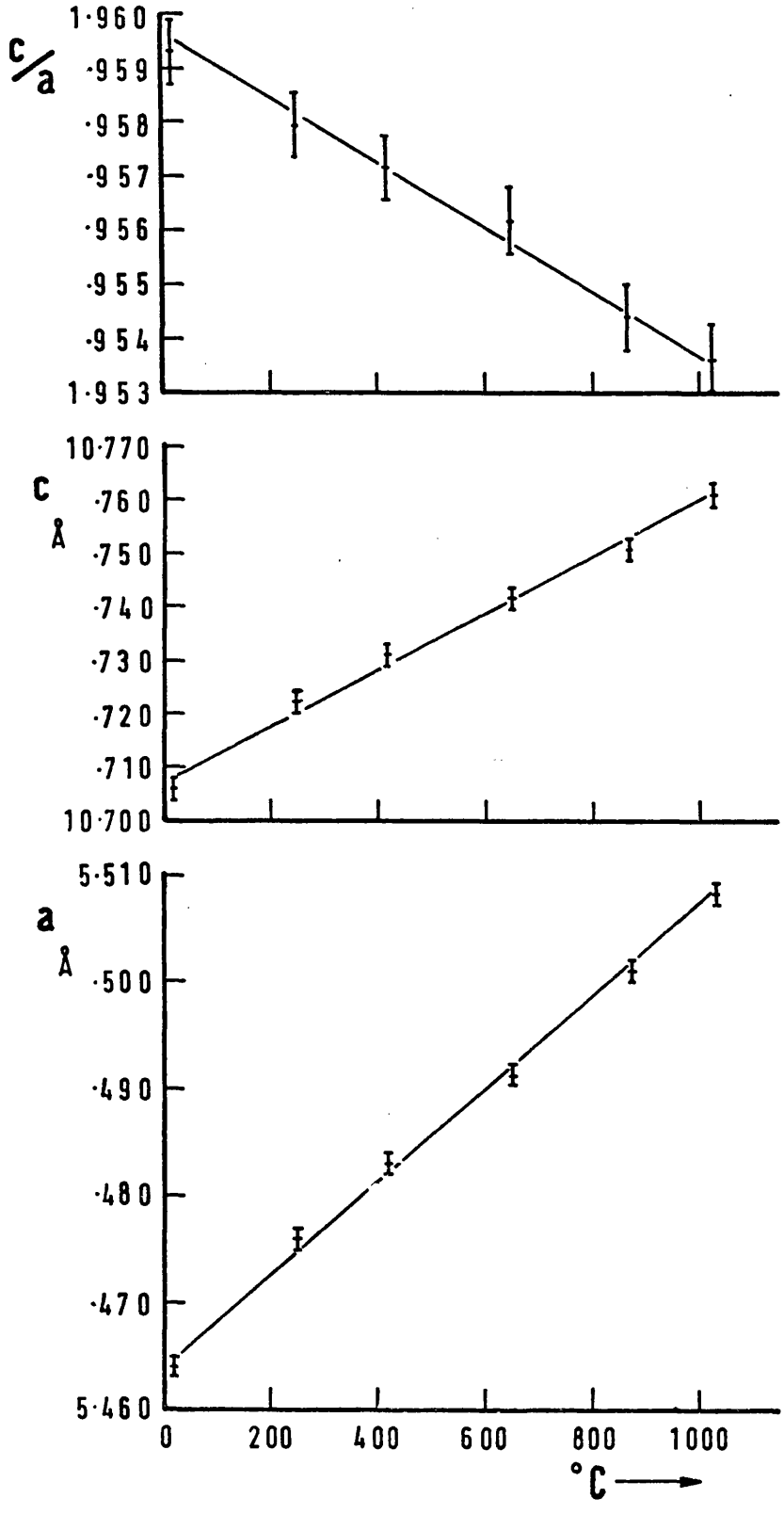

Figure 2.8 Temperature dependence of the lattice parameters of $ZnGeP_2$

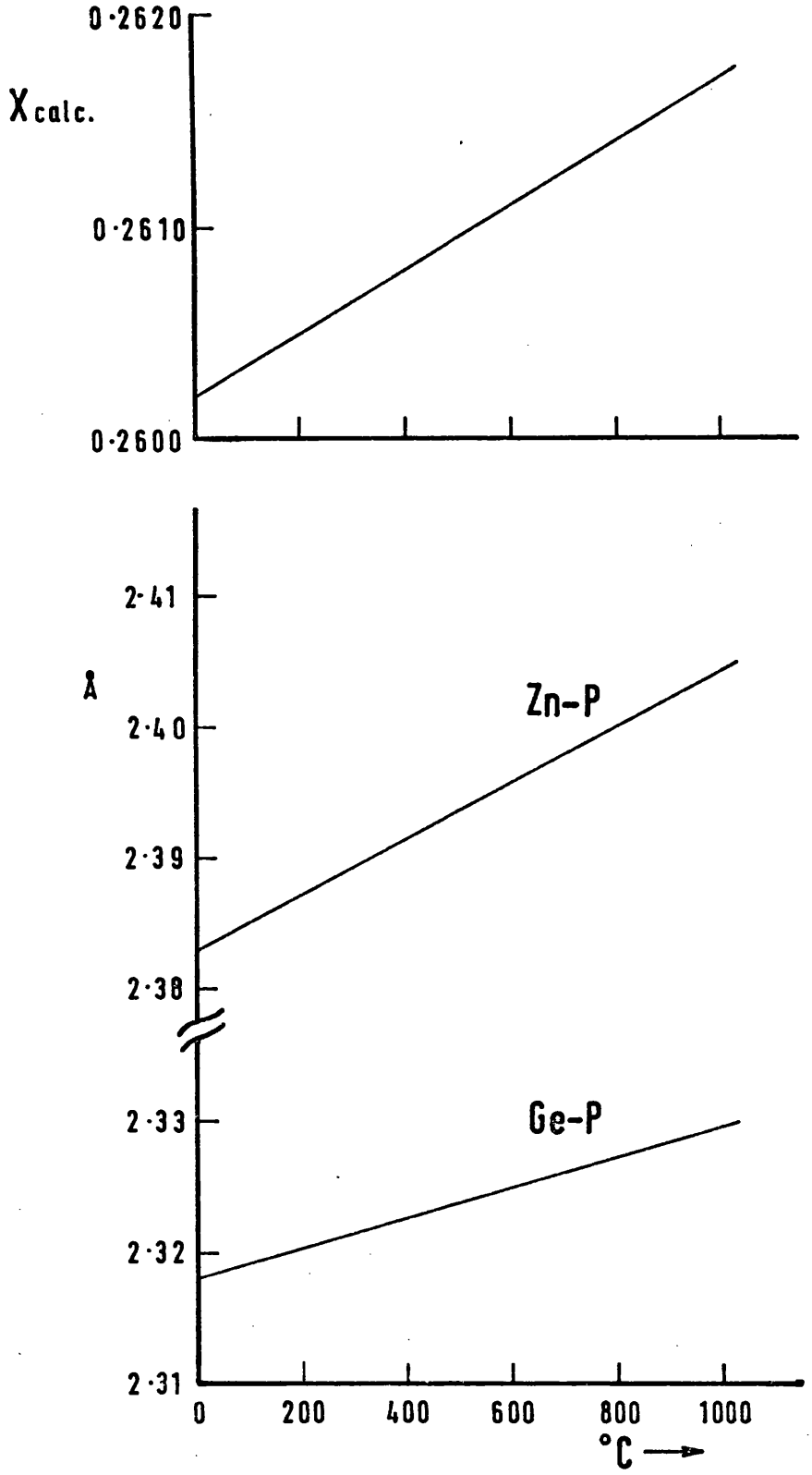

Figure 2.9 Calculated bond lengths in $ZnGeP_2$

the II-VI isoelectronic analogue was not found in the literature, but ZnSe has a thermal expansion of 1.96×10^{-5} Å/K(84).

We can thus conclude that as the temperature increases, the more ionic II-V bond increases more quickly than the stronger IV-V bond, causing a relative shift of the phosphorus towards the group IV atom. The x-parameter thus increases and hence the tetragonal compression also.

2.5.1 Hall effect and resistivity measurements

Variations of the Hall effect and conductivity of $ZnGeP_2$ and $CdGeP_2$ with temperature were measured by the Van der Pauw technique (85). Crystals were selected and ground on a polishing jig with 6 and 1 micron diamond pastes, to produce plane parallel platelets of area 5 x 5 mm^2 and approximately 200μm thick. The platelets were checked for solvent inclusions and twins with a polarising transmission microscope. The surfaces were cleaned by a 30 second etch in 5 conc HNO_3 : 5 conc HCℓ : 1 HF. Four tin dots were spaced around the edge of each crystal using a small soldering iron, the tin being previously cleaned with hydrazinium chloride flux. The crystal was placed on a brass plate with a probe touching one of the tin contacts. A 200 volt pulse between probe and plate normally gave an ohmic contact suitable for electrical measurements. In the case of $CdGeP_2$, the crystal had to be heated to 150°C to lower the resistance. The contacts were checked for any rectifying nature by observing the I-V characteristic across two contacts on an x-y oscilliscope when a small a.c. voltage was applied.

The crystal was placed on an alumina plate on a copper block and copper wires attached to the contacts with silver paste. Two wires doubled as thermocouples by having constantin wires soldered to them. A resistive heating element around the copper block gave

temperatures above room temperature. An evacuated non-magnetic stainless steel tube surrounded the crystal and block giving temperatures down to 78K by insertion in liquid nitrogen. Temperature control was provided by the heating element connected to a thermocouple feedback circuit. Current was supplied to the crystal by a 30V battery and the current and voltages measured on a Keithley 610C electrometer.

The Van der Pauw technique combines the measurement of mobility and conductivity in one sample using four contacts. If the contacts are labelled A, B, C and D in order round the sample, then $R_{AB,CD}$ is defined as the voltage between C and D when unit current flows between A and B. Complex variable theory shows that the resistivity, ρ, is given by,

$$\rho = \frac{\pi . d}{\ell n\ 2} \cdot \frac{R_{ABCD} + R_{BCDA}}{2} . f\left(\frac{R_{ABCD}}{R_{BCDA}}\right) \qquad 2.4$$

where d is the crystal thickness, and,

$$f\left(\frac{R_{ABCD}}{R_{BCDA}}\right) = 1 - \left[\frac{R_{ABCD} - R_{BCDA}}{R_{ABCD} + R_{BCDA}}\right]^2 \cdot \frac{\ell n\ 2}{2} + \left[\frac{R_{ABCD} - R_{BCDA}}{R_{ABCD} + R_{BCDA}}\right]^4 \cdot \left[\frac{\ell n^2 2}{4} - \frac{\ell n^3 2}{12}\right]$$

With a magnetic field, B, perpendicular to the sample, the Hall mobility is given by,

$$\mu_H = \frac{d . \Delta R_{ABCD}}{B . \rho} \qquad 2.5$$

where ΔR_{ABCD} is the change in the measured value of R_{ABCD} when the magnetic field is applied. For a material with a single carrier type, the Hall constant (86) is given by,

$$R_H = \mu_H . \rho \qquad 2.6$$

and the carrier concentration,

$$n = \frac{1}{R_H . e} \qquad 2.7$$

The activation energy, ε, of an impurity can be found by observing the variation of these quantities with temperature. Two approximations may be made to solve the equations from a Fermi-Dirac distribution of electrons in an extrinsic semiconductor. For a compensated material, the density of donor impurities, N_d, and acceptor impurities, N_a, are comparable, so that if $N_d > N_a >> N_c . \exp(-\varepsilon_d/k.T)$ where N_c is the effective density of conduction band states, then the carrier concentration is given by,

$$n = \frac{N_d - N_a}{2.N_a} . N_c . \exp\left(-\frac{\varepsilon_d}{k.T}\right) \qquad 2.8$$

In the uncompensated case, an n-type material has $N_a << N_c.\exp(-\varepsilon_d/k.T) << N_d$, and

$$n = \tfrac{1}{2} (N_d.N_a)^{\frac{1}{2}} . \exp\left(-\frac{\varepsilon_d}{2.k.T}\right) \qquad 2.9$$

N_c varies as $T^{3/2}$, thus in the compensated case, $\ell n\ n.T^{2/3}$ or $\ell n\ R_H.T^{3/2}$ plotted against $^1/_T$ gives the donor energy.

2.5.2 Results of electrical measurements

The variations of the Hall constant, Hall mobility and conductivity with temperature are shown in figure 2.10 for $ZnGeP_2$. The material was p-type with a room temperature carrier concentration of 2.4×10^{14} cm^{-3}, and a resistivity of 2.3×10^3 Ω.cm. The low carrier concentration and high resistivity indicate that the acceptors are compensated so that $R_H.T^{3/2}$ was plotted logarithmically against $^1/_T$. This gave an acceptor activation energy of 0.208 eV from equations 2.7 and 2.8. The mobility was very low and increased with temperature according to $\mu \sim T^{1.22}$. Ionised flaws normally give a $^3/_2$ power dependence, while neutral scattering centres give a mobility which is independent of temperature. The predominant scattering mechanism here is thus probably due to ionised impurities.

These results can be compared with previous work. Isomura

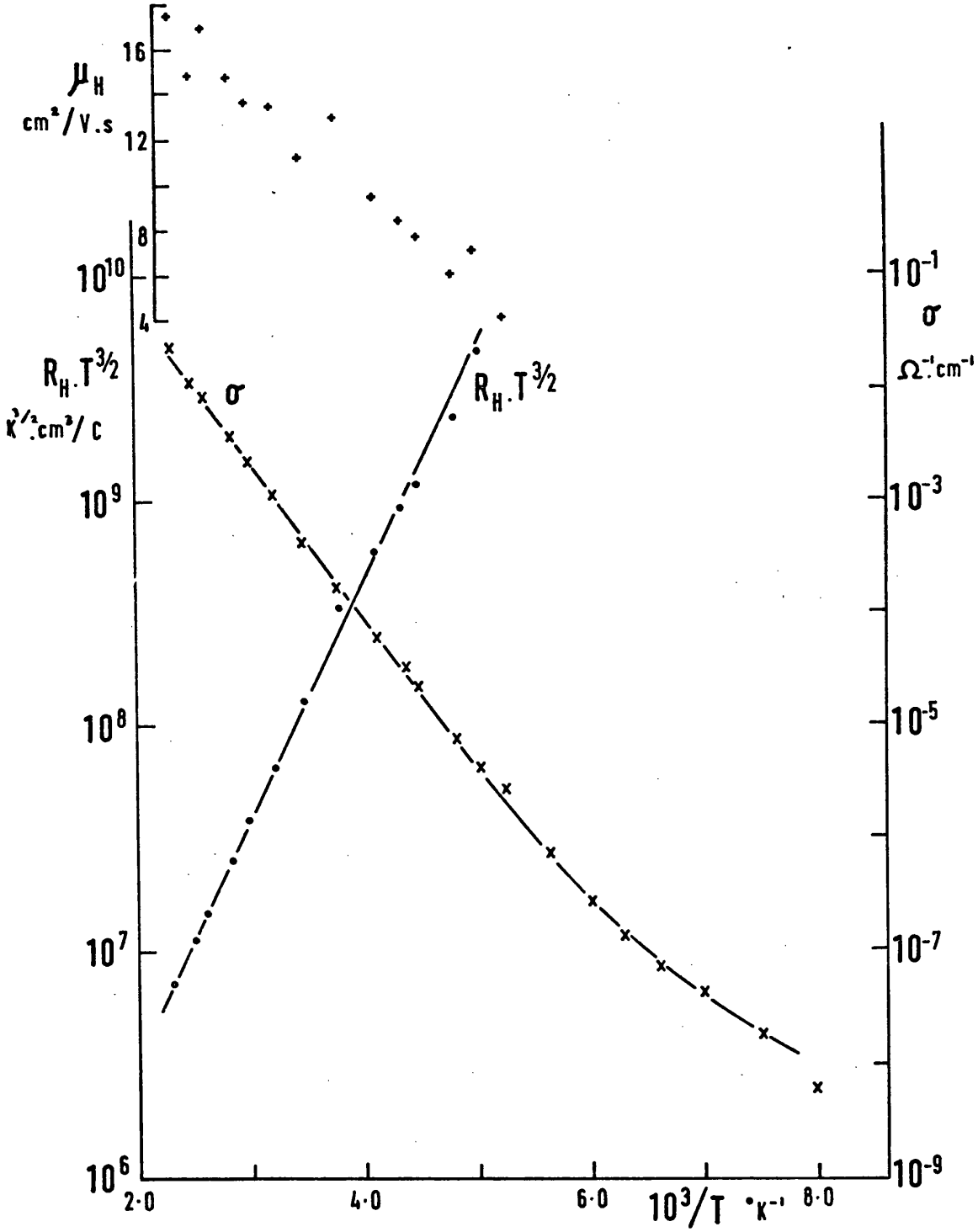

Figure 2.10 Electrical properties of $ZnGeP_2$

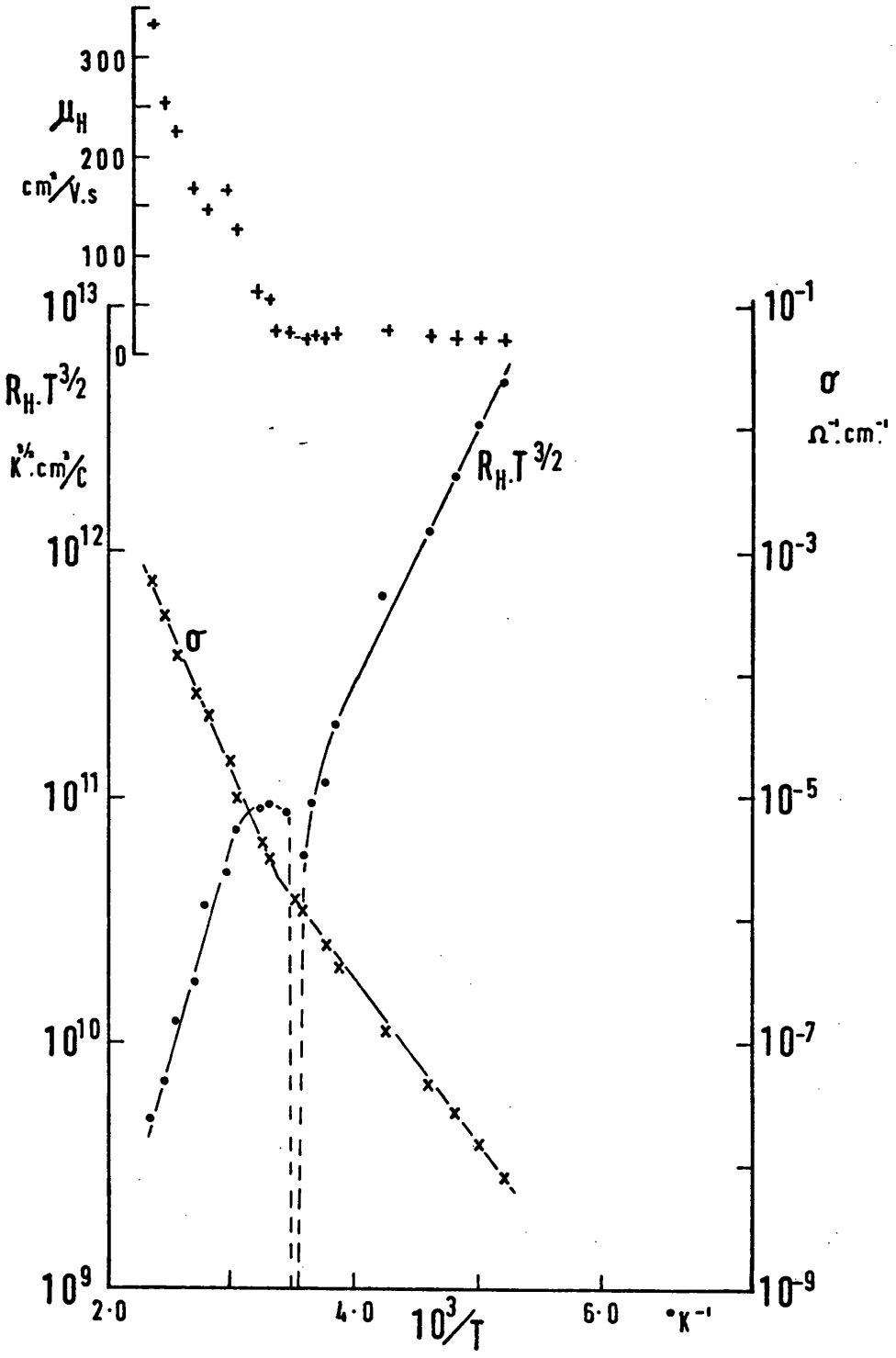

Figure 2.11 Electrical properties of $CdGeP_2$

and Masumoto (87) obtained melt grown crystals with resistivities of 10^6 - 10^7 Ω.cm and an acceptor activation energy of 0.55eV. Crystals grown by Ray et al (41) from the melt were similarly high resistivity, with an acceptor energy of 0.62eV, although this was calculated using the uncompensated approximation. The Pb-Bi solution grown crystals of Somogyi and Bertoti (71, 88, 89) had resistivities of 10^4 Ω.cm and a (compensated) acceptor activation energy of 0.35eV.

The $CdGeP_2$ results are shown in figure 2.11, and are more interesting because of the discontinuity of the Hall constant at about room temperature. At low temperature, the material was p-type, and the compensated approximation gave an activation energy of 0.202eV from the slope of $\ell n\ R_H.T^{3/2}$ vs. $^1/_T$. This is very close to the acceptor activation energy found for $ZnGeP_2$ and may be due to a similar defect or impurity. At around room temperature, where the resistivity was 7×10^5 Ω.cm, the Hall effect showed that the material changed to n-type conduction. This situation has been found previously in $CdGeAs_2$ (90) and $ZnSnAs_2$ (9). The change of sign of the Hall constant has been studied in detail for GaSb by Leifer and Dunlap (91).

For mixed conduction, the Hall constant is given by (92),

$$R_H = \frac{1}{e} \cdot \frac{n.b^2 - p}{(n.b + p)^2} \qquad 2.9$$

where b is the mobility ratio μ_n/μ_p. Thus, at the transition temperature, T´,

$$n.\mu_n^2 = p.\mu_p^2 \qquad 2.10$$

A possible model for the process is as follows. If the number of acceptors, N_a, exceed the number of donors, N_d, the donor electrons will fall to the empty acceptor states at low temperature. The low temperature conduction is thus due to the holes produced when electrons from the valence band begin to fill up the remaining acceptor states. At the cross-over, T´, sufficient electrons have been excited into the conduction band to make equation 2.10 valid. As the hole

mobility appeared to be constant, equation 2.10 gives an estimate of $n.\mu_n^2$ when the concentration of holes calculated from equation 2.7 in the low temperature region is extrapolated to T´. However, the conductivity was also determined at this point, so that $n.\mu_n$ can be obtained from,

$$\sigma = e(n.\mu_n + p.\mu_p) \qquad 2.11$$

This gives the values of n and μ_n,

$$n = 4.78 \times 10^{10} cm^{-3} \qquad \mu_n = 42.2 \ cm^2/V.s$$

$$p = 2.63 \times 10^{11} cm^{-3} \qquad \mu_p = 18 \ cm^2/V.s$$

and so the mobility ratio, b is 2.3 at T´.

Very little work has been done previously on the electrical properties of $CdGeP_2$ to compare with these results. Crystals have normally been reported to have high resistivities when grown from the melt and difficulty has been encountered in making ohmic contacts (66). Borshchevskii et al (72) has measured the variation of the Hall constant and resistivity with temperature in p-type and n-type melt grown crystals. Hole and electron mobilities were found to be constant with temperature at 50 $cm^2/V.s$ and 1000 $cm^2/V.s$ respectively, probably due to neutral scattering centres. The donor and acceptor activation energies were calculated to be 0.40 eV and 0.55eV respectively using the uncompensated approximation.

CHAPTER 3 Lattice Dynamics Theory

3.1 Introduction

Understanding of the motions of the atoms of a crystal and hence the restoring forces which exist when the atoms are displaced from their equilibrium positions is fundamental to the interpretation of many properties of solids such as electrical resistance, specific heat, optical and dielectric properties. These forces are determined by the chemical bonding of the atoms which must be elucidated to solve the equations of motion for the atoms.

The present understanding of the lattice dynamics of the chalcopyrite structure is presented in this chapter, and the basic theory introduced for interpretation of infrared reflectance measurements which will be described in Chapter 4, and for Raman scattering measurements in Chapter 5 for $ZnGeP_2$ and $CdGeP_2$.

3.2 Basic Theory

Several types of bonding mechanism exist between the atoms of solids. The outer shell or valence electrons of the atoms determine the type of bonding, and hence the structure of the solid by choice of the atomic configuration with the lowest energy. The possible modes of vibration of any crystal structure can be found from group theory by analysis of the symmetry properties of the structure. The frequency eigenvalues and displacement eigenvectors however are linked to the detailed interatomic forces and so a model must be constructed to represent these restoring forces in order to solve the equations of motion for the modes (93).

A great deal of theoretical work has centred on the alkali halides such as KBr in which the single electron in the outer shell of the potassium is transferred to the outer shell of the bromine

atom. The f.c.c. rock salt structure results with each atom at a potential minimum between the attractive Coulomb forces, dominated by the six oppositely charged nearest neighbours, and the repulsive overlap forces of the electronic shells, mostly due to the Pauli exclusion principle. The coulomb forces extend beyond nearest neighbours, but the repulsive forces are short range and need only normally be considered for nearest neighbours.

The atoms are in constant motion and although strictly, one should solve the Schroedinger equation for the system, this proves too difficult in all cases, and some simplifying assumptions must be made to predict the eigenvalues. The adiabatic approximation assumes that the response of the outer electrons to an electric field is much faster than the positively chargedcore together with its inner filled shells of electrons so that the two can be treated as separate entities. The harmonic approximation assumes that for small displacements, the restoring force on the ions will be proportional to the displacement.

The rigid ion model was the first simple model to be applied to alkali halides, treating the positive and negative ions as point charges. However, the distortion of the electron distribution with displacement was found to be significant and the shell model was introduced which in its simplest form considers the strong repulsive forces to act between the outer electron shells of nearest neighbours, while the interaction of the outer shell and its ion core can be represented by another, stronger force constant. More elaborate shell models using more force constant parameters have successfully reproduced the complete phonon dispersion curves for the alkali halides determined from neutron scattering measurements.

Covalent bonding, as in the elemental semiconductors silicon

and germanium, is more difficult to treat. The electrons forming the bonds tend to be localised with antiparallel spins in the region between the two atoms giving highly directional tetrahedral bonding. A shell model is not so suitable for this situation, although Johnson and Cochran (94, 95) have obtained quite good agreement for germanium, making a least squares fit with fifteen force constants to experimentally determined phonon frequencies, elasticity and polarisability parameters. Force constants to fifth nearest neighbours are required, so that they lose their physical significance. More recently, a valence force field method has been applied successfully to germanium (96) by describing the forces in terms of central bond stretching and noncentral bond bending parameters giving a more intuitive model.

III-V and II-VI compounds lie in the region intermediate between ionic and covalent materials. They form covalent tetrahedral bonds, but have an ionic contribution due to charge transfer between the atoms. Shell model fits have been made on GaAs (97, 98) and GaP (99) from neutron scattering measurements, but again the physical significance of the parameters are difficult to interpret. Martin (100) has recently extended a valence force field model to zinc blende materials to predict elastic constants, by including coulomb forces between charged ions. The trends obtained are explained in terms of the ionicity of III-V materials as defined by Phillips and Van Vechten (26).

II-IV-V_2 compounds have the extra complication of having two types of bond, i.e. II-V and IV-V, each having their own degree of ionicity, polarisability and force constants, which makes extension of existing theories difficult due to the number of parameters required. Without neutron scattering data, there is not enough

information for a shell model fitting and this awaits the growth of larger crystals of size at least $1cm^3$. However, insight into at least the type of motion which the ions may be expected to perform has been obtained by comparing the results of infrared and Raman measurements on chalcopyrites, with the phonon dispersion curves of the better understood III-V analogues. $ZnGeP_2$ offers a good example for such a study, being the isoelectronic analogue of the well studied GaP.

3.3.1 Zone centre modes in chalcopyrite

The tetragonal unit cell of space group $I\bar{4}2d$ contains 16 atoms of which 8 are non-equivalent, that is, they do not transform into each other by space group translations. Each of the 8 non-equivalent atoms has 3 degrees of freedom, giving a total of 24 zone centre vibrational modes, 3 of which are acoustic, pure translations.

These zone centre modes are all that need be considered for infrared and Raman scattering experiments. Electromagnetic radiation or inelastically scattered photons only interact with zone centre phonons in single phonon processes since wavevector and energy must be conserved.

The space group translations (77) are listed in Appendix A and the character table for the five irreducible representations are given in Table 3.1, (101).

Table 3.1 Character Table for $I\bar{4}2d$ at $q \simeq 0$

Irrep.	E	$2S_4$	C_2	$2C_2'$	$2\sigma_d$	Symmetry	Activity	Optic	Ac.
A_1	1	1	1	1	1	x^2+y^2,z^2	R	1	
A_2	1	1	1	-1	-1	-	-	2	
B_1	1	-1	1	1	-1	x^2-y^2	R	3	
B_2	1	-1	1	-1	1	xy;z	i.r.,R	3	1
E	2	0	-2	0	0	(xz,yz);(x,y)	i.r.,R	6	1

The activity, Raman or infrared, of each of the representations is shown, with the number of zone centre modes of vibration associated with them. As shown in Chapter 4, only B_2 and E modes are infrared active. B_2 modes produce a net dipole moment in the z-direction, while the doubly degenerate E modes have dipole moments in the x-y plane. A_1, B_1, B_2 and E modes are Raman active as shown in Chapter 5. Thus, all of the modes except the two A_2 vibrations can be studied by these two techniques.

It was shown in section 1.5 that some X and W points of the zinc blende Brillouin zone map to the zone centre in chalcopyrite. The physical significance of this for lattice vibrations, is that modes with zone boundary wavevectors at X and W in zinc blende become phonons of infinite wavelength in chalcopyrite due to the difference in the two cations. In other words, due to the similarity of the two structures, the normal mode vibrations should be very similar, but the difference in the two types of cation can now give X and W motions a net dipole moment which will couple with infrared radiation at the frequency of the mode.

Consider the phonon dispersion curve of GaP in figure 3.1. GaP is the isoelectronic analogue of $ZnGeP_2$ so that the normal modes of $ZnGeP_2$ would be exactly those of GaP if there were no mass differences between germanium and zinc and if the force constants of Zn-P and Ge-P bonds were identical. The effect of the small differences between Zn and Ge masses and force constants is enough to make lattice modes at X and W in GaP, zone centre modes of $ZnGeP_2$. The Zn atoms will have slightly different amplitudes of vibration to the Ge atoms and the differences in charge on the cations due to the different ionicities of the bonds may cause some of these modes to have a net dipole moment and so become infrared active. The difference

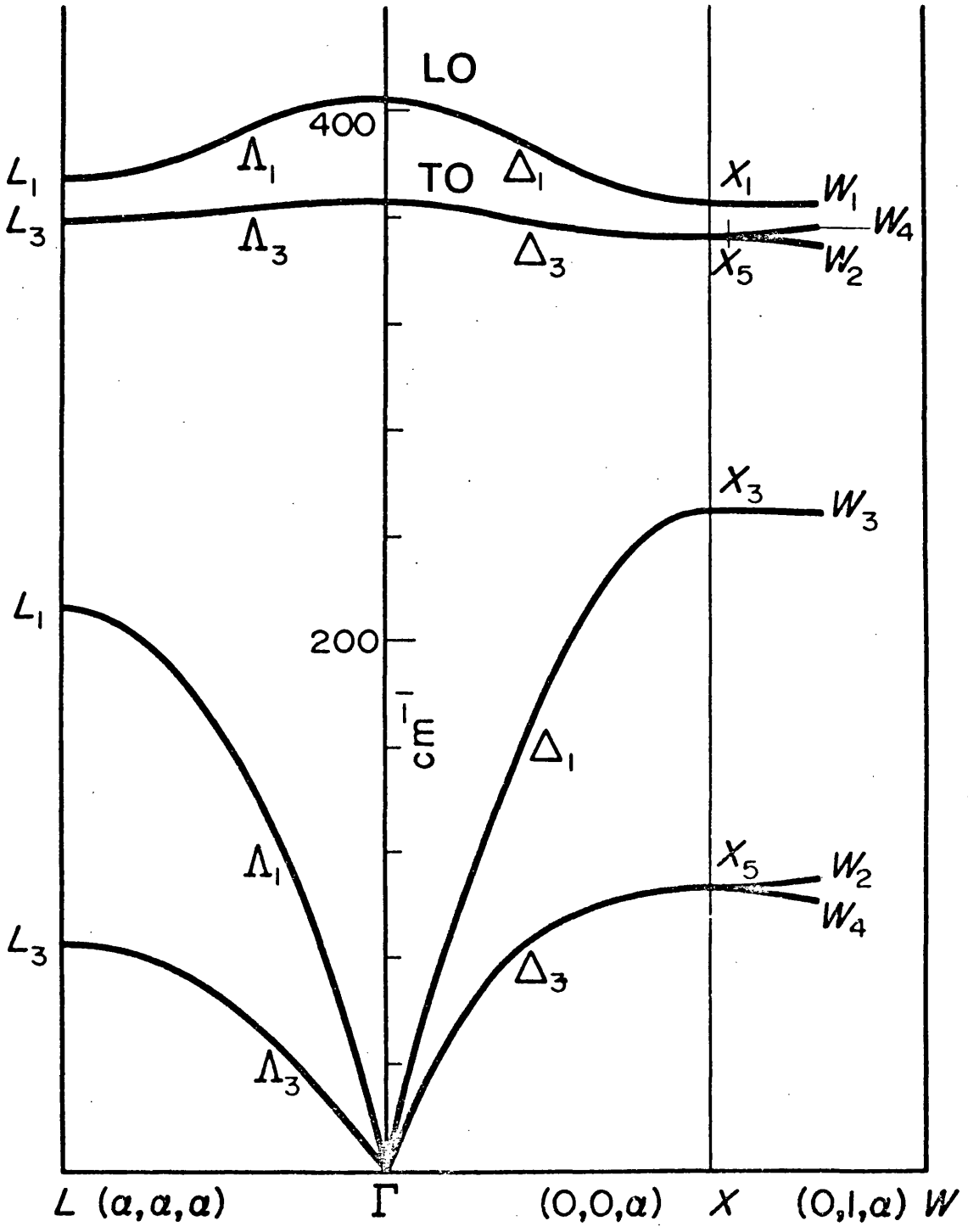

Phonon Dispersion Curve of GaP

Figure 3.1

in the polarisability of the atoms may cause the modes to be Raman active.

The phonon dispersion curves of GaP shown in figure 3.1 were determined by Yarnell et al (99) by neutron scattering. Unfortunately no experimental information is available for the W points for this compound nor indeed any member of the III-V zinc blende family. Germanium is the nearest material for which experimental information is available (102) for the W points. Shell model fits predict that the W branches from X will be almost horizontal in Ge and GaAs(94,95), but this is in disagreement with the measurements on germanium. Thus, figure 3.1 shows only which W points will derive from each of the X points without assuming their positions. Recently, Bettini (103, 104) has used a Keating rigid ion model to calculate W points of GaP, specifically for the present analysis of $ZnGeP_2$. These results will be considered in Chapter 5.

The Γ, X and W zinc blende modes shown in figure 3.1 correspond to chalcopyrite modes given by compatibility relations derived by Sandrock and Treuch (105). These give the following,

Γ_{15} $(E + B_2)$	W_1 $(A_1 + A_2)$
X_1 (A_2)	$W_{4_{opt}}$ (E)
$X_{5_{opt}}$ (E)	$W_{2_{opt}}$ $(B_1 + B_2)$
X_3 (B_1)	W_3 (E)
$X_{5_{ac}}$ (E)	$W_{2_{ac}}$ $(B_1 + B_2)$
	$W_{4_{ac}}$ (E)

The zone centre chalcopyrite modes are thus expected to fall into three frequency ranges. A high frequency group will correspond to zinc blende zone centre and zone boundary optic modes; a mid-frequency group will correspond to the longitudinal acoustic modes, and a low frequency group will correspond to the low frequency transverse acoustic modes of zinc blende.

Due to long range Coulomb interactions, in infrared active modes, the force constant is effectively stiffened for longitudinal modes, causing a shift to higher frequency relative to the transverse modes, for all E and B_2 modes.

In the uniaxial chalcopyrite structure, the short range forces will be anisotropic causing splitting of the Γ_{15} mode with E and B_2 irreducible representations. This splitting has been found in chalcopyrite, as in wurtzite compounds, to be much less than the long range Coulomb TO-LO splitting.

Loudon (106) considers this situation for uniaxial crystals (i.e. when $\omega_{LO} - \omega_{TO} >> \omega_{||} - \omega_{\perp}$, where $||$ indicates a phonon polarised parallel to the c-axis) in the case of general wave propagation direction. If θ is the angle of propagation of the phonon from the c-axis, then mixing of B_2 and E modes will occur such that observed phonon frequencies are given by,

$$\omega^2 = \omega_{||}^{TO^2} \sin^2\theta + \omega_{\perp}^{TO^2} \cos^2\theta$$

and $$\omega^2 = \omega_{||}^{LO^2} \cos^2\theta + \omega_{\perp}^{LO^2} \sin^2\theta$$

This becomes important when, due to the limiting size of the crystals, the incident light cannot be completely polarised parallel to the c-axis as in the present infrared and Raman measurements.

3.3.2 Normal Modes of vibration

No attempt has yet been made to fit the present experimental phonon energies to a model to obtain the amplitudes of the atomic displacements of the chalcopyrite compounds. As described in the previous section, qualitative analysis has been in terms of III-V analogues, and this can be extended to understand the directions of the displacements for the various modes.

Kaminow (101) in his analysis of $ZnSiP_2$ vibrational modes

described each of the irreducible representations in terms of symmetry coordinates derived empirically to be consistent with the transformation properties of the representations. The actual physical modes belonging to any representation are then linear combinations of these arbitrary symmetry coordinates of the representation. The contribution of each symmetry mode to a normal mode is deduced by consideration of the masses expected to be taking part in the motion, and also by comparison with motions in closely related tetrahedrally bonded compounds, such as GaP, ZnP_2, $ZnSnP_2$ and SiC.

Karavaev (107) has used a similar method of analysis, and in general comes to the same conclusions, but disagreement lies in the interpretation of the high frequency modes. Kaminow assumes that there will be two B_2 modes, from his arbitrary symmetry modes, one of which comprises an antiphase motion of Si and P with Zn stationary, and a lower frequency mode with Zn and P moving in antiphase with Si stationary. Two similar motions will have E irreducible representation. Karavaev, chooses as his symmetry modes, the normal modes of the zinc blende lattice, and assumes that the normal modes of the chalcopyrite lattice will be given by a perturbation on these. B_2 and E modes will thus have one dominant high frequency mode corresponding to the motion of the anion sub-lattice in antiphase with the whole cation sub-lattice. If one of the cations is heavier than the other, then its relative displacement will be correspondingly reduced, but this does not imply that it will be stationary. The other high frequency modes will approximately correspond to X and W zone boundary modes of zinc blende, as described in the previous section.

Holah, Webb and Montgomery (108) have clarified the situation by making a more detailed group theoretical analysis, based on a

previous calculation of ion motions in zinc blende materials by Montgomery (109). They also consider the simplified model of a linear tetra-atomic analogue to the chalcopyrite structure to investigate the effect of mass and force constant differences for the cations. The symmetry modes of $ZnGeP_2$ corresponding to GaP normal modes are as follows,

Γ_{15} modes $\Gamma(0, 0,0)$

These are the simplest zone centre modes and have both B_2 and E irreducible representations. The Γ_{15}, B_2 mode is shown in figure 3.2 and produces a very strong dipole moment in the z-direction and is thus infrared active in this polarisation. The doubly degenerate E modes are similar, with atomic displacements in x or y directions. The Γ_{15} acoustic modes are pure translations.

X modes $X(0, 0, 1)$

GaP has six X modes, X_1, $2X_{5_{opt}}$, X_3, $2X_{5_{ac}}$, as shown in figure 3.4. The X_1 is expected to be at higher frequency than X_3 since phosphorus is lighter than gallium, but X_1 will not be observed in infrared reflection or Raman scattering in $ZnGeP_2$. The X_3 and X_5 optic symmetry modes are shown for the chalcopyrite structure in figures 3.5 and 3.6. The X_5 mode shown, has E(x) irreducible representation, but the dipole moments, in spite of differences of mass and charge of the zinc and germanium atoms, will cancel in one unit cell, since the displacements of the two cations are in opposite senses in the [100] direction. The dipole moment for this mode is in the [010] direction, however, by mixing with other modes of E representation, this motion may be observed weakly in the infrared. The X_5 acoustic mode will be similar, but with all the phosphorus atoms moving in the opposite senses, towards two outward moving

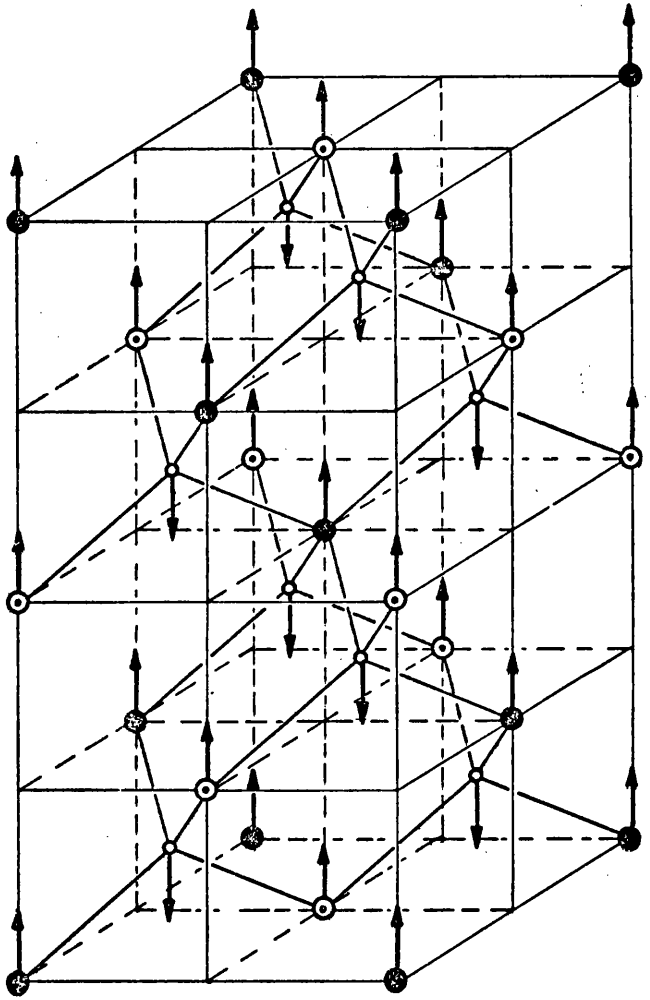

Figure 3.2 $B_2 - \Gamma_{15}$ optic

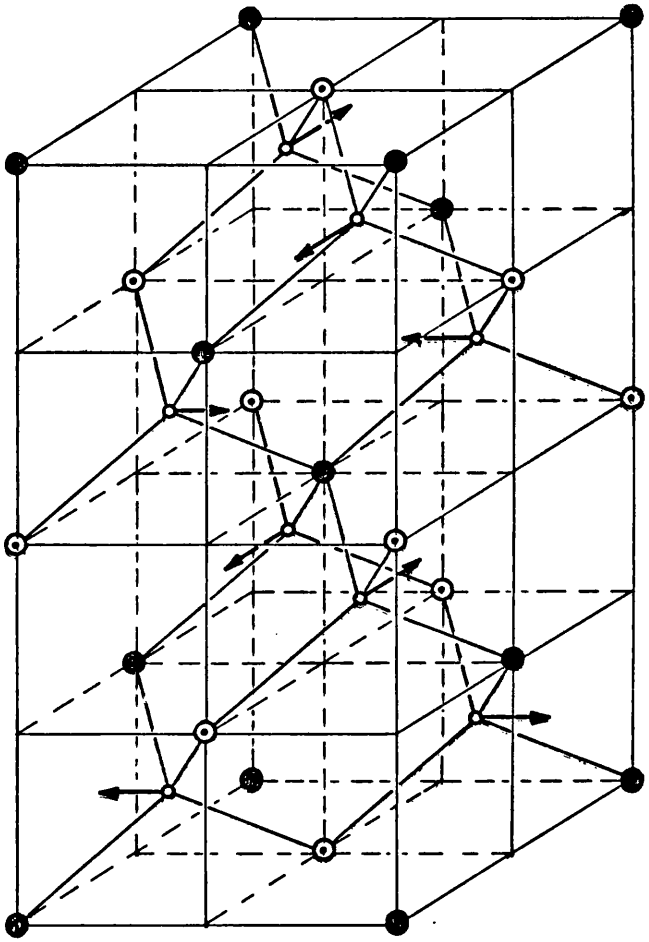

Figure 3.3 $A_1 - W_1$

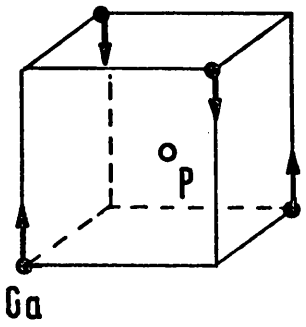

X_3

$m_{Ga} > m_P$

$\Rightarrow \omega_{X_1} > \omega_{X_3}$

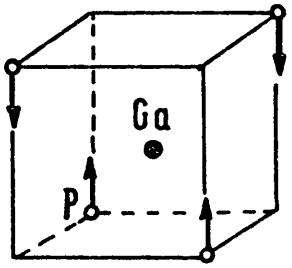

X_1

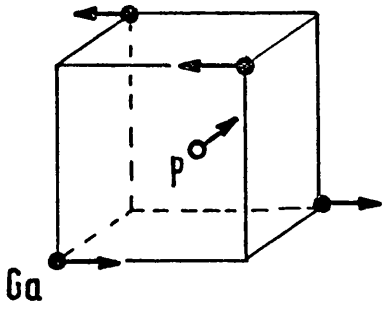

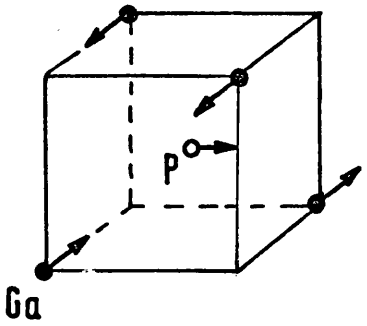

X_5 acoustic

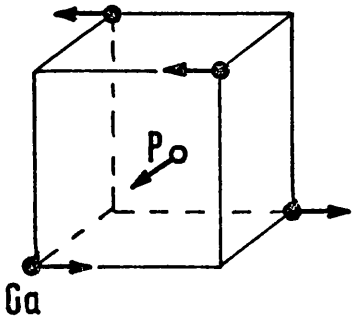

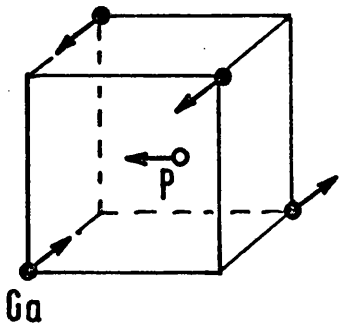

X_5 optic

Figure 3.4 X modes of GaP

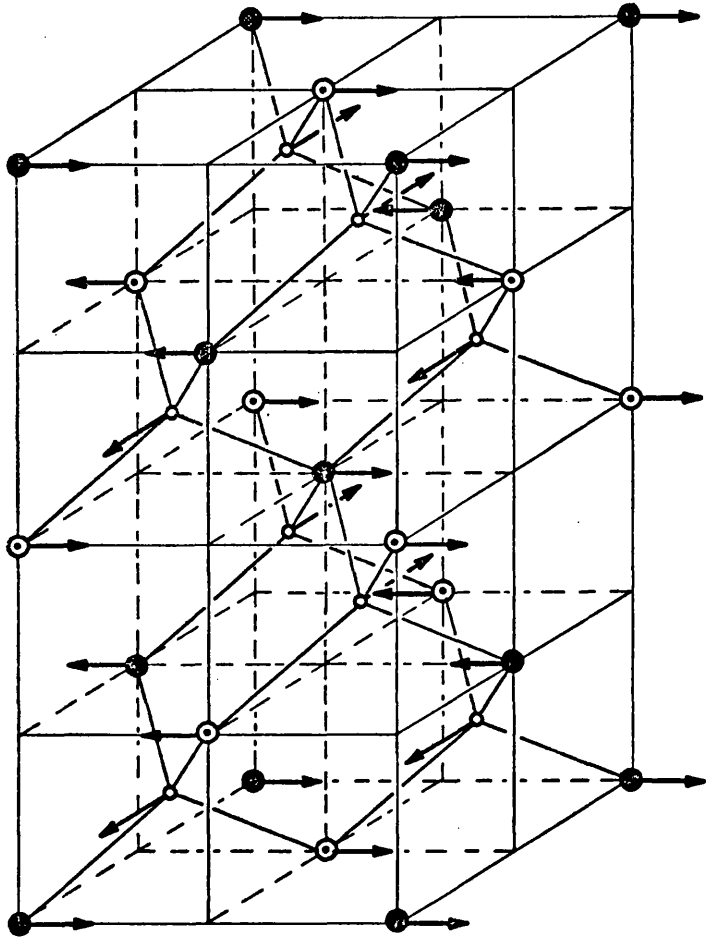

Figure 3.5 E — X_5 optic

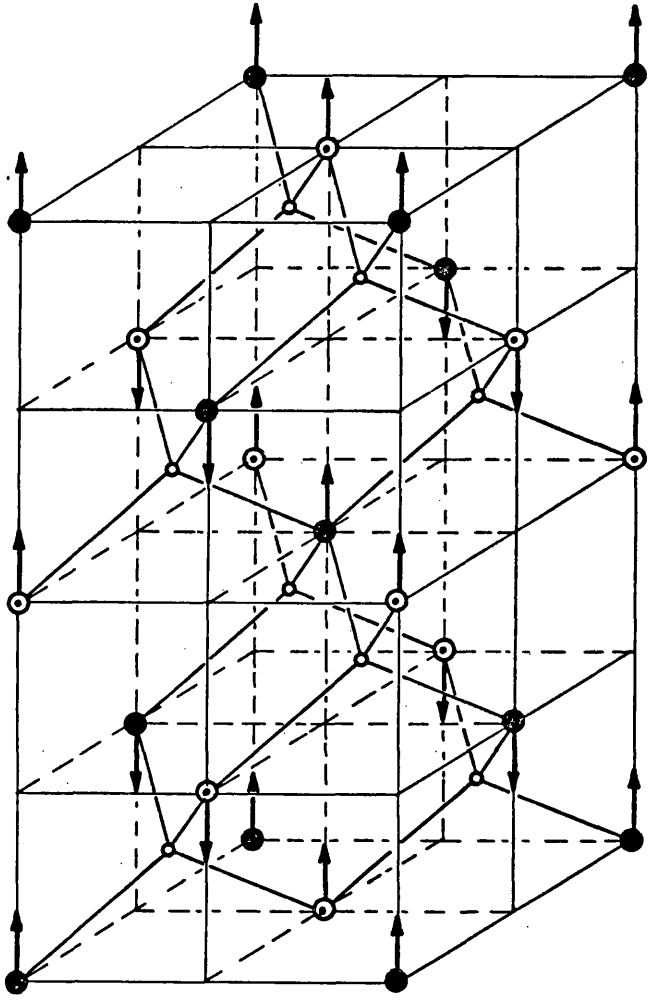

Figure 3.6 B_1 — X_3

cations, explaining the low frequency. The X_3 mode, shown in figure 3.6 will give only weak Raman scattering. The symmetry coordinate is $x^2 - y^2$ for this mode from Table 3.1, but all displacements are along [001] .

W modes $(0, \frac{1}{2}, 1)$ and $(\frac{1}{2}, 0, 1)$

The W modes of GaP are more difficult to map into chalcopyrite modes. Two different W points, $W^a(0, \frac{1}{2}, 1)$ and $W^b(\frac{1}{2}, 0, 1)$ both map to Γ . The $W^a(0, \frac{1}{2}, 1)$ modes are shown in figure 3.7 and all consist of circular motions in the y - z plane. W^b can be obtained from W^a by reflection in the (110) plane and so W^b modes will be similar, but with the senses reversed. The chalcopyrite motions will be a superposition of W^a and W^b motions, which has the effect of linearising all of the GaP W modes by superposition of the two circular motions.

The unique W_1 mode with A_1 representation is shown in figure 3.3. A_1 has symmetry coordinate $x^2 + y^2$; z^2 from table 3.1, and is a strong Raman scattering mode. The effect of the improper transformation, σ_d on W^a is to turn it into W^b with a phase shift of $\pm \pi/2$. The positive sign gives the W_1 (A_1) mode when W^a and W^b are superimposed, while the negative sign gives the inactive W_1 (A_2) mode which is similar to $W_1(A_1)$, except that the phosphorus atoms now move towards a zinc and a germanium instead of two identical cations.

W_2 will similarly be split into modes with B_1 and B_2 representations. The B_1 mode is a motion of phosphorus atoms moving towards two identical cations in the optic mode and should give strong Raman scattering while the B_2 mode, shown in figure 3.9 has the phosphorus moving towards a germanium and a zinc atom and the scattering will be weaker. The $W_2(B_2)$ mode is also infrared active in the z direction

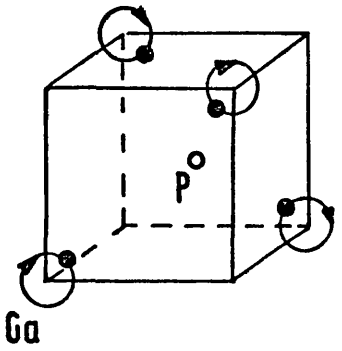

W_3

$m_{Ga} > m_P$

$\Rightarrow \omega_{W_1} > \omega_{W_3}$

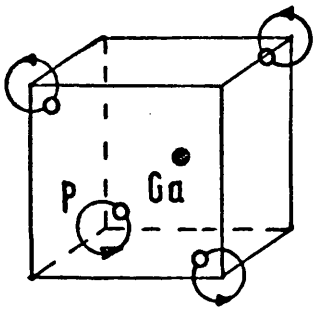

W_1

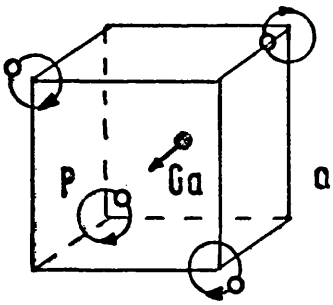

W_2 acoustic

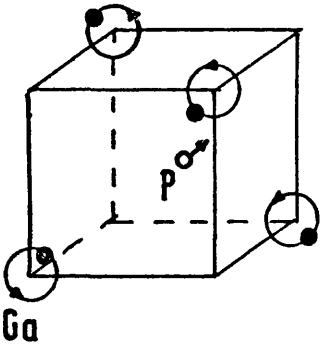

W_4 acoustic

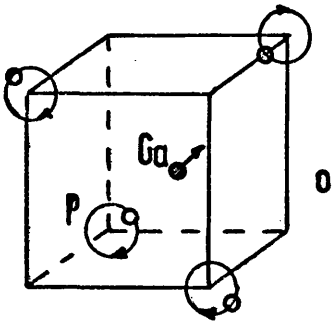

W_2 optic

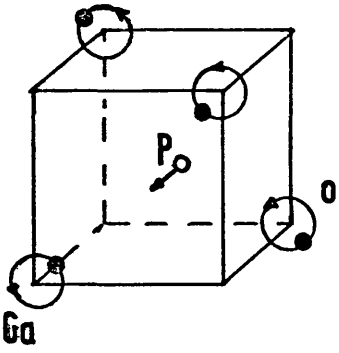

W_4 optic

Figure 3.7 W modes of GaP

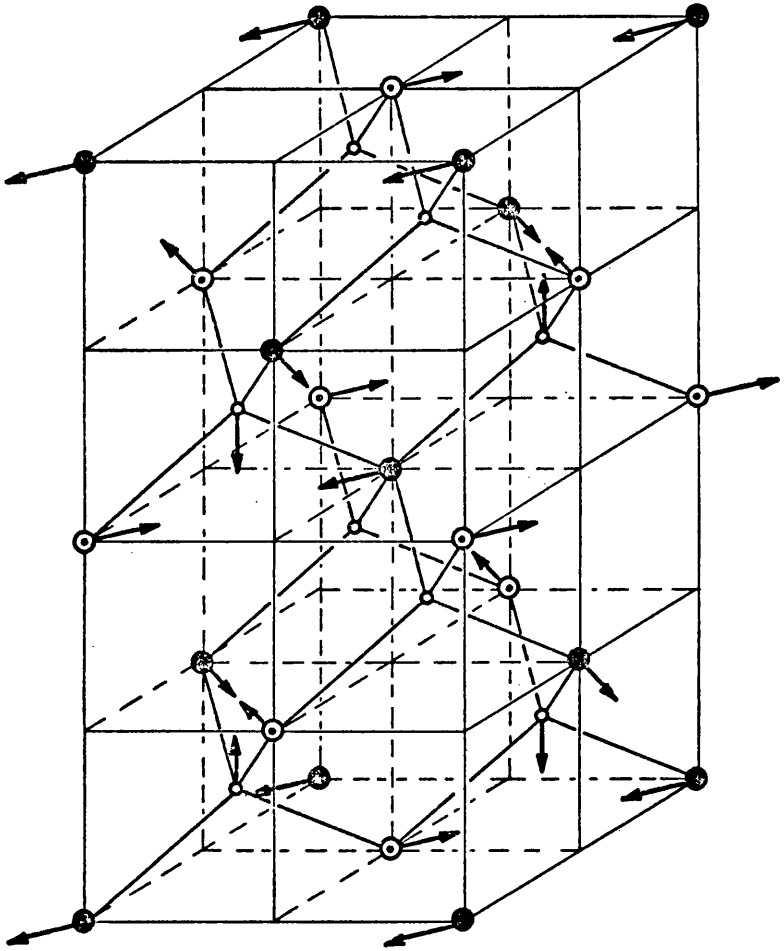

Figure 3.8 E – W_4 optic

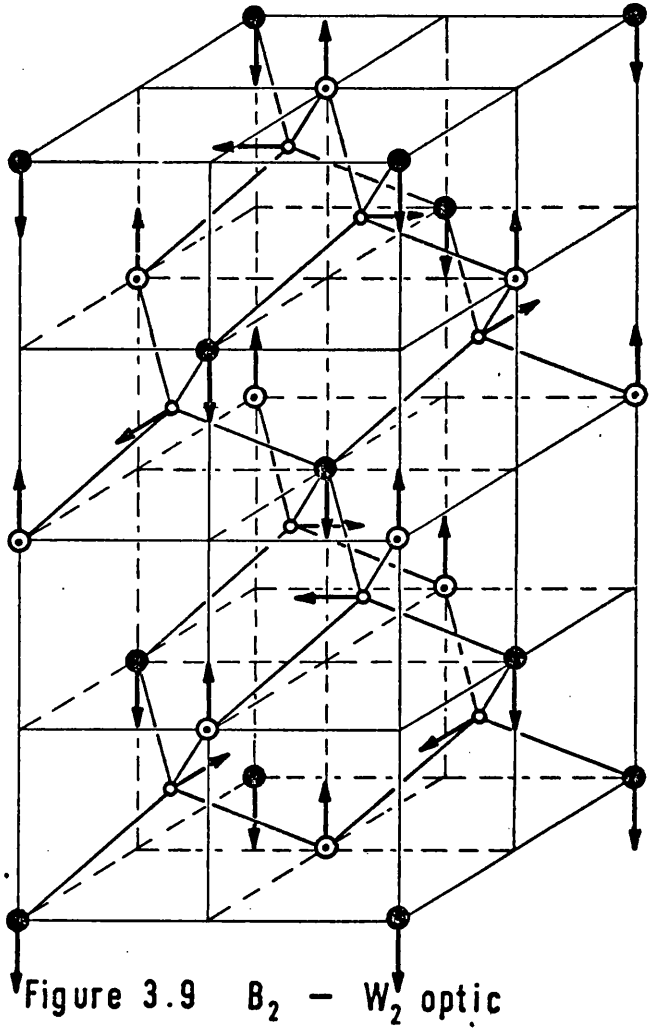

Figure 3.9 B_2 – W_2^1 optic

Table 3.2 Atomic displacements for $ZnGeP_2$ symmetry modes

Atomic positions:

Zn_1 (0 0 0) Zn_2 (0 $\frac{1}{2}$ $\frac{1}{4}$) Ge_1 (0 0 $\frac{\bar{1}}{2}$) Ge_2 (0 $\frac{\bar{1}}{2}$ $\frac{1}{4}$)

P_1 ($\frac{\bar{1}}{4}$ x $\frac{\bar{1}}{8}$) P_2 ($\frac{1}{4}$ $\bar{x}$ $\frac{\bar{1}}{8}$) P_3 ($\bar{x}$ $\frac{\bar{1}}{4}$ $\frac{1}{8}$) P_4 (x $\frac{1}{4}$ $\frac{1}{8}$)

Displacements:

			Zn_1 Zn_2	Ge_1 Ge_2	P_1 P_2 P_3 P_4
1	A_1	W_1			$y_1-y_2-x_3+x_4$
2	A_2	W_1			$x_1-x_2+y_3-y_4$
3	A_2	X_1			$z_1+z_2-z_3-z_4$
4	B_1	X_3	z_1-z_2	z_1-z_2	
5	B_1	$W_{2\ell}$	z_1-z_2	$-z_1+z_2$	$-y_1+y_2-x_3+x_4$
6	B_1	W_{2u}	z_1-z_2	$-z_1+z_2$	$y_1-y_2+x_3-x_4$
7	B_2	Γ_{15}	z_1+z_2	z_1+z_2	$-z_1-z_2-z_3-z_4$
8	B_2	$W_{2\ell}$	z_1+z_2	$-z_1-z_2$	$x_1-x_2-y_3+y_4$
9	B_2	W_{2u}	z_1+z_2	$-z_1-z_2$	$-x_1+x_2+y_3-y_4$
10	E_x	Γ_{15}	x_1+x_2	x_1+x_2	$-x_1-x_2-x_3-x_4$
11	E_x	$X_{5\ell}$	y_1-y_2	y_1-y_2	$-x_1-x_2+x_3+x_4$
12	E_x	X_{5u}	y_1-y_2	y_1-y_2	$x_1+x_2-x_3-x_4$
13	E_x	W_3	$x_1+y_1+x_2-y_2$	$-x_1-y_1-x_2+y_2$	
14	E_x	$W_{4\ell}$	$x_1-y_1+x_2+y_2$	$-x_1+y_1-x_2-y_2$	z_1-z_2
15	E_x	W_{4u}	$x_1-y_1+x_2+y_2$	$-x_1+y_1-x_2-y_2$	$-z_1+z_2$
16	E_y	Γ_{15}	y_1+y_2	y_1+y_2	$-y_1-y_2-y_3-y_4$
17	E_y	$X_{5\ell}$	$-x_1+x_2$	$-x_1+x_2$	$y_1+y_2-y_3-y_4$
18	E_y	X_{5u}	$-x_1+x_2$	$-x_1+x_2$	$-y_1-y_2+y_3+y_4$
19	E_y	W_3	$-x_1+y_1+x_2+y_2$	$x_1-y_1-x_2-y_2$	$-z_3+z_4$
20	E_y	$W_{4\ell}$	$x_1+y_1-x_2+y_2$	$-x_1-y_1+x_2-y_2$	z_3-z_4
21	E_y	W_{4u}	$x_1+y_1-x_2-y_2$	$-x_1-y_1+x_2-y_2$	

while $W_4(E_x)$ shown in figure 3.8 is infrared active in the x direction.

The complete set of 21 vibrational symmetry modes are reproduced from ref (108) in Table 3.2.

3.4 Experimental investigation of phonon spectra

Since 1969, many of the II-IV-V_2 and I-III-VI_2 chalcopyrite materials have been investigated by infrared absorption or reflectivity and by Raman scattering. Crystals are too small at present for neutron scattering measurements.

Initial infrared investigations were by the Russian group working at the A.F. Ioffe Institute in Leningrad. Zlatkin et al (110, 111) carried out unpolarised reflectivity measurements on $ZnSnP_2$ in both chalcopyrite and zinc blende phases. Only one strong absorption band was observed in both phases with the chalcopyrite peak at slightly higher energy (Ch: $\omega_{TO} = 327cm^{-1}$, $\omega_{LO} = 368cm^{-1}$; z.b: $322cm^{-1}$, $362cm^{-1}$). $CdGeAs_2$ was compared in its chalcopyrite and amorphous phases (112-114), also by unpolarised reflection. One strong peak was observed in the chalcopyrite structure with several small peaks at lower energy. Similar measurements on $CdSnP_2$ (115) gave four peaks with no dominant band. Infrared absorption above the Restrahl region was investigated by Boltovets (116) in $CdGeAs_2$, $ZnSnP_2$, $ZnSiAs_2$ and $CdGeP_2$ to observe the two phonon combination bands. In the case of $CdGeP_2$, it was concluded that zone boundary phonons exist at $\omega_{TO} = 376cm^{-1}$ and $\omega_{LO} = 359cm^{-1}$.

A much clearer picture of the phonon spectra of the chalcopyrite structure was obtained by Kaminow's Raman scattering investigation on oriented single crystals of $ZnSiP_2$ (101). By interpretation of

the spectra from the scattering selection rules, the observed Raman modes were thought to be 1 A_1 + 1 B_1 + 2 B_2(T) + 2 B_2(L) + 2E(T) + 2E(L) + 4E(L+T) where L+T denotes an unsplit polar mode. Thus, only two B_1 and one B_2 modes predicted by theory were not observed. This work formed the basis for interpretation by other workers. Polarised reflection measurements were carried out on $ZnSiP_2$ (60, 117) with the observation of five of the six E modes and two of the three B_2 modes. Markov (118) observed four E and two B_2 modes in $CdGeP_2$ and in $ZnGeP_2$ (119) five E modes and two B_2. Koschel et al investigated $ZnSiAs_2$(120) and Bettini et al $CdSiP_2$(121), by both Raman and infrared reflectivity. In $ZnSiAs_2$ one predicted B_1 mode and one E mode were missing, while in $CdSiP_2$ only the B_1 mode escaped observation. Two phonon combination bands have also been studied in $ZnSiP_2$ and $CdSiP_2$ by Bhar and Smith (122). Chapter 4 describes polarised infrared reflectivity measurements on $ZnGeP_2$ and $CdGeP_2$, the results of which were reported in refs. (123, 124). This is followed by a Raman scattering investigation of the same materials in Chapter 5 (104).

Since lattice modes in I-III-VI_2 compounds will be very similar to II-IV-V_2's, it is worthwhile to compare these materials also with the II-IV-V_2 family. Less work has been done on the I-III-VI_2 materials, although both Raman and polarised infrared measurements have been made on most of those studied. Holah et al. has observed all predicted modes in $AgGaS_2$ (108, 125, 126). These results and infrared results of Baars and Koschel on $CuGaS_2$ (127) agree with Raman measurements on $AgGaS_2$, $CuGaS_2$ and $AgGaSe_2$ and infrared measurements on $AgGaS_2$ by Van der Zeil et al (128). Koschel et al have also studied $CuAlS_2$(129) by infrared reflection, absorption and Raman scattering. Finally, two phonon combination bands were observed by

Bhar et al (122) in $CuAlS_2$, $CuAlSe_2$, $CuGaS_2$, $CuGaSe_2$, $AgGaS_2$, $AgGaSe_2$, and $AgInS_2$.

CHAPTER 4 Infrared Dielectric Dispersion

4.1 Introduction

The modes of vibration of a solid have frequencies in the infrared region of the electromagnetic spectrum. If the displacements of the atoms for any of the modes in the long wavelength limit produce a net dipole moment, electromagnetic radiation of this frequency can interact with the lattice (93). Very little absorption is observed at the frequency of the Γ_{25}' mode in the elemental semiconductors due to the absence of charge on the covalently bonded atoms, but a large absorption band may be observed in partially ionic III-V materials due to the opposite relative displacements of the negatively charged anions to the positive cations in the Γ_{15} zone-centre mode (50). As II-IV-V_2 chalcopyrite materials have several modes of vibration which produce finite dipole moments by virtue of the charged ions, a study of the lattice absorption can give information on the frequencies, strengths and damping of the modes.

The present chapter is concerned with the infrared dielectric dispersion of $ZnGeP_2$ and $CdGeP_2$. The measurements were taken in reflection, as the lattice absorption is large. Fresnel's equation (130) was used together with both classical dispersion theory and Kramers-Krönig integration to obtain optical constants from the reflectivity measurements (130). The character table for $I\bar{4}2d$, Section 3.3.1, shows that only transformations of the B_2 irreducible representation leave displacements in the z direction unchanged and thus, z is a basis of the representation. A net dipole moment in this direction may result and B_2 modes are isolated by reflection of light polarised parallel to the c-axis of the crystal. Similarly, only the E modes give dipole moments in the x-y plane, and so light polarised perpendicular to the c-axis will show absorption peaks due

to these motions.

The work described here was carried out at Heriot-Watt University, Edinburgh with Dr. G.D. Holah (124) by permission of Professor S.D. Smith.

4.2.1. Infrared reflectivity

Transmission and reflection of electromagnetic radiation at the surface of a solid involve both the dispersion and absorption of the material according to Maxwell's equations. The complex index of refraction, $N = n' + in''$ describes dispersion and absorption in the material and is thus a function of incident light frequency. If the incident e.m. radiation has an electric vector given by,

$$E = E_o . \exp 2\pi i c . \omega (t - \frac{x}{c}) \qquad 4.1$$

where c = the velocity of light in vacuum in cm per sec and ω = the frequency in cm^{-1} (the unit normally used in infrared spectroscopy), then, in the material at position x (cm),

$$E(x) = E_o \exp 2\pi i c.\omega(t - \frac{n'x}{c}) \exp.\left[- \frac{2\pi c\omega . n''x}{c} \right] \qquad 4.2$$

and the phase velocity is, $v = \frac{c}{N}$.

The last term in 4.2 is a damping factor and n'' is known as the extinction coefficient, giving the absorption in the material from,

$$\alpha = 4\pi \omega . n'' \qquad 4.3$$

The optical conductivity is given by,

$$\sigma = 4\pi \varepsilon_o . c . \omega . n' . n'' \qquad 4.4$$

For normal incidence, Fresnel showed that the reflectivity, R, may be written in terms of n' and n'',

$$R = \frac{(n' - 1)^2 + n''^2}{(n' + 1)^2 + n''^2} \qquad 4.5$$

The complex dielectric constant is defined by,

$$\varepsilon = N^2 \qquad 4.6$$

where

$$\varepsilon = \varepsilon' + i.\varepsilon'' \qquad 4.7$$

Thus, $$\varepsilon' = n'^2 - n''^2 \qquad 4.8$$

$$\varepsilon'' = 2.n'.n'' \qquad 4.9$$

To obtain the optical constants from the measured reflectivity, two standard methods are available, (a) classical dispersion theory, and (b) Kramers -Krönig integration.

4.2.2 Classical dispersion theory

Classical dispersion theory is a phenomenological explanation of the dependence of the optical constants on frequency (93). The atoms of the solid are considered as an assembly of charged Lorentzian harmonic oscillators, which are set into forced vibration by the radiation. If the ions are first of all considered to be point charges, then the equation of motion of a vibrating atom of effective charge, e* is,

$$\ddot{x} + \gamma.\dot{x} + \omega_o^2 x = -\frac{e^*.E_o.\exp(-2\pi i\ c.\omega.t)}{m} \qquad 4.10$$

where $E_o.\ \exp(-2\pi i\ c.\omega.t)$ is the x component of the electric field,

$-\ m.\gamma.\dot{x}$ represents the damping,

and $-\ m.\omega_o^2.x$ is the restoring force.

The solution for forced oscillations of frequency, ω, is

$$x = \frac{(-e^*\ E_o / 4\pi^2.c^2.m).\ \exp(-2\pi i\ c.\omega.t)}{\omega_o^2 - \omega^2 - i\ \omega.\gamma} \qquad 4.11$$

The electric polarisation, P_x is $-N.e^*.x$ for N atoms/unit volume, and the dielectric constant, $\varepsilon\ (\omega)$ is given by,

$$\varepsilon(\omega) = 1 + \frac{P_x}{\varepsilon_o.E_x} \qquad 4.12$$

Hence,

$$\varepsilon(\omega) = 1 + \frac{N.e^{*2}/4\pi^2.c^2.m.\varepsilon_o}{\omega_o^2 - \omega^2 - i\ \gamma.\omega} \qquad 4.13$$

This still holds for solids with more than one type of atom. For a diatomic solid, m and x above are defined by,

$$m = \frac{m_A . m_B}{m_A - m_B} \qquad 4.14$$

and $$x = x_A - x_B \qquad 4.15$$

Treating the atoms as point charges in this way does not take account of the polarisation in each ion caused by the relative displacement of the outer electron shell to the positive ion core due to the electric field, i.e. the polarisability, α. The contribution of this to ε is almost constant up to optical frequencies ($\sim 10^{15} sec^{-1}$), since the electron shell responds much more quickly than the ion cores. Thus, a constant, ε_∞ is added to the ionic contribution to represent the polarisability giving,

$$\varepsilon(\omega) = \varepsilon_\infty + \frac{N.e^{*2} \; / \; 4\pi^2 c^2 . m . \varepsilon_o}{\omega_o^2 - \omega^2 - i.\gamma.\omega} \qquad 4.16$$

Finally, putting $\omega = 0$, we see that,

$$\frac{N.e^{*2}}{4\pi^2 c^2 . m . \varepsilon_o} = \left\{ \varepsilon(0) - \varepsilon_\infty \right\} \omega_o^2$$

thus,
$$\varepsilon(\omega) = \varepsilon_\infty + \frac{\omega_o^2 \left\{ \varepsilon(0) - \varepsilon_\infty \right\}}{\omega_o^2 - \omega^2 - i\gamma.\omega} \qquad 4.17$$

$\omega_o^2 . \left\{ \varepsilon(0) - \varepsilon_\infty \right\}$ is termed the strength of the mode of vibration and is given the symbol, S. The contribution of more than one resonance is given by summation over the total number of oscillators,

$$\varepsilon(\omega) = \varepsilon_\infty + \sum_j \frac{S_j}{\omega_{oj}^2 - \omega^2 - i\gamma_j.\omega} \qquad 4.18$$

In a uniaxial crystal, two dielectric constants can be defined (106) for electric fields parallel and perpendicular to the optic axis. Thus, in chalcopyrite materials, a dielectric constant, $\varepsilon_{||}$, is obtained for fields parallel to the c-axis by summation over the B_2 modes, while summation over E modes gives $\varepsilon_\perp$.

The problem now lies in obtaining values for the parameters ε_∞, ω_{oj}, S_j and γ_j in order to produce the dispersion of $\varepsilon(\omega)$ which, when substituted in Fresnel's equation, 4.5, will agree with the experimentally determined variation of reflectance with frequency. This is normally achieved by making a computer least squares fit, allowing the parameters of equation 4.18 to vary.

4.2.3 Kramers-Krönig analysis

The Kramers-Krönig relations are applicable to phenomena which can be described by the absorption and phase shift of waves at an interface. Originally used in electrical filter design (131), Kramers and Krönig applied them to optical phenomena (132). The relations are causal in that an effect at a point in the material, for instance the polarisation, at a given time, t=0 can only depend on the fields at that point for $t \leq 0$. Thus, the polarisation can be described by a response function,

$$\underline{P}(t) = \int_0^\infty F(t').\ \underline{E}(t-t').dt' \qquad 4.19$$

Substituting $E(t) = E_o \exp 2\pi ci.\omega.t$ and using equation 4.12 gives the response function in terms of $\varepsilon'(\omega)$ and $\varepsilon''(\omega)$ by a Fourier transformation. Imposing the causality condition, $F(t) = 0$ for $t \leq 0$ gives

$$\varepsilon'(\omega) - 1 = \frac{2}{\pi} \int_0^\infty \frac{\omega' .\varepsilon''(\omega').d\omega'}{(\omega'^2 - \omega^2)}$$

$$\varepsilon''(\omega) = \frac{2}{\pi} \int_0^\infty \frac{\omega.\varepsilon'(\omega).\ d\omega'}{(\omega'^2 - \omega^2)} \qquad 4.20$$

Again, Fresnel's equation, 4.5, can be used to obtain the optical constants from the measured reflectivity by introducing the phase shift on reflection, θ,

$$r = |r|.e^{i\theta} \qquad \text{where } R = |r|^2$$

$$\theta(\omega) = \frac{2\omega}{\pi} \int_0^\infty \frac{\ln\{r(\omega') - r(\omega)\}.d\omega'}{\omega^2 - \omega'^2} \qquad 4.21$$

and

$$n' = \frac{1 - r^2}{1 + r^2 - 2r.\cos\theta} \; ; \; n'' = \frac{2r.\sin\theta}{1 + r^2 - 2r.\cos\theta} \qquad 4.22$$

$$\varepsilon' = n'^2 - n''^2 \; ; \; \varepsilon'' = 2n'.n''$$

This integration is taken over as large a range of frequency as possible by extrapolating the reflectivity to zero and to optical frequencies where the optical constants are known.

4.3.1 Sample preparation

Crystals of $ZnGeP_2$ and $CdGeP_2$ grown from lead solution gave large enough faces for infrared reflectivity measurements. A $ZnGeP_2$ crystal with a $(\bar{1}\bar{1}2)$ face of size 8 x 6 mm^2 was chosen. This crystal had small $(0\bar{1}1)$ and $(\bar{1}01)$ faces on the edge of the large face, determined by Laué X-ray photographs. These edges were used to align the sample with the polariser as they lie on the projection of the c-axis onto the $(\bar{1}\bar{1}2)$ plane. The crystal face was highly reflecting and used without any polishing. The only treatment to the crystal was the $CH_3COOH : H_2O_2$ etch used to remove the lead solvent, and a ten second rinse in concentrated hydrochloric acid to remove the lead acetate precipitate.

A crystal of $CdGeP_2$ of size 8 x 4 x 0.5 mm^3, also with a large $(\bar{1}\bar{1}2)$ face was chosen, but in this case, polishing was required. A polishing machine was used, which involved an initial polish with 6 micron diamond paste on a solder lap, followed by a 1 micron paste.

Both crystal surfaces were cleaned with methanol just before measurements were taken. Use of the $(\bar{1}\bar{1}2)$ faces does not allow complete polarisation of the light along the c-axis. Only 2/3 of the intensity lies along this plane, while complete polarisation is obtained in the x-y plane.

4.3.2 Optical systems

Two spectrometers were used to cover the wavelength range from 4 to 250μm. ($40cm^{-1}$ to $2500\ cm^{-1}$). For the long wavelength range, $40cm^{-1}$ to $400cm^{-1}$, a Beckmann RIIC FS720 interferometer was used. This instrument is of the Michelson interferometer type having a 125 watt high pressure mercury arc source with the light chopped at 12.5Hz. The beam was divided by a "Melinex" (polythene tetraphthalate) beam splitter of 6μm thickness (40 to $480cm^{-1}$) and subsequently recombined after reflection from the two plane Michelson mirrors. A reflecting module was attached, with a small 10^{o} angle of incidence, and the reflected light detected by a Xe filled Golay detector. One mirror was driven by a piston and cylinder, and a Moiré fringe system was used for measuring the mirror displacement in units of 4μm. The whole apparatus was evacuated to avoid atmospheric absorption bands.

An A.I.M. grid polariser was inserted before the sample to give $\sim$ 99% polarisation. A movement of + 2 mm to -2 mm. was generally used giving a resolution of $5cm^{-1}$, with a scanning speed of 5μm/sec. The fringes recorded after reflection from the sample were compared with those from a silvered mirror, and a Fourier transformation taken using an FTC 100 analogue computer with digital storage facilities.

For the range above $400\ cm^{-1}$, a Grubb-Parsons Spectrometer was used. This is a double beam, single grating spectrometer using a Nernst filament light source, which is switched between sample beam and reference beam. The light was polarised by a Perkin-Elmer gold wire polariser before reflection from the crystal at 10^{o} angle of incidence. The intensity was then measured on a Golay detector.

The travel on a feedback mechanical attenuator in the reference beam recorded the amount of light reflected when a null reading between reference and sample intensities was obtained. This was compared with the amount of light reflected from a front silvered mirror to obtain the reflectance of the sample. The resolution of this instrument was 4 cm^{-1}.

4.4.1. Infrared reflectivity results

Reflectivity measurements are presented for the two polarisations of $ZnGeP_2$ in figures 4.1 (a) and (b). As the radiation is only partially polarised parallel to the c-axis, the B_2 modes carry a small E mode contribution. In the low energy range, a straight line was drawn through small peaks which appeared at the same frequency as the observed peaks in the $E \perp c$ configuration. The high energy B_2 modes will be slightly modified by mixing with the E modes. The lowest energy peak in figure 4.1 (b) at $80cm^{-1}$ is probably due to an absorption in the polythene window of the interferometer. No evidence of a mode was observed here in Raman scattering measurements, section 5.4, and so it has been ignored in the analysis.

This leaves two closely spaced B_2 modes in the 300 to $400cm^{-1}$ range which would appear to correspond to the high frequency Γ_{15} and W_2 optic modes of GaP. The third predicted B_2 mode not observed must be the W_2 zone boundary acoustic mode. In the E configuration, four of the six predicted modes were observed. Comparison of their frequencies with the phonon dispersion curve of GaP in figure 3.1 indicates that the three closely spaced high energy modes may be due to the optic Γ_{15}, W_4 and X_5 modes of GaP, while the mode at $200cm^{-1}$ will correspond to the longitudinal acoustic W_3 mode. Thus, the low frequency X_5 and W_4 modes have escaped observation.

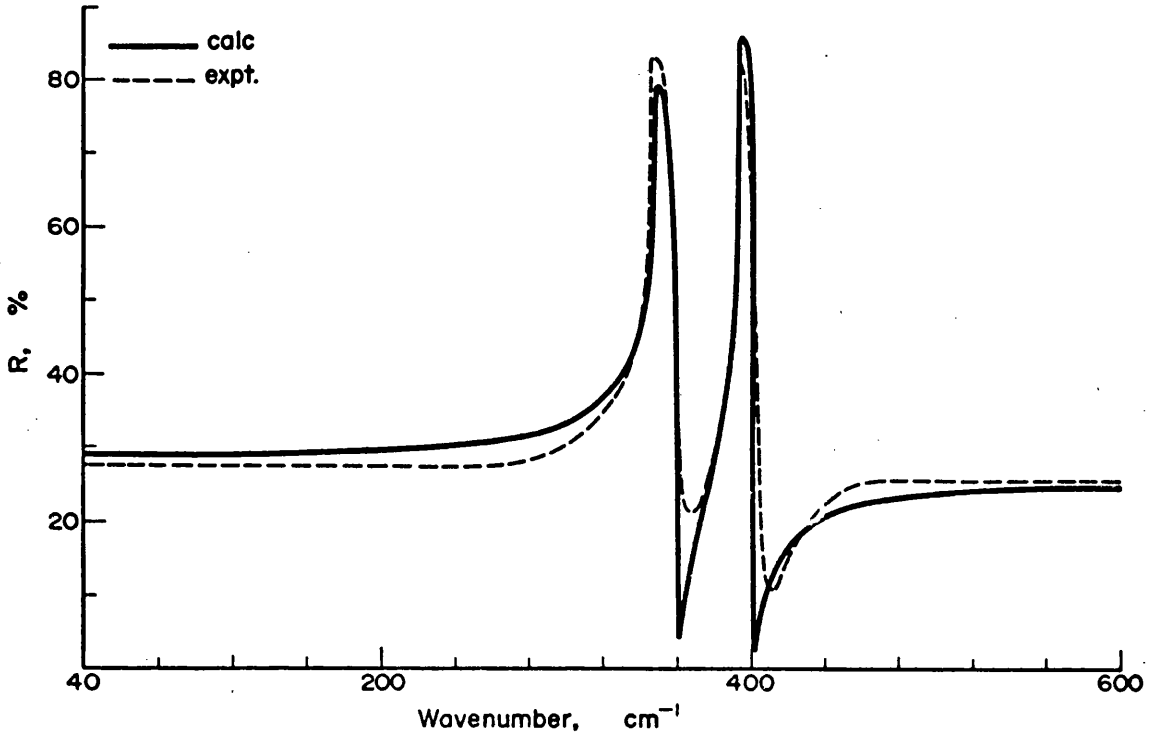

(a). Experimental and calculated reflectivity of the B_2 modes of $ZnGeP_2$.

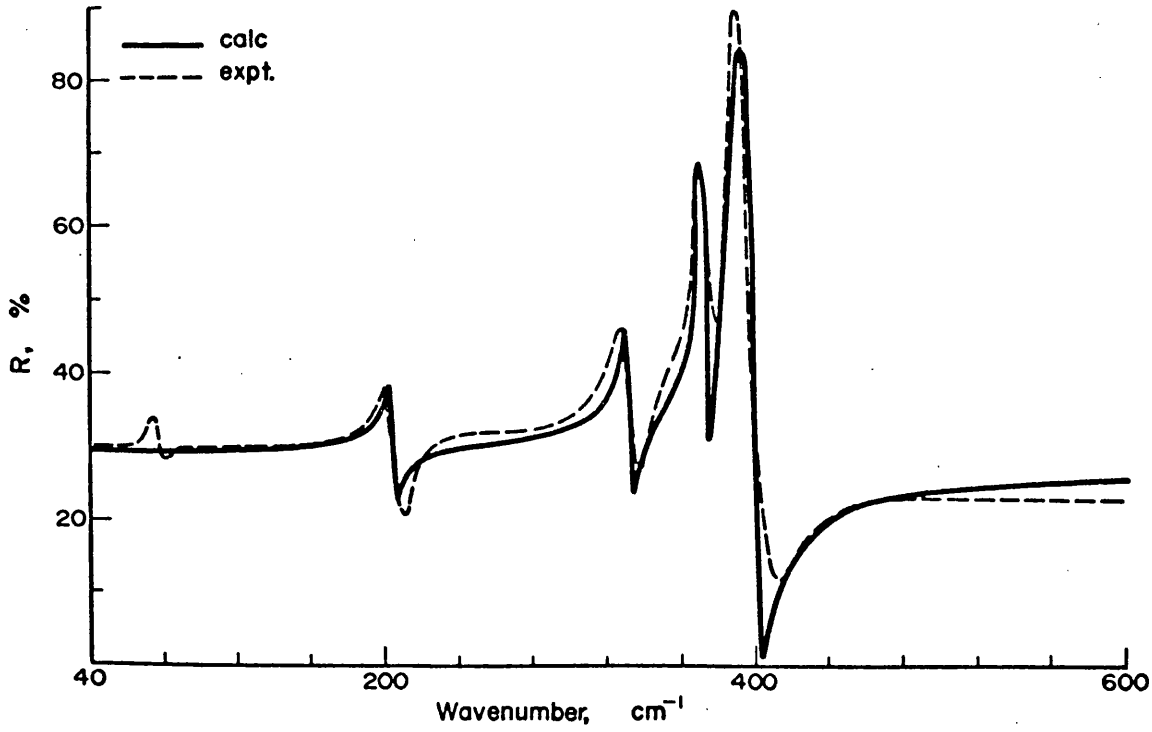

(b). Experimental and calculated reflectivity of the E modes of $ZnGeP_2$.

Figure 4.1

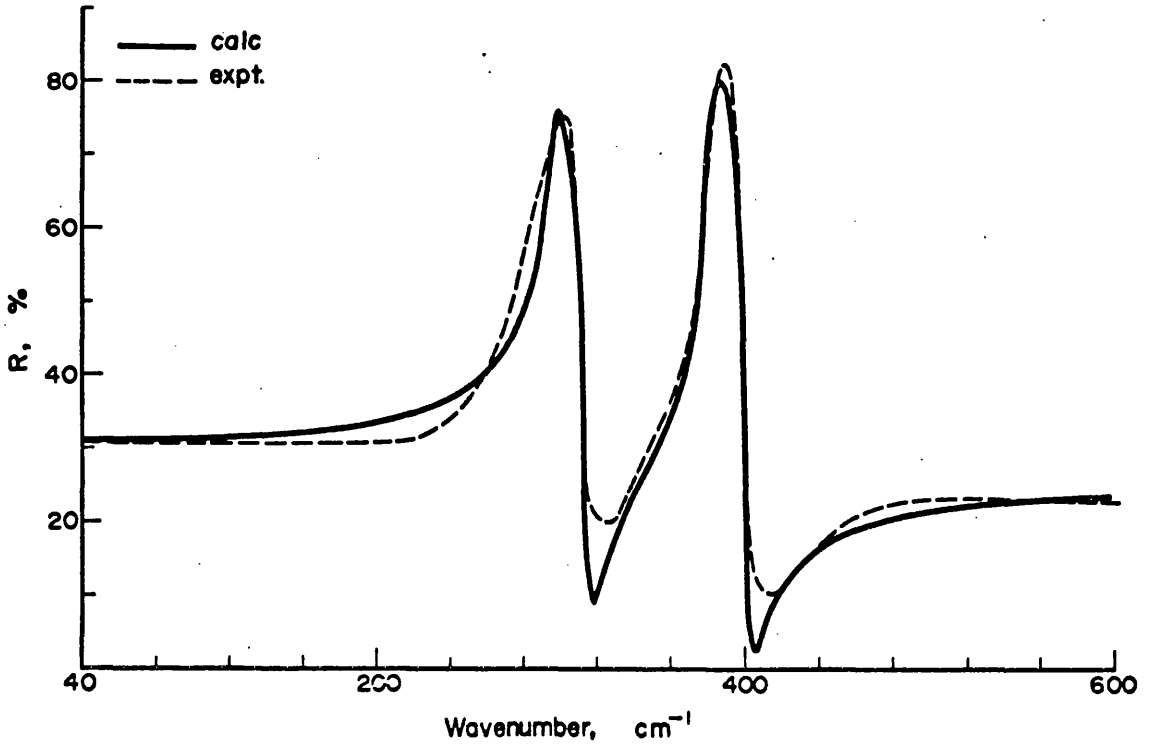

(a). Experimental and calculated reflectivity of the B_2 modes of $CdGeP_2$.

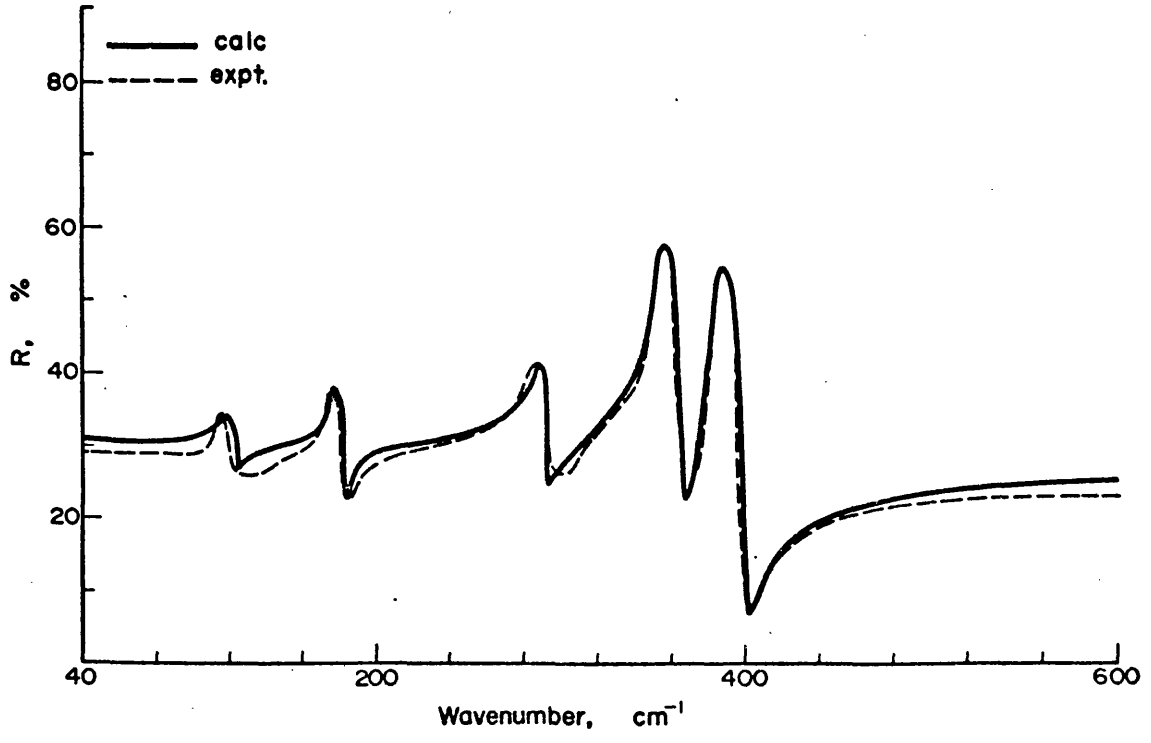

(b). Experimental and calculated reflectivity of the E modes of $CdGeP_2$.

Figure 4.2

The results for $CdGeP_2$ in figures 4.2(a) and (b) are similar and can be interpreted in the same way. The highest B_2 and E modes are very close to the highest energy modes of $ZnGeP_2$. The effect of the heavier cadmium atom is greater at lower energies. In this case, five E modes were observed. The additional low energy mode will be one of the zone boundary transverse acoustic modes of GaP with E irreducible representation, X_5 or W_4.

A least squares fitting computer programme written by G. Peckham (133) was used to fit the classical dispersion equation 4.18 with Fresnel's equation 4.5 for each polarisation by free adjustment of the mode parameters, ω_j, S_j and γ_j. The high frequency dielectric constants were taken from work by Boyd (55, 56) on the measurement of the refractive indices below the fundamental absorption edge in $ZnGeP_2$ and $CdGeP_2$ by the prism method. His results are shown in figures 4.3(a) and (b) and the values of the high frequency dielectric constant were taken at 5μm, near to the points of inflection of the curves.

The reflectivity fits are superimposed on the measured reflectivity plots of figures 4.1 and 4.2 for comparison, and the final fitting parameters are listed for $ZnGeP_2$ in Table 4.1 and for $CdGeP_2$ in Table 4.2. The calculated dielectric constants for real and imaginary parts, are plotted in figures 4.4 and 4.5, while the real and imaginary refractive indices are shown in 4.6 and 4.7. for the two materials.

Due to the transverse nature of electromagnetic radiation, the strong interaction is with the transverse optical phonons and thus the resonant frequency of equation 4.18 would be ω_{TO} if damping were not present. ω_{TO} is given by the position of the maximum in the

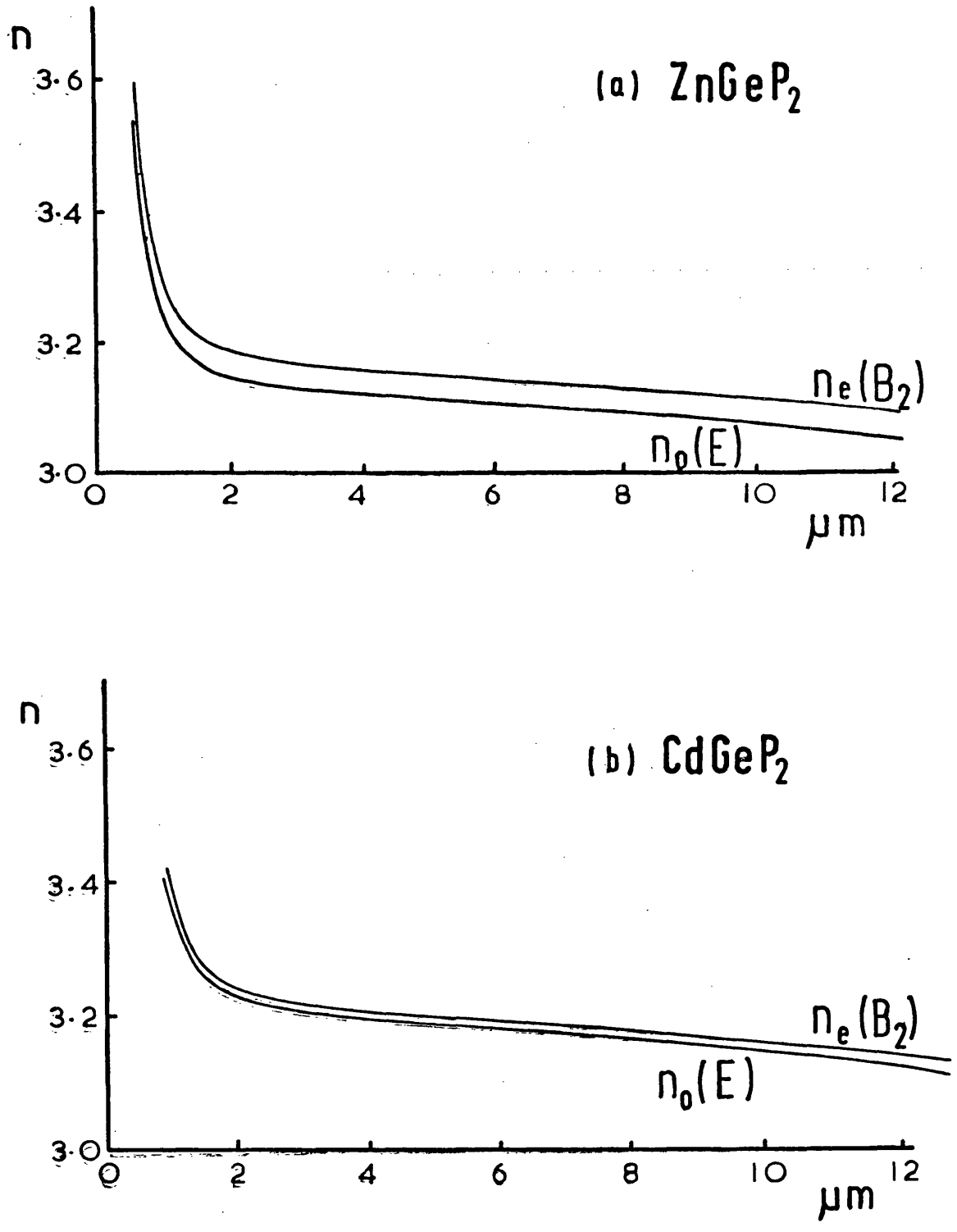

Figure 4.3 Refractive index vs. wavelength below the band gap

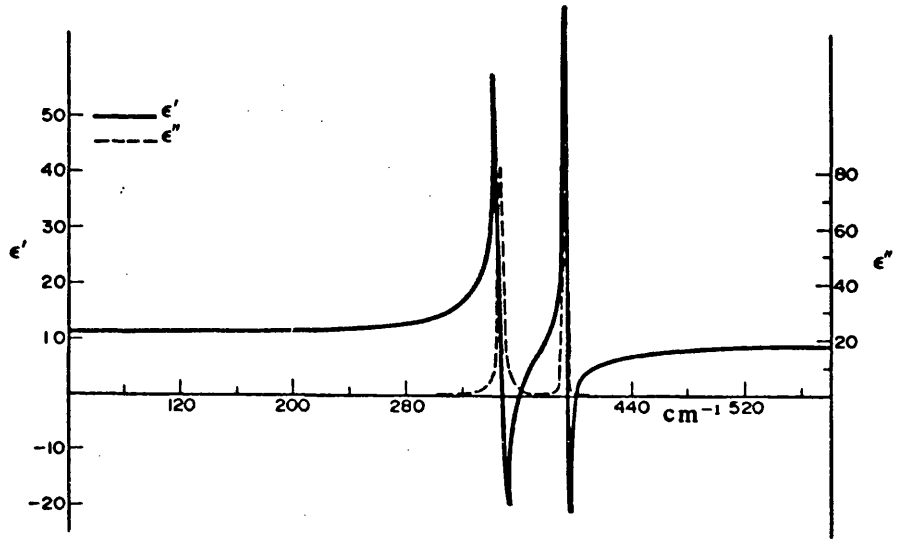

Fig. 4(a). Real and imaginary parts of the dielectric constant of the B_2 modes of $ZnGeP_2$.

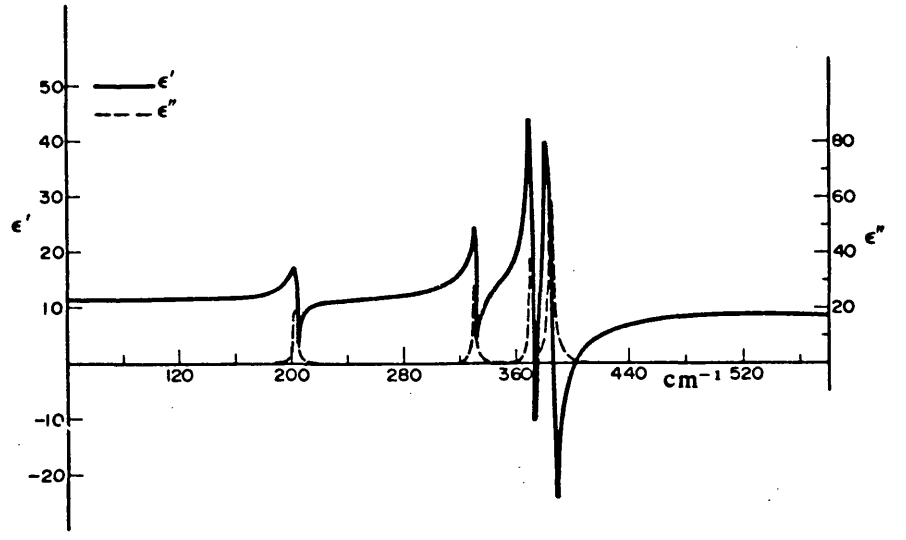

Fig. 4(b). Real and imaginary parts of the dielectric constant of the E modes of $ZnGeP_2$.

Figure 4.4

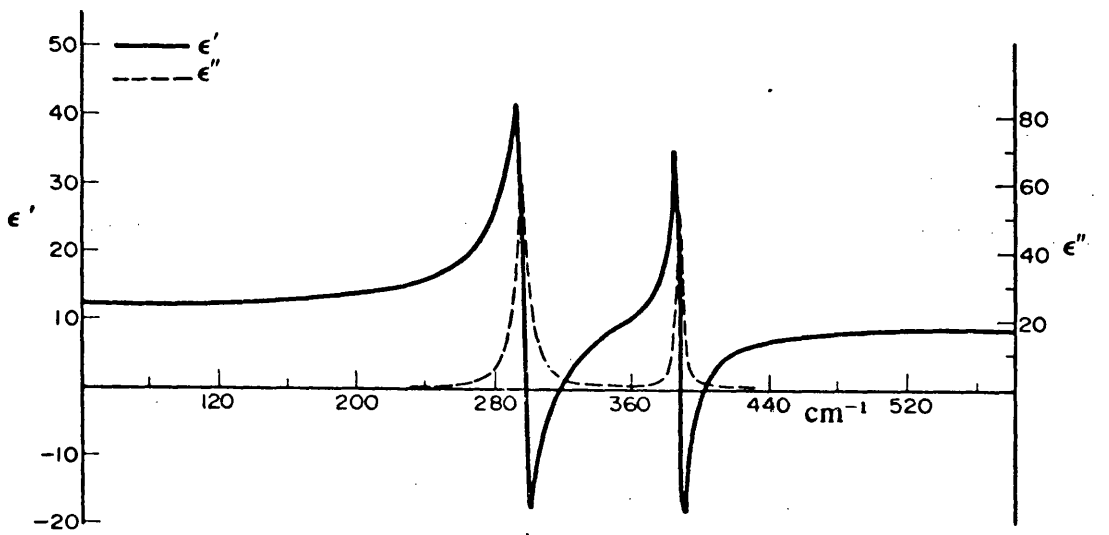

Fig. 5(a). Real and imaginary parts of the dielectric constant of the B_2 modes of $CdGeP_2$.

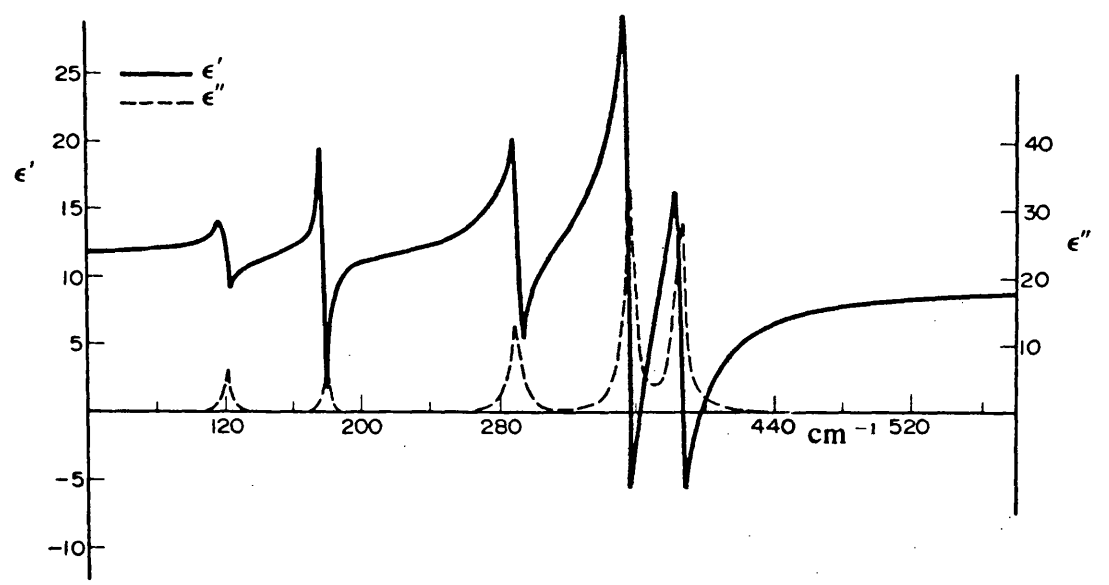

Fig. 5(b). Real and imaginary parts of the dielectric constant of the E modes of $CeGeP_2$.

Figure 4.5

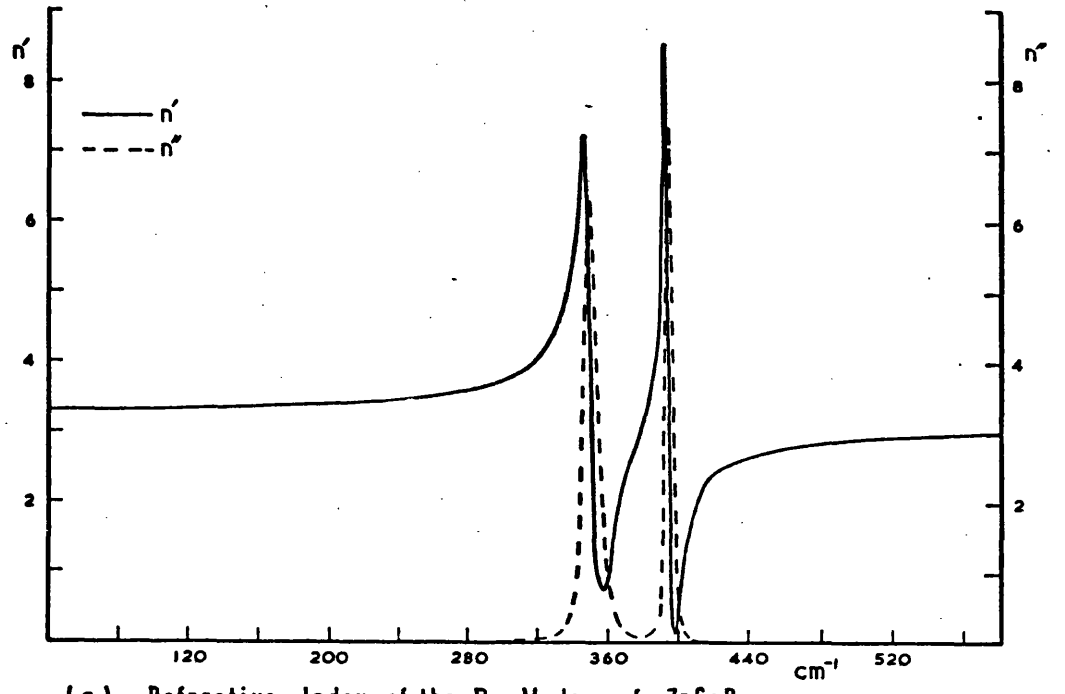

(a) Refractive Index of the B_2 Modes of $ZnGeP_2$

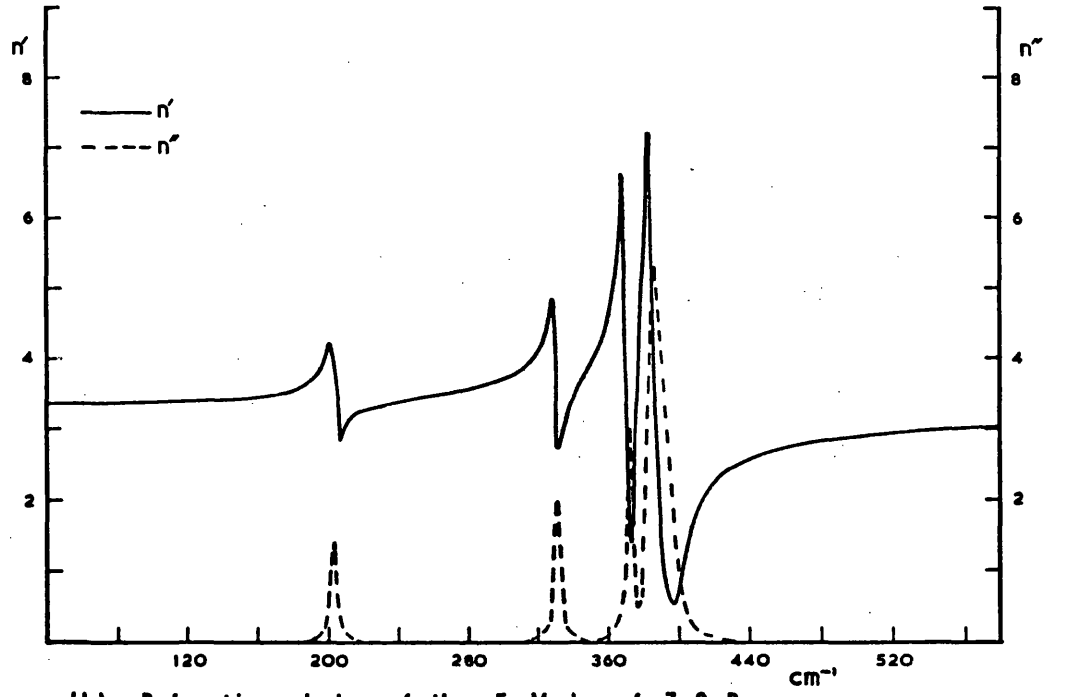

(b) Refractive Index of the E Modes of $ZnGeP_2$

Figure 4.6

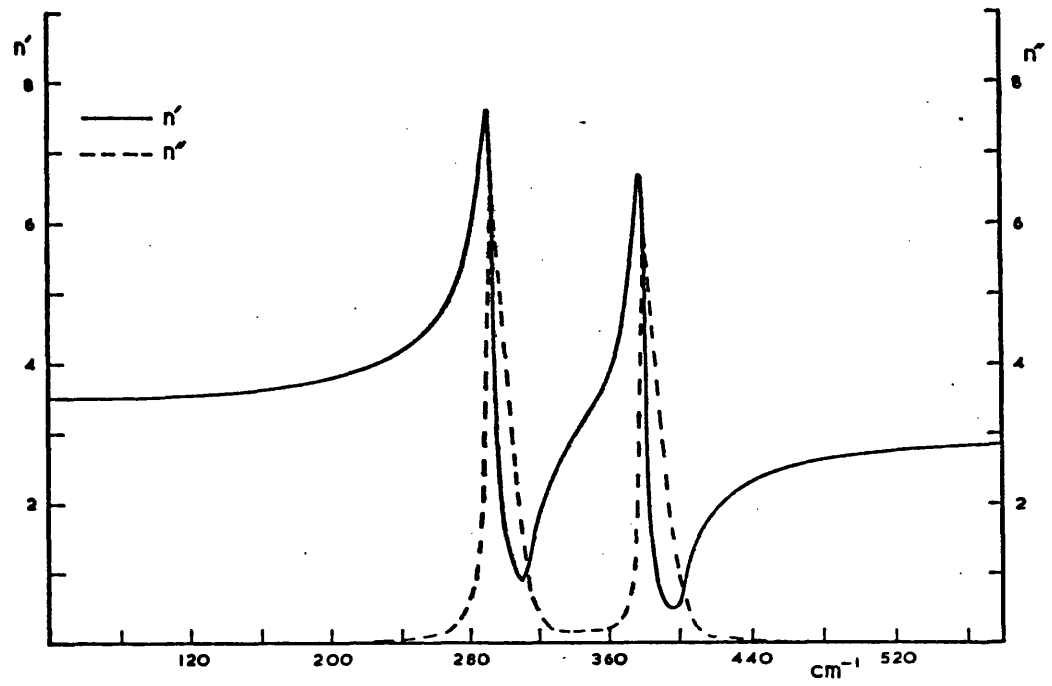

(a) Refractive Index of the B_2 Modes of $CdGeP_2$

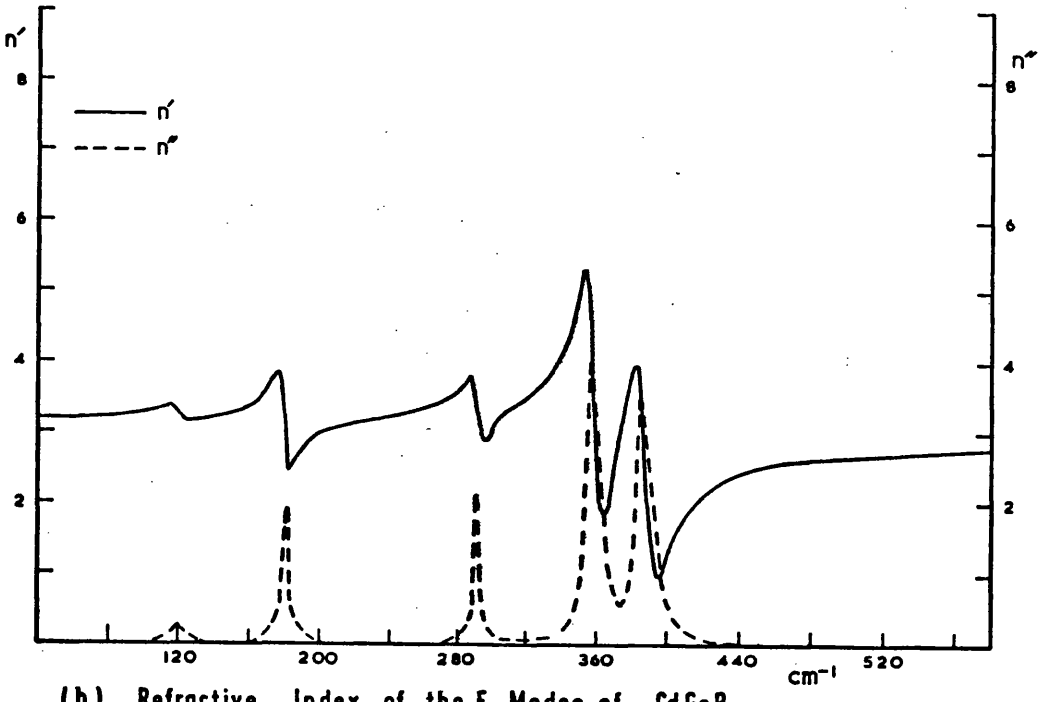

(b) Refractive Index of the E Modes of $CdGeP_2$

Figure 4.7

Table 4.1 Results of analysis for $ZnGeP_2$

	Dispersion analysis				Kram-Krön.		Ref (119)	
	TO cm^{-1}	LO cm^{-1}	S cm^{-2}	γ cm^{-1}	TO cm^{-1}	LO cm^{-1}	TO cm^{-1}	LO cm^{-1}
B_2 modes								
Γ_{15}	392	401	4.76×10^4	1.16	392	402	397	414
W_2	348	360	1.07×10^4	3.95	348	359	342	364
	$\varepsilon_\infty = 9.94$							
E modes								
Γ_{15}	385	402	1.01×10^5	4.26	384	402	387	406
W_4	370	375	4.16×10^4	1.08	370	376	365	376
X_5	330	332	2.11×10^4	3.68	329	335	326	332
W_3	202	204	8.3×10^3	3.31	201	206	205	208
							142	143
	$\varepsilon_\infty = 9.70$							

Table 4.2 Results of analysis for $CdGeP_2$

	Dispersion analysis				Kram-Krön.		Ref (118)	
	TO cm^{-1}	LO cm^{-1}	S cm^{-2}	cm^{-1}	TO cm^{-1}	LO cm^{-1}	TO cm^{-1}	LO cm^{-1}
B_2 modes								
Γ_{15}	387	401	7.87×10^4	4.38	388	399	381	400
W_2	295	317	1.54×10^5	10.25	295	315	294	312
	$\varepsilon_\infty = 10.23$							
E modes								
Γ_{15}	385	397	7.05×10^4	9.06	385	396	381	400
W_4	356	363	8.95×10^4	7.90	356	362	351	360
X_5	289	293	2.63×10^4	8.20	288	295	287	-
W_3	179	181	6.45×10^4	1.80	177	182	177	-
W_4	122	124	3.81×10^4	7.57	121	127	-	-
	$\varepsilon_\infty = 10.17$							

absorption coefficient, α, or the extinction coefficient, n''. Figures 4.4 and 4.5 thus give ω_{TO}, which are tabulated for the various modes.

Longitudinal displacements will be associated with a longitudinal field, $\underline{E} \| \underline{k}$. For a crystal having no net charge, the Maxwell relation, $\nabla.\underline{D} = 0$ gives,

$$\varepsilon(\omega).\ \underline{k}.\underline{E} = 0$$

This equation can only be satisfied by a non-zero, $E_{||}$, if there are frequencies for which $\varepsilon(\omega) = 0$. Figures 4.4 and 4.5 giving the real and imaginary parts of the dielectric constants show that $\varepsilon'(\omega)$ does not reach zero for all modes. In these cases, the minimum value has been chosen.

The results of the Kramers-Krönig analysis are given in Tables 4.1 and 4.2 for comparison with the dispersion analysis. A computer programme was written to calculate the phase change from the measured reflectivity by the integration in equation 4.21. The reflectivity was extrapolated to zero frequency by a horizontal line in each case and the high frequency end was produced to the value of the reflectivity calculated from Boyd's measurements (55, 56) of the refractive index, figures 4.3(a) and (b), assuming no strong absorption in the unmeasured range. (Two phonon absorption is normally small). The dispersions of the optical constants were very similar to the curves presented for the classical dispersion analysis, and the frequencies of the TO and LO modes obtained from the two analyses were within the resolution of $4cm^{-1}$ for the experiments.

To complete Tables 4.1 and 4.2, recent results of Markov et al for $ZnGeP_2$ (119) and $CdGeP_2$ (118) are also listed. General agreement is obtained between these results and the present ones

described here. One extra E mode was observed at low frequency in $ZnGeP_2$ which is confirmed by the Raman measurements of Chapter 5. The largest difference is in the frequency obtained for the B_2, $\Gamma_{15}(LO)$ mode. Since there is close agreement between the values obtained from dispersion and Kramers-Krönig analyses in this work, the discrepancy may lie in the experimental results rather than the analysis. Markov used polished surfaces, with E||c axis, whereas the present work used as grown (112) faces. Thus, with a (112) face, there can be mixing between the B_2 and E modes with the effect that the measured $\Gamma_{15}(LO)$ mode will be shifted towards the $\Gamma_{15}(LO)$ mode with E irreducible representation. No splitting of the Γ_{15} modes in the two representations was observed at all by Markov in $CdGeP_2$. The difference between $ZnGeP_2$ and $CdGeP_2$ here is surprising since one would expect the very large tetragonal compression of $CdGeP_2$ to contribute to a splitting of these modes.

4.4.2 Lyddane - Sachs - Teller relation

Zone centre longitudinal optical vibrations have higher frequencies than the transverse vibrations of the same mode, due to the long range Coulomb forces associated with polar modes. Lyddane, Sachs and Teller (134) showed from the macroscopic theory of optical vibrations (93) that the frequencies are related by,

$$\frac{\varepsilon(o)}{\varepsilon_\infty} = \left(\frac{\omega_L}{\omega_T}\right)^2 \qquad 4.23$$

for the case of cubic crystals with two atoms per unit cell. This relation is independent of any model used to describe the crystal and depends only on the electrostatic, adiabatic and harmonic approximations, for phonons of wavelength long compared to the unit cell but small compared to the crystal dimensions. Merten (135, 136) modified equation 4.23 for uniaxial crystals with two atoms

per unit cell and Cochran and Cowley (137) derived a general expression for any crystal,

$$\frac{\varepsilon(o)}{\varepsilon_\infty} = \prod_j \left(\frac{\omega_{Lj}}{\omega_{Tj}}\right)^2 \qquad 4.24$$

where the product is over all modes of vibration of a given polarisation.

Applying equation 4.24 to the results obtained in section 4.4.1 gives the static dielectric constants,

$ZnGeP_2$:	B_2 modes	$\frac{\varepsilon(0,B_2)}{\varepsilon_\infty}$	= 1.12	$\varepsilon(0) = 11.13$
	E modes	$\frac{\varepsilon(0,E)}{\varepsilon_\infty}$	= 1.16	$\varepsilon(0) = 11.21$
$CdGeP_2$:	B_2 modes	$\frac{\varepsilon(0,B_2)}{\varepsilon_\infty}$	= 1.24	$\varepsilon(0) = 12.69$
	E modes	$\frac{\varepsilon(0,E)}{\varepsilon_\infty}$	= 1.20	$\varepsilon(0) = 12.20$

4.4.3 Effective charge

The degree of polar character, or ionicity, of a partially ionic crystal has been defined in several ways depending on the application of the concept to different measurements. The usual approach taken for infrared measurements is to calculate an effective charge for the ions. Several definitions for this also exist. The problem lies in the fact that the interaction of electromagnetic radiation lies not only with the charge associated with the ions, but also with the polarisation produced by the movement of the electron shells relative to the positive ion cores. For a diatomic compound, the polarisation is given by,

$$P_x = \frac{Z.e\ (x_A - x_B)}{V} + \frac{\alpha\ \varepsilon_o .\ E_x\ \ell oc}{V}$$

where Z.e is the excess charge on the anion, and α is the summed polarisability of both ions. V is the volume of the primitive unit cell.

The local field can be expressed by the Lorentz field, $\underline{E_{loc}} = \underline{E} + \frac{\underline{P}}{3\varepsilon_0}$ for an isotropic medium, and the polarisability by the Clausius Mosotti formula,

$$\frac{\alpha}{3V} = \frac{\varepsilon_\infty - 1}{\varepsilon_\infty + 2}$$

Born and Huang (93) defined an effective ionic charge for transverse fields by solving the phenomenological macroscopic equations for dispersion, giving the polarisation in terms of a displacement times the effective charge term,

$$\frac{e_B^*}{e} = \frac{2\pi c}{e} \cdot \sqrt{\varepsilon_0 . S \cdot \frac{m}{N}} \qquad 4.25$$

where m is the reduced mass and N is the number of dipoles per cubic metre.

Similarly, for a long wavelength longitudinal mode, $\underline{D} = \varepsilon_0 . \underline{E_{loc}} + \underline{P} = 0$, so that, the Callen charge is defined for longitudinal fields by,

$$\frac{e_c^*}{e} = \frac{2\pi c}{\varepsilon_\infty . e} \cdot \sqrt{\varepsilon_0 . S \cdot \frac{m}{N}} \qquad 4.26$$

Szigetti (134, 135) derived another well used expression for effective charge by an atomic treatment of dielectric dispersion,

$$\frac{e_s^*}{e} = \frac{3}{e.(\varepsilon_\infty + 2)} \left[\frac{4\pi^2 . c^2 . \varepsilon_0 . m . S}{N} \right]^{\frac{1}{2}} \qquad 4.27$$

If it is assumed that the anisotropy of the local field is not too large in the chalcopyrite structure, then equation 4.27 can be solved for the high frequency Γ_{15} polar modes for II-IV-V_2 compounds since this is the anions moving in antiphase with the cations as in the III-V zinc blende zone centre mode. The effective charge will then be due to the average contribution of the two cations if the reduced mass is calculated by taking the arithmetic mean of the cation masses. The results are tabulated in Table 4.3 and

compared with the values for the nearest III-V analogues, GaP and InP. The values for the III-V's are much higher due to the larger LO-TO splitting in these materials.

It has been pointed out by Cochran that the values of Szigetti charge can be misleading. For instance, the value for KBr is 0.73 although from other experimental evidence it is expected to be almost 1.0 and thus completely ionic. Similarly, the value of GaP may be too high since it actually shows very strong covalent character, even to the extent that the gallium atom in fact has a net negative charge.

The discrepancy comes from the fact that the polarisability changes as the displacement of the ions distort the electron shells. A large part of the effective charge comes from this contribution. In the shell model this is taken account of by defining a new effective charge with this contribution added. A physical model is required for this distortion before the effective charges can be fully interpreted. Hidaka (141) has recently attempted to interpret the contribution due to the distortion in terms of only second nearest neighbour electron interactions of the cations for tetrahedrally coordinated materials. Nevertheless, the lower effective charges obtained for chalcopyrite materials may be mainly due to the redistribution of the charge between the atoms. Section 1.2 discussed how charge is expected to be transferred from the Zn-P bond to the more covalent Ge-P bond and so the dipole associated with a displacement of germanium and phosphorus atoms may be small compared to that due to a displacement of zinc and phosphorus atoms.

Table 4.3 Effective charges

	e^*_B/e	e^*_c/e	e^*_s/e	Ionicity (Levine, 25)
GaP(140)	2.0	0.24	0.58	0.328
InP(140)	2.5	0.26	0.66	0.421
$ZnGeP_2$: B_2	0.92	0.092	0.231	Zn-P: 0.442
: E	1.34	0.14	0.334	Ge-P: 0.219
$CdGeP_2$: B_2	1.29	0.13	0.317	Cd-P: 0.532
: E	1.22	0.12	0.301	Ge-P: 0.231

Recently, Levine (25, 28) has extended the ionicity defined for binary compounds by Phillips and Van Vechten (26) to II-IV-V_2 and I-III-VI_2 compounds. His work derives the ionicity empirically from the electronic dielectric constant and bond length. A static dielectric constant had to be derived for each bond by extrapolation from the values of III-V compounds, but the values he obtains can predict the values of non-linear susceptibilities comparable with experimental results (55, 56, 57). The values of ionicity obtained are shown in Table 4.3 for comparison with the calculated effective charges. The ionicity of the IV-V bond is found to be smaller as expected and the average ionicity of the two bonds is comparable with the value for the III-V analogue.

4.4.4 Polariton dispersion

Transverse optic phonons will couple strongly with photons of the same frequency and wavevector. For $\varepsilon \neq 0$, $\underline{k}$, $\underline{E}$ and $\underline{H}$ vectors are mutually orthogonal, and the phase velocity of the wave motion is given by,

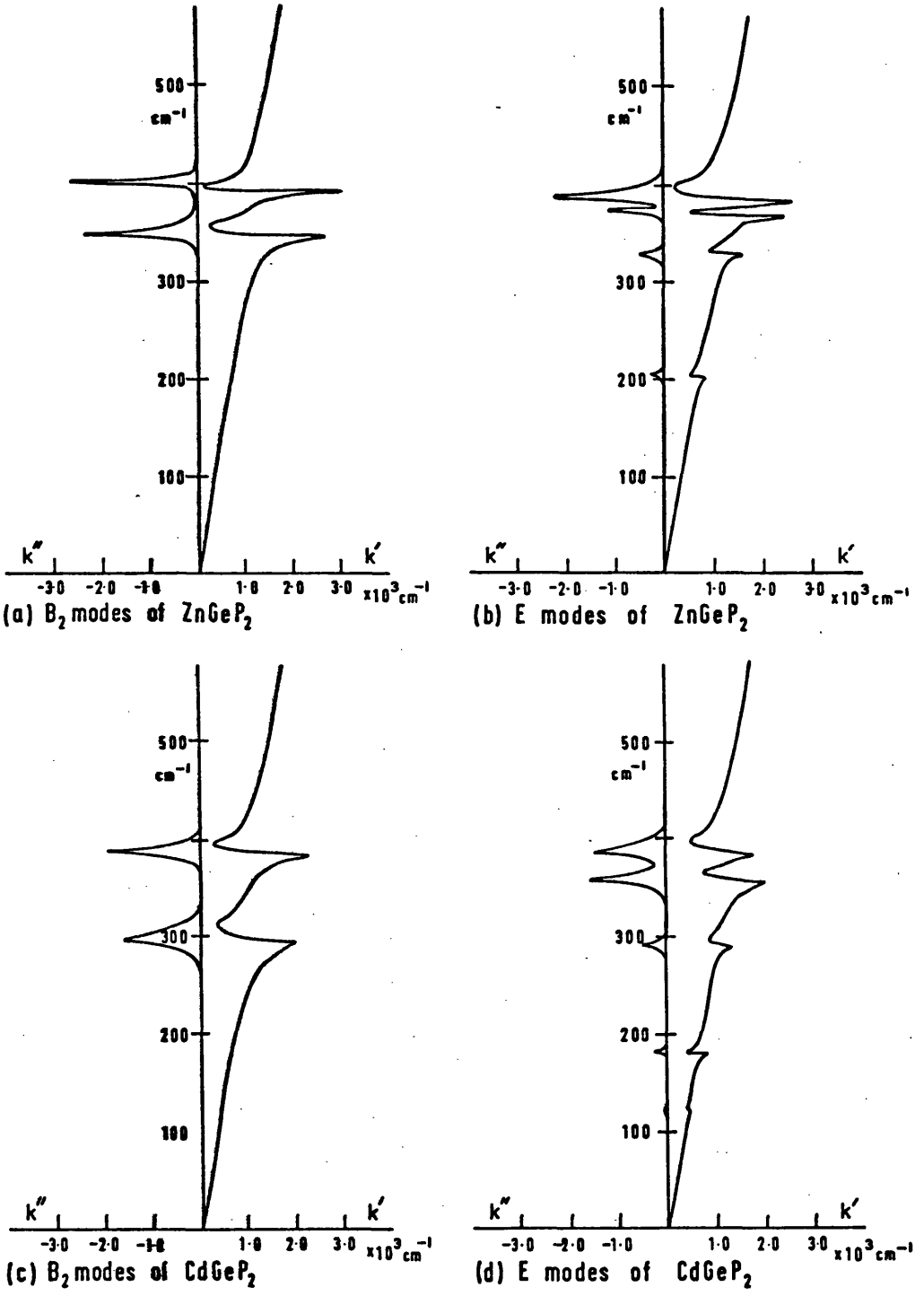
500
cm⁻¹
300
200
100
k″
k′
-3·0 -2·0 -1·0 1·0 2·0 3·0 x10³cm⁻¹
(a) B₂ modes of ZnGeP₂
(b) E modes of ZnGeP₂
(c) B₂ modes of CdGeP₂
(d) E modes of CdGeP₂

Figure 4.8

$$v = \frac{c}{n} = \frac{c.\omega}{k}$$

where c is the velocity of e.m. in vacuum and k is the wavevector in cm^{-1}.

Thus, the dispersion relation can be written,

$$k^2 = \omega^2 . \varepsilon(\omega)$$

$\varepsilon(\omega)$ is given by equation 4.18, and the resulting dispersion curves for B_2 and E modes of $ZnGeP_2$ and $CdGeP_2$ are shown in figure 4.8. A combined state exists which is partly mechanical and partly electromagnetic. Hopfield (142) called this state a polariton. At low frequency, the energy of the system is photon-like, as it is again at high frequency. At intermediate values, the dispersion tends to become horizontal, indicating mechanical, phonon-like character.

Holah (60) has pointed out the possible use of chalcopyrite semiconductors as polariton Raman lasers using their phase matching properties. The generation of tunable infrared radiation by Raman scattering from polaritons has been demonstrated in $LiNbO_3$(61).

4.5 Conclusions

Figure 4.9 groups the results of the infrared analysis for comparison with the experimentally determined GaP frequencies. The frequency distribution can be seen to compare well for GaP and $ZnGeP_2$ indicating that the assumption that the atomic motions of $ZnGeP_2$ will be similar to GaP is valid. The $ZnGeP_2$ and $CdGeP_2$ modes corresponding to the Γ_{15} motions of GaP were chosen to be those with the highest frequency since very similar reflection peaks were observed in both B_2 and E configurations with comparable frequencies and strengths. The heavier cadmium atom does not move this mode to lower energy since the reduced mass of the cations and anions is almost the same for $CdGeP_2$ and $ZnGeP_2$. However, the

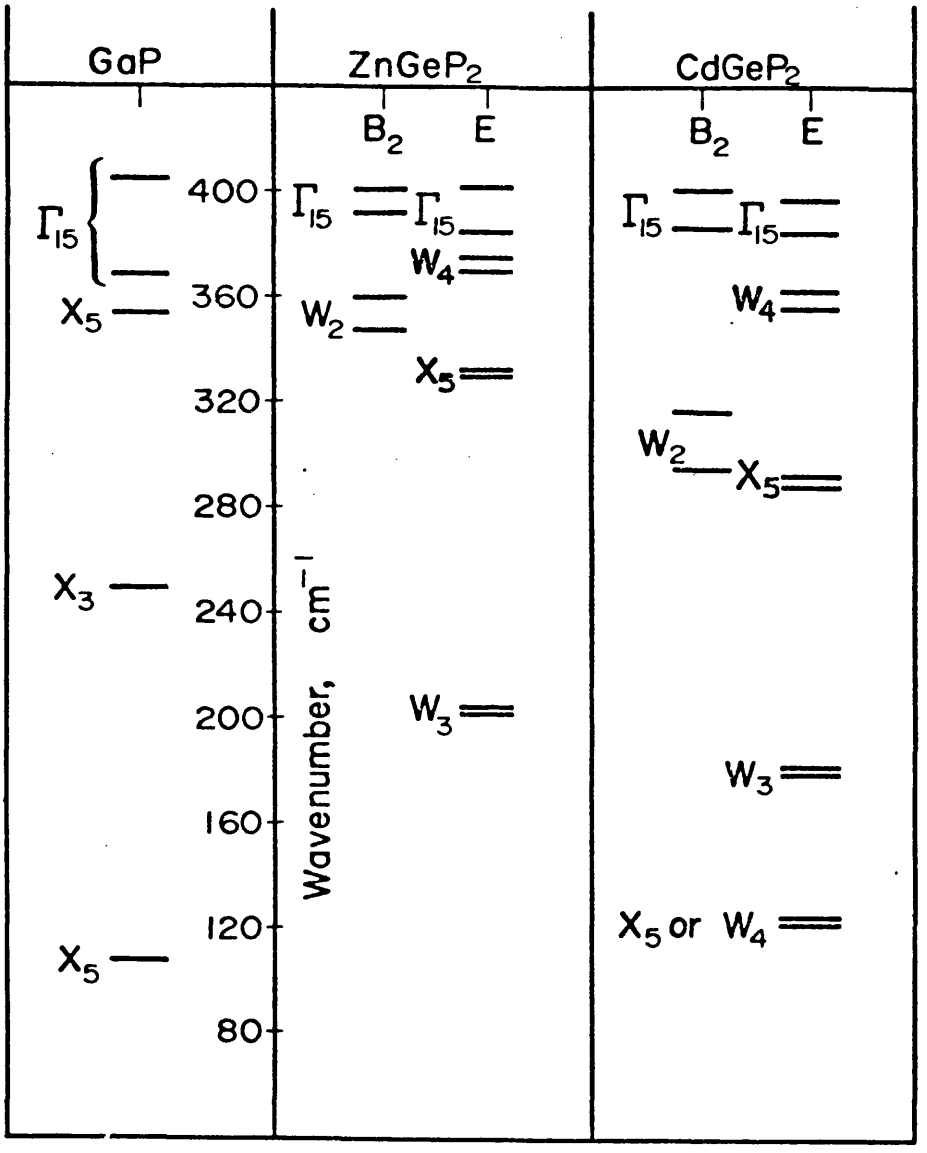

Longitudinal and transverse vibrational mode frequencies of $ZnGeP_2$ and $CdGeP_2$ compared with GaP modes.

Figure 4.9

displacement of the cadmium atom will be much smaller than the zinc, so that in $CdGeP_2$ this mode will be mostly a Ge-P motion. The coulomb splittings are much smaller for the chalcopyrite modes than for the Γ_{15} GaP mode which may at first seem to indicate that the ionicity of the GaP bond is larger. However, the redistribution of charge whereby charge gained by germanium and phosphorus is lost by zinc, as discussed in section 1.2, will also cause this effect. Further, mixing of Γ_{15}, W_4 and X_5 modes of E irreducible representation will also alter the LO-TO splitting of the Γ_{15} (E) mode. The allocation of W_4 and X_5 labels is fairly arbitrary since the mixing of these modes will be large because they are close in energy. In the X_5 symmetry mode, figure 3.5, the dipole moments cancel out within the unit cell so that X_5 is assigned to the weaker of the two modes observed.

Further discussion of the interpretation of the lattice modes will be delayed until section 5.5 when the results of Raman scattering measurements are included.

CHAPTER 5 Raman Scattering

5.1 Introduction

In order to supplement the knowledge gained about the lattice vibrational modes by infrared reflection, Raman scattering measurements were carried out with M. Bettini (104), at the invitation of Professor M. Cardona at the Max Plank Institut für Festkörperforschung Stuttgart, in the Federal Republic of Germany. Raman scattering is inelastic scattering of electromagnetic radiation from the atoms of a material. The frequency of the incident light is much higher than that of the lattice phonons, normally in the optical region. Two scattering processes, involving either creation or annihilation of a phonon can be observed, as shown in figure 5.1,

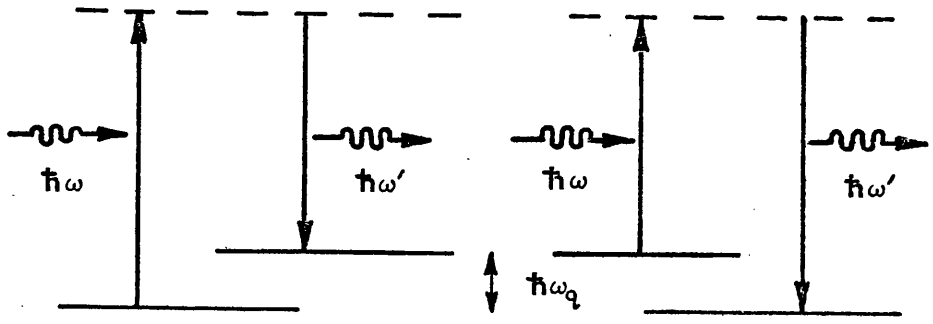

(a) Stokes line
phonon creation
$\hbar\omega > \hbar\omega'$

(b) Anti-Stokes line
phonon annihilation
$\hbar\omega < \hbar\omega'$

Figure 5.1

The qualitative explanation of the process in (a), is that the incident electromagnetic radiation, with energy, $\hbar\omega$, can excite the crystal to a virtual electronic state by interaction with the outer electrons of the ions comprising the solid. The crystal (within 10^{-12} sec) de-excites by emission of a photon of energy $\hbar\omega'$ and simultaneously the creation of a lattice phonon of energy $\hbar\omega_{\underline{q}} = \hbar\omega - \hbar\omega'$. This is Stokes' scattering. The alternative process known as Anti-Stokes scattering, is shown in figure 5.1 (b) in which the crystal is already in an excited vibrational state of energy $\hbar\omega_{\underline{q}}$. Incident light of energy $\hbar\omega$ again creates a virtual electronic state and the crystal returns to its ground state by the annihilation of the phonon and emission of a photon of energy $\hbar\omega'$. In this case, light scattering is to higher frequency with $\hbar\omega_{\underline{q}} = \hbar\omega' - \hbar\omega$.

A study of the frequency shift of the scattered light thus gives directly the frequencies of the lattice phonons. Normally, only one phonon processes are observed, as the scattering cross sections for multiphonon processes are much smaller. Stokes' scattering is in general stronger than anti-Stokes', especially at low temperature when the number of phonons already excited is small. In the first instance, one avoids exciting the crystal to any electronic energy level of the crystal since resonance effects complicate the interpretation of the spectra. Thus, in the study of a semiconductor by Raman scattering, incident light, whose frequency lies in the transparent region below the electronic energy band gap is used, with analysis of the Stokes' scattered light at longer wavelengths. Typically, 10^{-5} of the incident light may be scattered with change of frequency.

The phenomenon was first discovered by Sir C.V. Raman in 1928 (143-145), although it was theoretically predicted by Smekal

in 1923 (146). Many crystalline materials were studied using the discreet lines of a gas discharge lamp as source in the 1930's and 40's, limiting investigation to materials with band gaps above 2eV. The development of the laser in the 1960's as a high power narrow line width visible and infrared source has revived much interest in the effect as a tool for the study of lattice dynamics and chemical analysis. Much work is also being done on second order, resonant and stimulated Raman scattering. Excitations other than phonons, such as electronic states, plasmons and spin waves can be used to obtain a frequency shift.

5.2 Experimental

The crystals used for Raman scattering measurements all had natural (101) faces, but were not thick enough to observe light scattered at right angles to the incident beam. The back scattering configuration shown in figure 5.2 was used with a Krypton laser. The angle of incidence was 30^{o}, so that the angle of refraction inside the crystal was about 10^{o}, assuming a refractive index of 3 (figure 4.3). The crystal, which was mounted on a copper block in a glass cryostat was normal to the light collecting system with a collecting angle of 30^{o}. A cylindrical lens focussed the light to a vertical line on the crystal face. The scattered light could then be focussed to a similar image on the vertical entrance slits of the monochromator, by the large collecting lens. A Jarrel Ash one meter double monochromator was used with entrance, centre and exit slits set to a width of 100μm, corresponding to a resolution of $2cm^{-1}$. The detector was a GaAs - RCA phototube IC-3104-01. A 1000 channel Canberra multichannel analyser was used to store the spectra, which were taken at scanning rates of between 0.1 and $0.25cm^{-1}$ per sec., with each channel open for between one and five seconds. This was

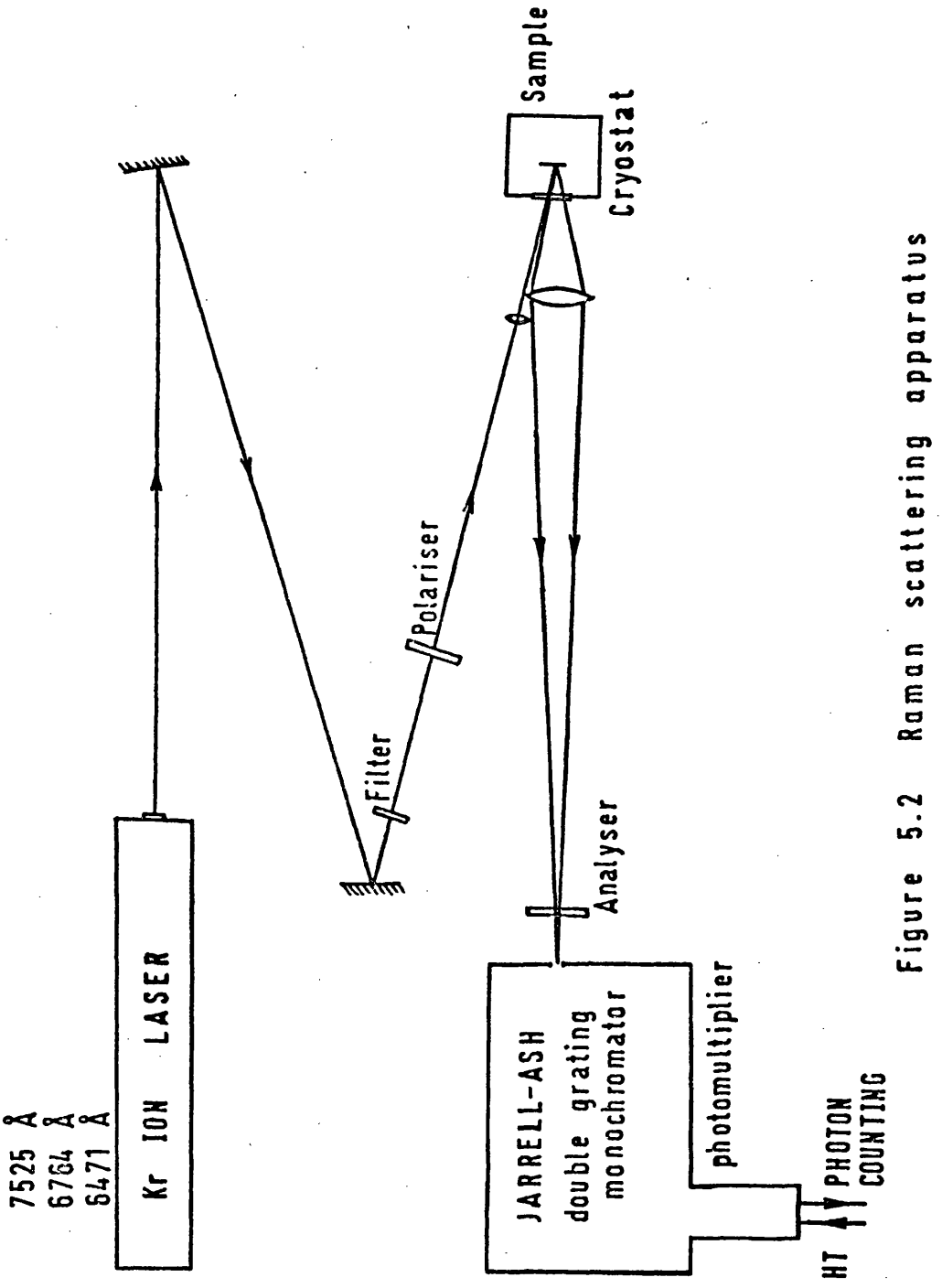

Figure 5.2 Raman scattering apparatus

within the $2cm^{-1}$ resolution of the monochromator.

Using polarised incident light, parallel and perpendicular to the c-axis, and inserting an analyser in the scattered beam in similar configurations, most of the Raman active modes of vibration can be identified, section 5.3.2, when a (101) crystal face is used. Polaroid sheet was used for polariser and analyser. In fact, the c-axis does not lie in the (101) face, but at $\theta = 27^{o}$ to it, figure 5.3. The projection of the c-axis onto the face is at $\phi = 24^{o}$ to the [111] growth direction of the crystal which is defined by the edge between the (101) and (112) faces. The y-axis lies on the (101) face. Thus, with the [111] direction vertical, the light could be polarised along the projection of the c-axis on the face by rotating the polariser axis 24^{o} from the vertical. The sense of this rotation was checked by X-ray Laüé back reflection. The analyser was set similarly.

Due to the relatively low band gaps of $ZnGeP_2$ and $CdGeP_2$ in the visible region, section 6.5.3, a Krypton laser was used, which offered laser frequencies below these gaps, at 647.1nm, 676.4nm and 752.5nm, with powers between 75 and 150mW, which was large enough for Raman scattering. All of these lines were below the absorption edge of $ZnGeP_2$, figure 6.11, at liquid nitrogen temperature, but only the 752.5 nm line was far enough below the steep anisotropic absorption edge of $CdGeP_2$, and then only at liquid nitrogen temperature when the band gap has increased, figure 6.12. This was the only case when the selection rules were well obeyed for $CdGeP_2$, but all spectra were checked with at least two laser frequencies to avoid laser discharge lines being mistaken for Raman scattering. A narrow band pass filter was used with each line. By comparing room and liquid nitrogen temperature spectra, second order Raman scattering was eliminated due to the different temperature dependence of the

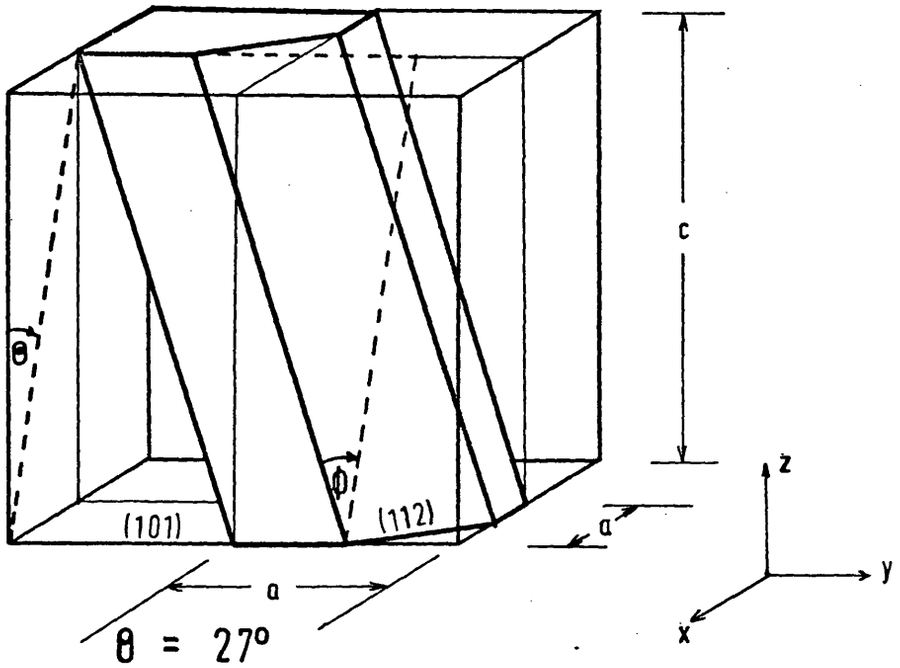

Figure 5.3 (101) face used for Raman scattering

scattered frequencies of the two processes. The line width of first order scattering is reduced at liquid nitrogen temperature, which makes identification of complicated spectra clearer.

The spectra were corrected for the different monochromator response to the scattered light analysed parallel and perpendicular to the c-axis of the crystal. This was calibrated using several emission lines of a Ne lamp which had no preferred polarisation of the emitted light. The laser power was noted at a position after the polariser, before and after each run, and the scattered intensity corrected for differences of power in the different polarisations.

Finally the spectra were checked using a second crystal of each material.

5.3.1 Raman Active Modes

Not all of the modes of vibration of a crystal are necessarily Raman active, and the different active modes will have different polarisation, directional and intensity dependences. Although the process of Raman scattering is understood qualitatively, the theoretical prediction of intensities is still an active field of research. A quantum mechanical description of the intensities was given by Loudon (147) involving third order time dependent perturbation theory. Other models have been used, for example, Born and Bradburn (148) used an expansion technique for the elements of the polarisability tensor while Garrett and Barker (149, 150) applied the shell model to represent the ionic distortion.

Active modes and their selection rules can, however, be predicted from the crystal symmetry and the method has been reviewed by Loudon (106) for all 32 point groups. Light of optical frequency interacts with the crystal only through the electronic polarisability of the ions. The ions themselves are too heavy to respond at this

frequency, but the value of the polarisability is dependent on the displacement of the ions from their equilibrium position due to the distortion of the outer electron shells by the nearest neighbours. The polarisability is given by the summation,

$$\alpha_{\rho\sigma} = \alpha_{\rho\sigma}^{(o)} + \sum_{\mu} \alpha_{\rho\sigma,\mu} r_{\mu} + \ldots$$

$$\alpha_{\rho\sigma,\mu} = \left(\frac{\partial \alpha_{\rho\sigma}}{\partial r_{\mu}} \right)_{r=0} \qquad 5.1$$

where ρ and σ take the values, x, y, z and r_{μ} is the relative displacement of the ions in mode μ.

The polarisability will thus vary periodically with the frequency of the normal modes of vibration. Simplifying the tensor equation 5.1 and ignoring terms after the second, for a single vibrational mode, μ,

$$\alpha = \alpha_o + \Delta\alpha_o . \cos \omega_{\mu} . t$$

The induced dipole moment, due to the incident radiation of frequency ω is,

$$P = \alpha . E_M . \cos \omega . t$$

$$= \alpha_o . E_M . \cos \omega t + \frac{\Delta\alpha_o}{2} . \left\{ \cos(\omega+\omega_{\mu})t + \cos(\omega-\omega_{\mu})t \right\} + \ldots \qquad 5.2$$

The first term gives rise to Rayleigh scattering with no frequency shift, while the second term causes Stoke's and anti-Stoke's Raman scattering. Higher order terms in equation 5.2 give rise to multiphonon scattering.

As shown in equation 5.1, the polarisability is a tensor quantity whose symmetry is given by the crystal structure. It can be shown that the components, $\alpha_{xx}, \alpha_{xy}, \ldots, \alpha_{zz}$ have the same transformation properties as the quadratic functions, $x^2, xy, \ldots, z^2$ (151). The scattered light is produced by re-radiation of energy

by the oscillating dipole moment, $\underline{M}$,

$$\underline{M}_\rho = \sum_\sigma \alpha_{\rho\sigma} \cdot \underline{E}_\sigma \qquad 5.3$$

the scattered intensity being proportional to $|\underline{M}|^2$ and inversely proportional to the fourth power of the wavelength, as for Rayleigh scattering. The character table for $\bar{4}2m$ given in section 3.3.1 shows the quadratic symmetry of the irreducible representations, thus A_1, B_1, B_2 and E modes can be Raman active.

Raman activity is normally complementary to infrared activity. The optic mode at $\underline{q} = 0$ in the diamond lattice has even parity, that is, it is invariant under inversion about a point midway between the atoms. It is thus Raman active, but not infrared active, whereas the zone centre optic mode of sodium chloride is infrared active but not Raman active because the centre of inversion is on the atom site, and so the phonon has odd parity. In piezoelectric crystals which lack a centre of inversion, (such as chalcopyrite), some modes can be both infrared and Raman active. In our case B_2 and E modes are in this category and Raman scattering can be obtained from both longitudinal and transverse modes provided the wavevector is conserved.

5.3.2 Selection rules

The selection rules for point group $\bar{4}2m$ were calculated from the Raman tensors listed by Loudon (126) and reproduced in Table 5.1.

Table 5.1 Raman tensors for $\bar{4}2m$.

$$A_1 : \begin{bmatrix} a & & \\ & a & \\ & & b \end{bmatrix}$$

$$B_1 : \begin{bmatrix} c & & \\ & -c & \\ & & \end{bmatrix} \quad ; \quad B_2(z) : \begin{bmatrix} & d & \\ d & & \\ & & \end{bmatrix}$$

$$E(y) : \begin{bmatrix} & & e \\ & & \\ e & & \end{bmatrix} \quad ; \quad E(x) : \begin{bmatrix} & & \\ & & e \\ & e & \end{bmatrix}$$

The scattering efficiency for a mode of one of the irreducible representations is given by,

$$S = A \cdot \sum_{\rho,\sigma} \left[e_i^{\sigma} \cdot R_{\sigma\rho} \cdot e_s^{\rho} \right]^2 \qquad 5.4$$

where A is a constant of proportionality, $R_{\sigma\rho}$ is the Raman coefficient of the representation and e_i^{σ} and e_i^{ρ} are components of the unit vectors of polarisation of the e.m. radiation along the principle axes, σ and ρ = x, y, z.

For a (101) face, figure 5.3, light polarised along the projection of the c-axis on the face gives $\underline{e}_{||} = \left[\sin 27^{\circ}, 0, \cos 27^{\circ}\right]$. Light polarised along the y-direction gives $\underline{e}_{\perp} = \left[0, 1, 0\right]$. Table 5.2 gives the resulting selection rules for the backscattering configuration, assuming incident and scattered light to be normal to the face. In the table, || and $\perp$ are defined for the above polarisation vectors, $\underline{e}$, and indicate incident and scattered polarisations respectively.

Table 5.2 Selection rules for polarisations defined in text

Irrep.	$\perp$ $\perp$	|| ||	|| $\perp$
A_1	a^2	$(0.2a + 0.8b)^2$	-
B_1	c^2	$0.04.\ c^2$	-
B_2 (TO)	-	-	$0.2\ d^2$
E (TO)	-	$0.64\ e^2$	-
E (LO)	-	-	$0.8\ e^2$

Since the Raman tensors are symmetric, the || $\perp$ polarisation gives the same scattering intensities as $\perp$ ||. For conservation of wavevector, the direction of propagation of the created phonon can only be parallel to the incident light in the backscattering configuration, and thus corresponds to the direction, $\left[\sin\theta, 0, \cos\theta\right]$ relative to the crystal axes. Table 5.3 shows the polarisation of the B_2 and E phonons for different directions of propagation.

Table 5.3 Phonon propagation and polarisation directions

		Phonon polarisation		
		E(x)	E(y)	B_2 (z)
Phonon	x	LO $\perp$	TO $\perp$	TO $\parallel$
propagation	y	TO $\perp$	LO $\perp$	TO $\parallel$
direction	z	TO $\perp$	TO $\perp$	LO $\parallel$

Note that in Table 5.3., $\perp$ and $\parallel$ denote phonon polarisations exactly parallel and perpendicular to the c-axis. Thus, for phonon propagation in a direction near to the x-axis, the top row shows that the longitudinal B_2 mode will be only very weak. In addition, equation 5.4 is solved separately for E(y) and E(x) from Table 5.1. E(y) gives the scattering coefficient 0.64 e^2 for $\parallel$ $\parallel$ configuration and E(x) gives 0.8 e^2 for $\parallel$ $\perp$, (other configurations being zero). By comparison with the top row of Table 5.3, it can be seen that these configurations give TO and LO modes respectively. The selection rules of Table 5.2 do not distinguish between B_2(TO) and E(LO) modes.

5.4 Results

Best agreement with the selection rules of Table 5.2 were obtained for $ZnGeP_2$ using the 647.1 nm Krypton laser line and with the 752.5nm line for $CdGeP_2$ at liquid nitrogen temperature. The spectra are shown in figures 5.4 and 5.5 respectively, and have been corrected for monochromator polarisation response and laser power.

The spectra were sharper at liquid nitrogen temperature than at room temperature, which helps to distinguish the closely grouped set of modes in the 300 to 400 cm^{-1} region, but no frequency shifts of the modes were observed with temperature. Faint second order

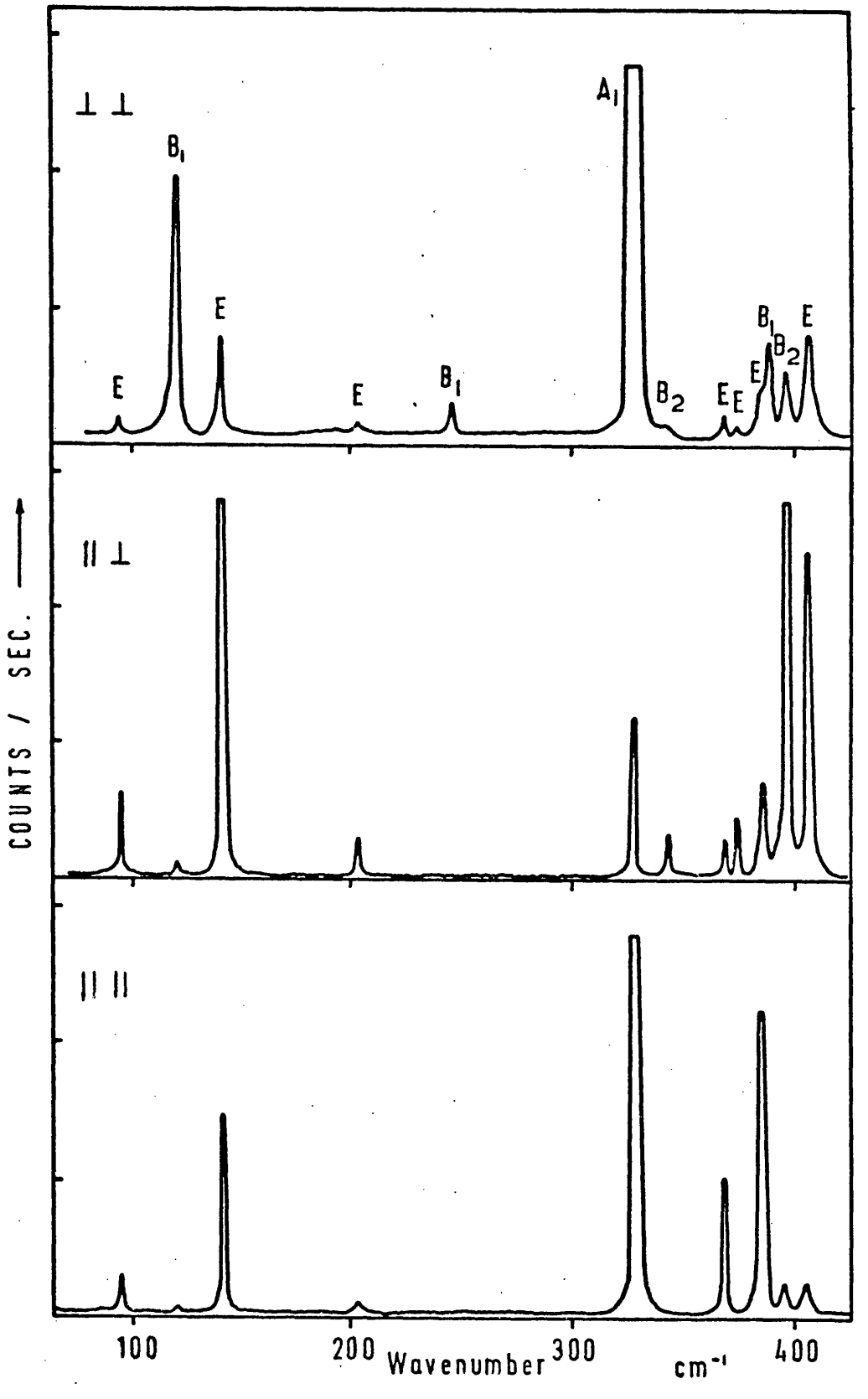

Figure 5.4 Raman spectra of $ZnGeP_2$
Krypton laser line 647·1 nm, T = 78 K

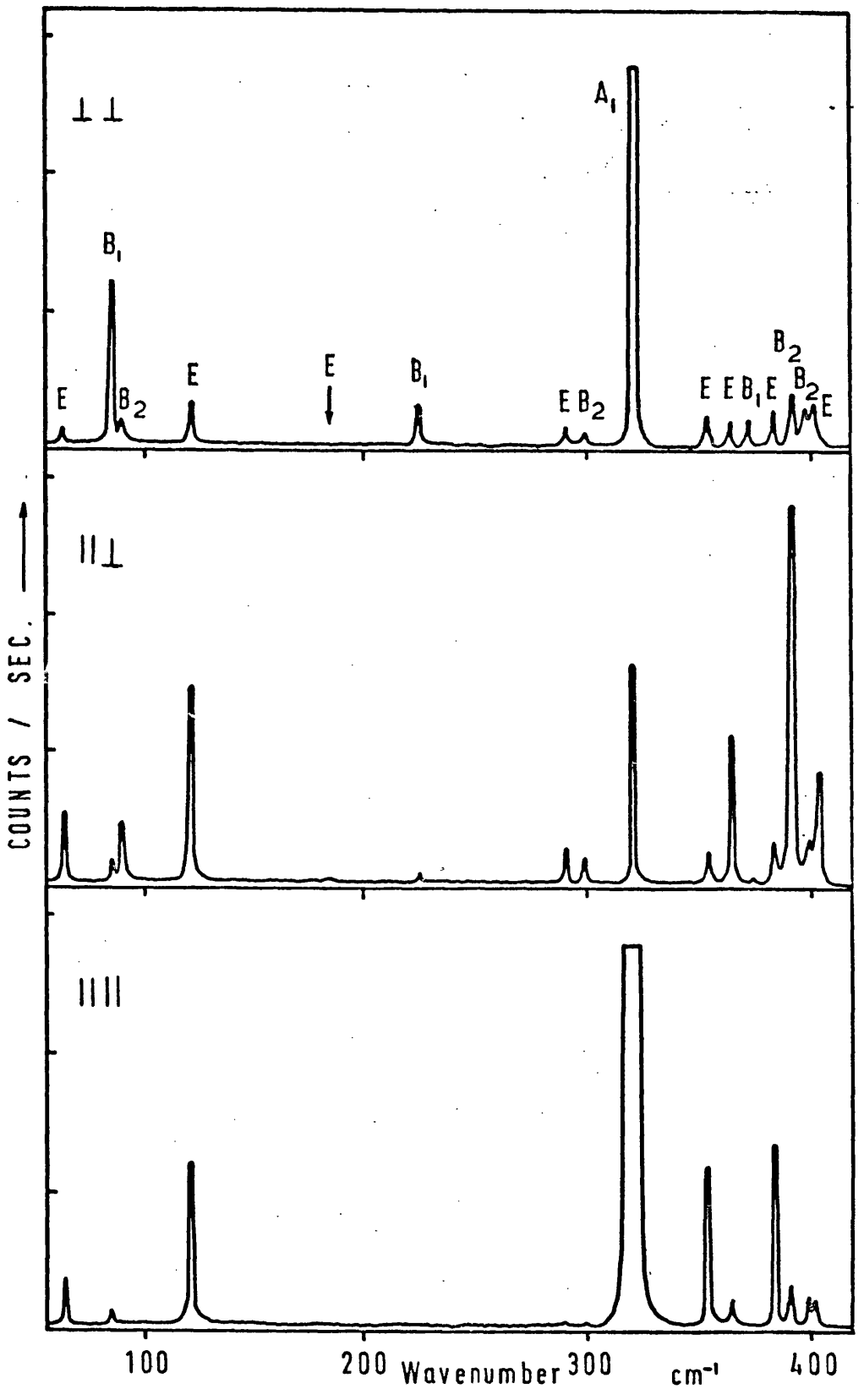

Figure 5.5 Raman spectra of $CdGeP_2$

Krypton laser line 752·5 nm, T = 78 K

structures appearing between 100 and 200 cm^{-1} could be distinguished at liquid nitrogen temperature. As well as the spectra shown, the $\perp$ || configuration was also used as a check on the ||$\perp$ configuration as it has the same scattering intensity coefficients. The peaks are labelled with the most likely assignments by comparison with the selection rules of Table 5.2. In general, the selection rules were not obeyed perfectly, but well enough to assign all the peaks. The peak at 398 cm^{-1} in $CdGeP_2$ had to be associated with the forbidden $B_2(LO)$ mode. As can be observed for the $\perp$ $\perp$ configuration, for instance, B_2 and E modes have considerable strength although they are forbidden. The reason for the deviations from the selection rules come from a combination of four main sources,

(i) crystal quality, i.e. small impurity inclusions, cracks and grain boundaries cause scattering of the incident light.

(ii) the off axis angle of incidence and the aperture of the scattered light collecting lens will give components from other polarisations.

(iii) the absorption coefficient, $\alpha_{||}$ is greater than $\alpha_{\perp}$ below the absorption edge, figures 6.11 and 6.12, so that $\perp$ $\perp$ intensities will be increased and the || || intensities decreased relative to the ||$\perp$ configuration.

(iv) thin platelets of the samples were used ($\sim$ 0.5 mm thick) so that reflections were obtained from the uneven rear surfaces.

The effect of (i) is difficult to determine. Appendix B gives the selection rules, calculated for an angle of incidence of 30°, and the results show that the deviation from Table 5.2 should not be more than 10%, so that the effect of (ii) should be small. The effect of (iii) could be observed experimentally. In the case of $ZnGeP_2$, it was noticed that the selection rules were more closely obeyed for laser frequencies nearer the band gap. This

was interpreted as being due to the smaller penetration depth of the laser light into the material as the absorption increased, cutting down the amount of light reflected from the rear surface of the crystal. However, as the band gap is approached, the effect of (iii) increases because the scattering volume is no longer determined by the focus of the lens but by the absorption coefficient. In $ZnGeP_2$ the absorption edge is dominated by an indirect transition, section 6.2 and the strongly anisotropic Eo transitions are well above this, so that the difference between $\alpha_{||}$ and $\alpha_{\perp}$ is not large, figure 6.11. The laser line at 647.1 nm, close to the absorption edge gave the best agreement. On the other hand, $CdGeP_2$ has a direct gap at 1.7 eV at room temperature so that the longest wavelength available at 752.5 nm was in the region of large dichroism with $\alpha_{||} >> \alpha_{\perp}$. At liquid nitrogen temperature, this difference was reduced due to the shift of the band gap to higher energy so that 752.5 nm (= 1.648eV) is just below the band gap, figure 6.12.

By using incident light energies near to the band gap, one also has to consider changes in relative intensities due to the different resonance behaviour of the modes. In forbidden configurations, strong intensities may occur due to the Fröhlich or surface field induced interaction (51). An indication of this may be the strong intensity of the A_1 mode of $CdGeP_2$ for the $||$ $||$ configuration. The A_1 mode resonates in the $||$ $||$ configuration with the $\Gamma_7 - \Gamma_6$ electronic transition and in the $\perp$ $\perp$ configuration with the $\Gamma_6 - \Gamma_6$ transition, figure 6.2. The A_1 mode was also the strongest observed Raman mode in the direct gap I-III-VI_2 chalcopyrite materials, $AgGaS_2$, $AgGaSe_2$ and $CuGaS_2$, investigated by Van der Ziel et al (128), for laser excitation frequencies just below the band gap. By

Table 5.4 Relative intensities of the Raman lines of $ZnGeP_2$

Krypton laser line 647.1nm, T = 78K

Mode (cm^{-1})	Relative Intensities $\perp\perp$	$\parallel\parallel$	$\parallel\perp$	i.r.	Symmetry
94	3.0	7.0	15.0		E(T+L)
120	45.5	1.0	2.5		B_1
141	17.5	37.0	79.0		E(T+L)
203	2.0	2.0	6.5	202,204	E(T+L)
247	5.0	-	-		B_1
328	252.0	152.0	29.5		A_1
343	1.5	-	7.0	348	B_{2T}
369	3.5	24.5	7.0	370	E_T
375	1.5	-	10.5	375	E_L
386	8.5	56.0	17.0	385	E_T
389	17.0	-	-		B_1
396	10.0	5.5	156.0	392	B_{2T}
406	18.0	5.5	60.0	402	E_L

Table 5.5 Relative intensities of the Raman lines of $CdGeP_2$

Krypton laser line 752.5nm, T = 78K

Mode (cm^{-1})	Relative Intensities $\perp\perp$	$\parallel\parallel$	$\parallel\perp$	i.r.	Symmetry
63	2.5	7.5	11.5		E(T+L)
85	29.5	2.5	3.5		B_1
88	5.0	-	10.0		B_2(T+L)
121	8.0	19.5	33.0	122,124	E(T+L)
183	-	-	-	179,181	E(T+L)
225	6.5	-	1.0		B_1
291	3.0	0.5	6.0	289,293	E(T+L)
299	2.0	0.5	4.0	295	B_{2T}
321	135.0	181.0	37.0		A_1
354	5.5	26.0	5.5	356	E_T
364	4.5	4.0	25.5	363	E_L
373	5.0	-	1.0		B_1
383	6.5	30.5	7.0	385	E_T
391	10.0	7.0	66.0	387	B_{2T}
398	6.5	5.0	7.0	401	B_{2L}
402	7.5	4.0	18.5	397	E_L

studying the relative intensity of the mode in the $x(zz)\bar{x}$ configuration for different excitation frequencies, they found that the resonant behaviour was strong below the band gap and continued to $\sim$ 0.7eV above the gaps of $AgGaS_2$ and $AgGaSe_2$ where it fell rapidly.

The frequencies and relative scattering intensities from figure 5.4 are given in Table 5.4 for $ZnGeP_2$ and those from figure 5.5 for $CdGeP_2$ are given in Table 5.5. The number of counts per second have been reduced by a factor of 100 from the experimentally determined values. The Raman results are also compared with the B_2 and E modes determined from the results of infrared reflectivity in Chapter 4, and the final assignment of the symmetry of the modes is given. The $CdGeP_2$ E mode observed in i.r. at 179, 181 cm^{-1} was not observed in the Raman spectra shown in figure 5.5. With a slow scan over this region, a weak peak was observed at 183cm^{-1} and tentatively associated with the missing E mode.

5.5 Interpretation

The observed Raman scattering frequencies of $ZnGeP_2$ and $CdGeP_2$ are presented in figure 5.6 for comparison with GaP phonon energies at Γ and X. This can be compared with figure 4.9 for the infrared results.

In $CdGeP_2$, all of the predicted and allowed Raman active modes were observed. The infrared value of the high frequency $B_2(W_2)$ longitudinal mode is added to figure 5.6 for completeness. Good agreement is obtained between the frequencies determined from infrared and Raman for B_2 and E modes.

In $ZnGeP_2$, two predicted Raman active modes escaped observation. A missing low frequency B_2 mode, corresponding to the zone boundary W_2 mode of GaP may be unresolved in the strong scattering from the B_1 mode at 120cm^{-1}. Both these modes may be derived from W_2 of GaP,

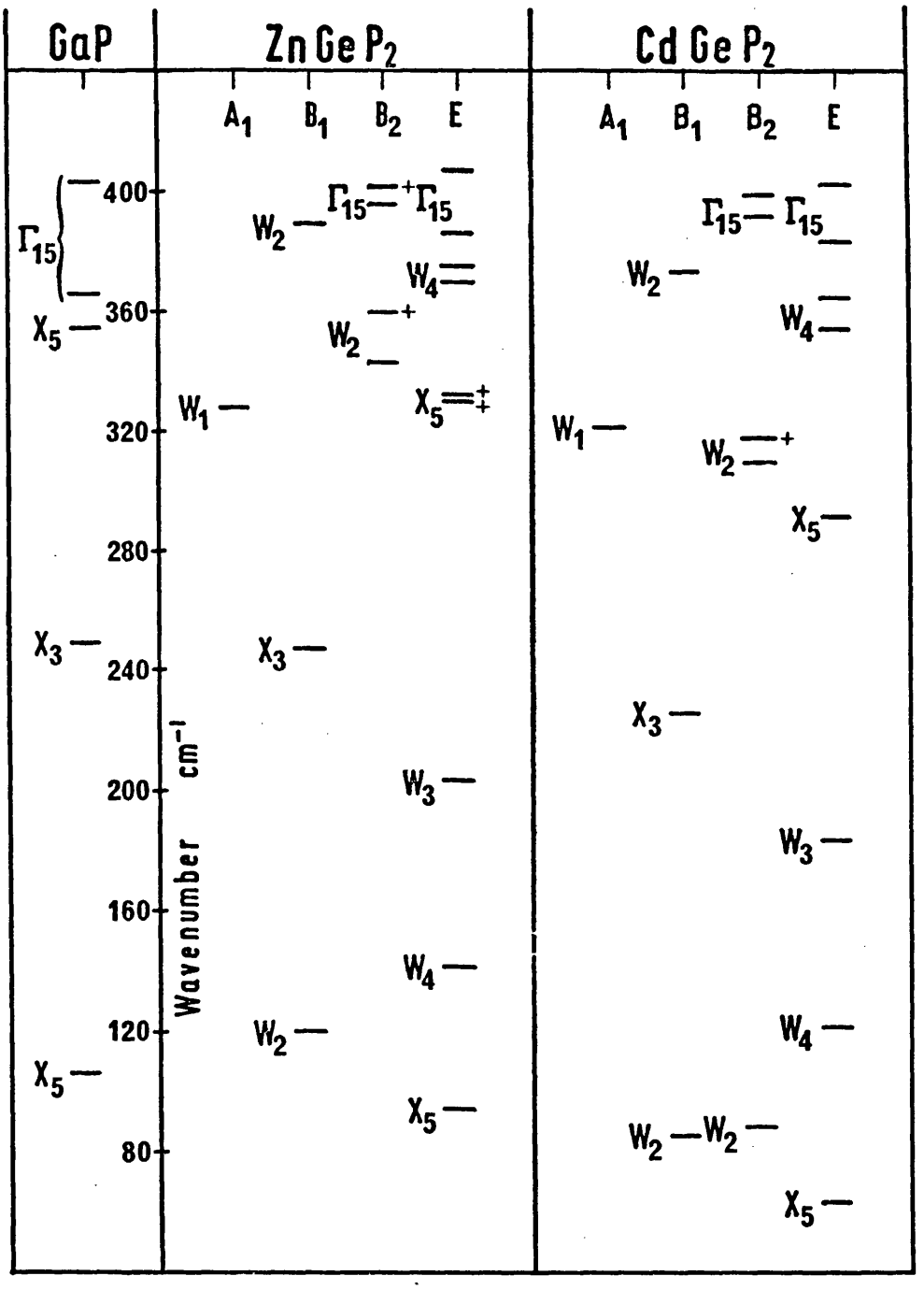

Figure 5.6 Raman modes compared to GaP. Modes not observed by Raman scattering which appeared in the i.r. are indicated by "+"

and the small splitting (3 cm^{-1}) of the corresponding modes in $CdGeP_2$ at 85 cm^{-1} supports this conclusion. The other unobserved mode is an E mode, which by comparison with the infrared results, seems to be the high frequency mode assigned, X_5, in figure 4.9. The infrared result for X_5 is included in figure 5.6.

A more detailed examination can now be made of the energies of the modes of $ZnGeP_2$ compared with those of GaP to determine how closely the symmetry modes chosen in Chapter 3 correspond to the normal modes of vibration in $ZnGeP_2$ because of the small mass differences of Zn, Ga and Ge. Since only the energies of Γ and X modes of GaP have been determined experimentally (99), Bettini has calculated the energies of X and W modes of GaP by a simple Keating model (152) for comparison with $ZnGeP_2$. This model is very limited and in particular, the transverse acoustic modes are not described correctly. However, a more elaborate model may not assure a correct extrapolation as can be seen from the shell model fit for Ge (102), and only a simple model may be capable of being extended to try to predict chalcopyrite phonon energies with the present spectroscopic data alone. The model is essentially the same as that used for the calculation of the elastic properties of zinc blende compounds by Martin (100), in which interatomic forces are resolved into bond stretching forces, α, and bond bending forces, β, of the strongly directional tetrahedral bonds, as in the valence force model (96). Only nearest neighbours are considered, and coulomb forces are accounted for by a rigid ion model. Thus, there are only three parameters, α, β and Z (the effective ionic charge), which are determined by a least squares fit to four vibrational frequencies. A check on germanium gave W mode frequencies within a few per cent of measurements by Nilson et al (102) for all

optical and longitudinal acoustic modes. The results for GaP are listed in Table 5.6 with the four frequencies chosen for the fitting indicated. The X_1 frequency is the only check on the accuracy of the model for GaP.

The observed $ZnGeP_2$ mode frequencies are within 8% of the W mode frequencies down to W_3, after which the model fails. This is interpreted as implying that the model is giving reasonable values of the W points for GaP, and that the $ZnGeP_2$ normal mode frequencies must correspond fairly closely to them. The experimentally determined GaP frequencies at Γ and X also suggest that $ZnGeP_2$ modes are close to GaP, and so the normal modes of GaP which were chosen as symmetry modes for $ZnGeP_2$ are close to the normal modes. The allocations given to the observed modes of $ZnGeP_2$ in figure 5.6 indicate the closest GaP mode. The effect of the chalcopyrite structure is thus small enough in this case to be considered as a perturbation on the GaP motions, and the effects of this perturbation can now be examined.

As Γ_{15}, W_4 and X_5 modes have E irreducible representations in chalcopyrite, there can be mixing of these modes. An indication of this may be the fact that the $X_{5_{opt}}$ mode has less energy than the GaP mode while the $W_{4_{opt}}$ mode has more energy according to the calculated result. The acoustic X_5 mode of $ZnGeP_2$ has also moved to lower energy. (The assignment of the low frequency modes X_5 and W_4 are made by comparison of the ordering obtained from the Keating model calculation, although the eigenvalues do not agree well).

The LO-TO splitting of the Γ_{15} modes are much reduced in $ZnGeP_2$. This could be the effect of the different ionicities of the chalcopyrite bonds, or it may be another consequence of the

Table 5.6 Comparison of $ZnGeP_2$ and GaP

GaP			$ZnGeP_2$		
mode	calc. cm^{-1}	expt. cm^{-1}	expt. cm^{-1}	mode	measurement
X_{5ac}	166	107	94	E	R
W_{2ac}	181		120	B_1, B_2	R
W_{4ac}	195		141	B_2	R
W_3	216.5		203	E	R,i.r.
X_3	242.5	250+	247	B_1	R
W_1	324.5		328	A_1	R
X_{5opt}	344.5	354+	330,332	E_T, E_L	i.r.
W_{4opt}	347.5		369,375	E_T, E_L	R,i.r.
X_1	364	366		A_2	inactive
W_{2opt}	374.5		343,360	B_{2T}, B_{2L}	R,i.r.
			389	B_1	R
Γ_{15T}	377	367+	386,396	E_T, B_{2T}	R,i.r.
Γ_{15L}	409.5	403+	406,401	E_T, B_{2L}	R,i.r.

+ see text

mixing of the group of high frequency polar modes. The splitting of Γ_{15} is larger for E modes than for B_2 modes in both $ZnGeP_2$ and $CdGeP_2$. The tetragonal compression may contribute to this difference although the splittings are remarkably similar in the two compounds considering the difference in tetragonal compressions ($ZnGeP_2$, $c/a = 1.960$; $CdGeP_2$, $c/a = 1.876$).

A very marked and unexpected effect of the chalcopyrite structure is the splitting of B_1 and B_2 high frequency, W_2 modes. The B_2 mode at $348cm^{-1}$ is shown in figure 3.9, and is the motion of the phosphorus atoms moving towards incoming zinc and germanium atoms which are moving in antiphase. This is expected to be a fairly weak Raman mode as verified by examination of figure 5.4. The B_1 motion is similar, but in this case, the phosphorus moves towards two incoming zinc atoms in antiphase in one half of the motion and incoming germanium atoms in the other half. This causes stronger Raman scattering as observed in figure 5.4. The higher frequency of the B_1 mode is thus an indication of the difference in force constant of the Zn-P and Ge-P bonds.

$CdGeP_2$ energies can be explained in terms of the above interpretation of $ZnGeP_2$. The perturbation from the $ZnGeP_2$ symmetry modes will be enhanced by the heavier cadmium atom replacing zinc. The force constant of the IV-V bond will be very similar to $ZnGeP_2$ since it is mainly determined by the bond stretching nearest neighbour force constant, while X-ray investigation (18, 19) shows that the phosphorus atoms form an almost exact regular tetrahedral arrangement around the germanium atoms in both materials. The bond stretching force constants of the II-V bonds will be similar, but the bond bending constant will be modified due to the different distribution of phosphorus atoms relative to cadmium atoms indicated by the x-parameters and tetragonal compression.

The Γ_{15} modes of $CdGeP_2$ are very close to those of $ZnGeP_2$ and the LO-TO splitting similar. The motion will thus be similar to that of $ZnGeP_2$, but modified by a much reduced cadmium displacement compared to zinc, leaving the frequency to be determined mostly by the germanium and phosphorus masses and IV-V force constant. As one goes to lower energies, the modes become more acoustic-like, and so the cadmium will take part much more in the motion and hence slow it down compared to $ZnGeP_2$. This trend can be seen for the whole spectrum in Table 5.6 with the exception of the unique W_1 mode. This is the motion of the phosphorus atoms alone, figure 3.3, and so it is very close to that of $ZnGeP_2$ and GaP. Agreement is good with the two other phosphides investigated by Raman scattering, $ZnSiP_2$, 344 (cm^{-1}) (101), $CdSiP_2$, 326cm^{-1} (121), $ZnGeP_2$ 328cm^{-1}, $CdGeP_2$, 321cm^{-1}.

CHAPTER 6 Electronic structure

6.1 Introduction

As for the phonon spectra of chalcopyrite compounds, the electronic band structures have been discussed in terms of binary compounds. However, the visible and ultraviolet reflection spectra are much more complex than those of their analogues. Additional interest in the optical properties in this region comes from the possible application of the materials in light detectors or light emission devices.

Three techniques were used in this study and will be described in this chapter. Electroreflectance, a sensitive modulation technique was used to determine the energy of direct transitions in the Brillouin zone. A measurement of the variation of the absorption coefficient with incident photon energy gave the nature of the lowest transitions, and polarisation modulation was used to measure the birefrigence of the materials at and above the band gap.

6.2 Theoretical band structure

Section 1.3 gave the Brillouin zone of the chalcopyrite structure, and explained the method of obtaining a first approximation to any of the II-IV-V_2 band structures by embedding the structure of the isoelectronic III-V analogue into this zone. The resulting direct and pseudodirect structures derived from direct and indirect analogues were given by Shay and Wernick (14) and are shown in figures 6.1 (a) and (b) respectively. GaP has an X_1 lowest minimum, so that $ZnGeP_2$ should correspond to the structure shown in figure 6.1 (b) with Γ_3 the lowest minimum. The analogue of $CdGeP_2$ is $Ga_{0.5}In_{0.5}P$. InP has a direct energy gap. Averaging GaP and InP band structures indicates that $CdGeP_2$ should correspond to the structure

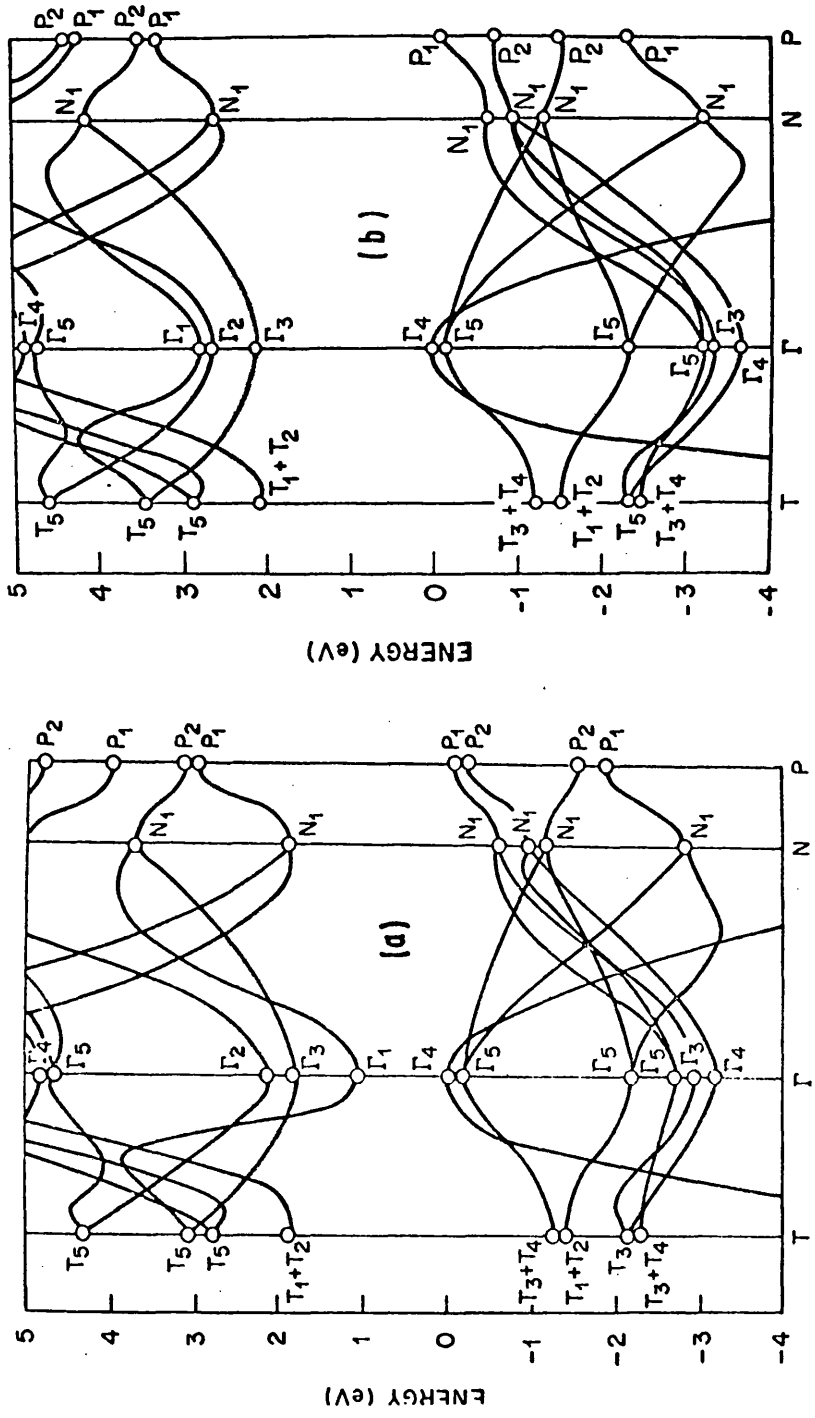

Figure 6.1 Thecretical band structure of (a) direct and (b) pseudo-direct chalcopyrite compounds.

shown in figure 6.1 (a), with a lowest minimum, Γ_1. The Γ - X cross over was found to occur for x = 0.63 in $Ga_xIn_{1-x}P$ by Alibert et al (153).

The valence band structure will also be modified in going from the zinc blende to the chalcopyrite structure. If spin is neglected, the valence bands of zinc blende are composed of four sub-bands. Three upper p-like bands are degenerate at the zone centre and are labelled Γ_{15} in figure 1.8. The fourth band is s-like and assigned Γ_1. The symmetry notation follows Parmenter (154). Away from the zone centre, the three fold degeneracy of Γ_{15} is split into two bands which are approximately parabolic with different curvatures. The smaller curvature is doubly degenerate and called the heavy hole band, V_1 and the larger curvature is called the light hole band, V_2. All of these bands have a further degeneracy of two due to spin however. Spin also removes the degeneracy of V_1 and V_2 at the zone centre due to spin-orbit coupling. This effect is due to the interaction of the magnetic moments associated with the spin and the orbital angular momentum of an electron which will be different for V_1 and V_2.

Figure 6.2 shows the splitting of the zone centre Γ_{15} valence band in going from zinc blende to chalcopyrite. Again neglecting spin initially, the chalcopyrite lattice causes a crystal field splitting of the doubly degenerate V_1 band into Γ_4 and Γ_5. This crystal field splitting is caused by the three effects contributing to the distortion of the lattice from cubic,

(1) tetragonal compression, (2) internal parameter, $x > \frac{1}{4}$,

(3) ordering of the two cations. Now introducing spin-orbit interaction further splits Γ_5. Spin introduces new symmetry operations

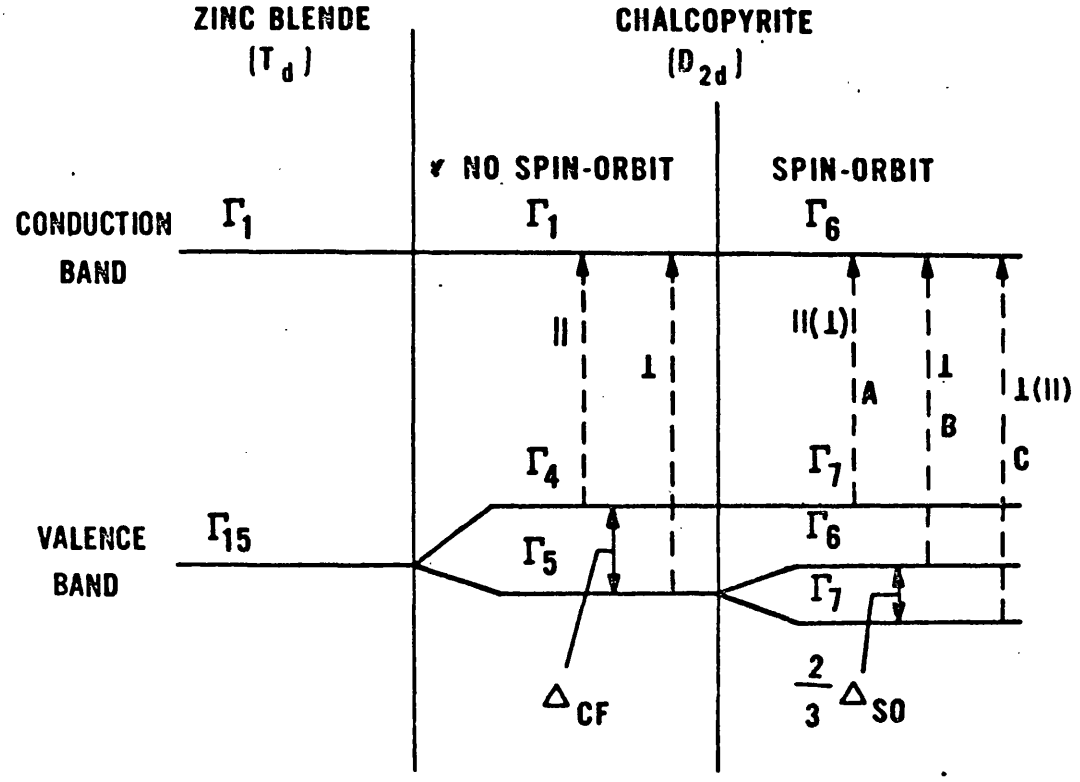

Figure 6.2 Effects on the valence bands of crystal field and spin orbit interactions

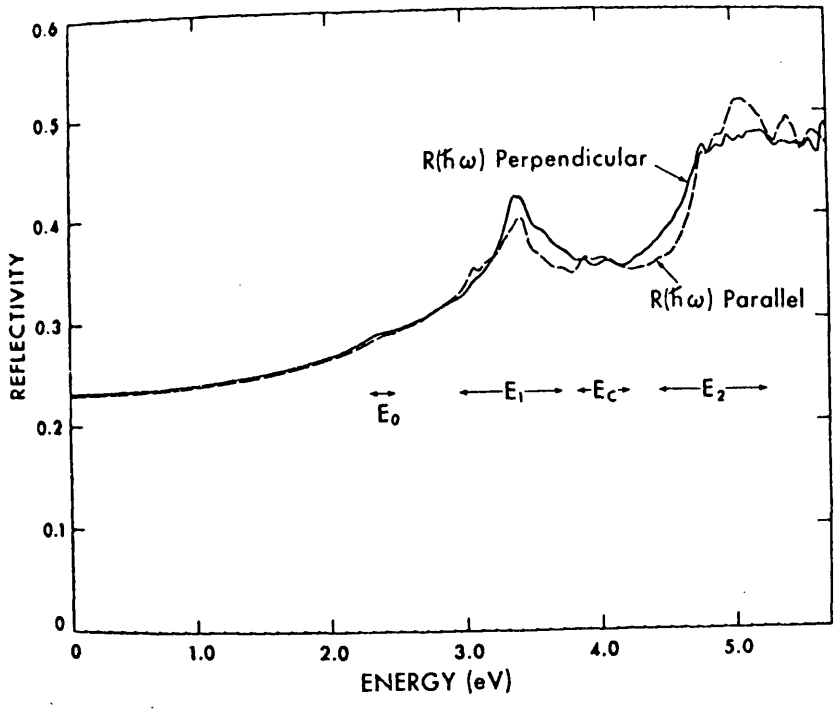

Figure 6.3 Theoretical reflectivity spectrum of $ZnGeP_2$

into the space group, and a double group is used which gives the new notation, Γ_6, Γ_7 of figure 6.2. Hopfield (155) has used a model for the splitting of p-like levels in a cubic crystal when it is strained along [001] . Rowe and Shay (156) have applied this to the chalcopyrite structure by assuming that the tetragonal compression is the dominant effect in crystal field splitting. The energy of Γ_7 levels relative to Γ_6 is then given by,

$$E_{1,3} = -\tfrac{1}{2}.(\Delta_{cf} - \Delta_{so}) \pm \left\{(\Delta_{cf} - \Delta_{so})^2 - \frac{8}{3}\Delta_{so}\Delta_{cf}\right\}^{\frac{1}{2}} \qquad 6.1$$

when $E_2 = 0$.

Shay et al (14) showed that the diagonalisation of the Hamiltonian matrix giving the eigenvalues in equation 6.1 also yields wavefunctions from which polarisation intensity ratios can be determined. The ratio of the strengths of the transitions from a Γ_7 valence band to the Γ_6 conduction band, figure 6.2, for light polarised parallel and perpendicular to the optic axis is,

$$\frac{I_{||}}{I_{\perp}} = \left(2 + \frac{3E}{\Delta_{so}}\right)^2 \qquad 6.2$$

Shay has verified the quasicubic model approach by comparing the results of experiments for different compounds with the theoretical value of the crystal field splitting, $\Delta_{cf} = \frac{3}{2}.b.(2 - \frac{c}{a})$. b turns out to be -1.2eV compared to -1.5eV in III-V compounds.

Several band structure calculations have been made on II-IV-V_2 compounds using a pseudopotential approach. Poplavnoi et al (157, 158, 159) have made calculations for several compounds and the results have been reviewed by Goryunova et al (10). The two types of chalcopyrite band structure deriving from direct and indirect III-V analogues have also been studied by Morgan (160) by extending pseudopotential calculations on GaAs and GaP to the $I\bar{4}2d$ space group. Varea de Alvarez and Cohen (161) similarly calculated the band structure

of $ZnGeP_2$ with no experimental fitting parameters and produced the theoretical reflectivity spectrum shown in figure 6.3. The complexity of this spectrum is due to the4:1 mapping from zinc blende, giving four times as many bands at any value of $\underline{k}$, and thus only a detailed band calculation can be used for interpreting observed structure. Indeed, an attempt has been made to assign positions in the Brillouin zone to only the first four peaks out of the twelve normally observed between the band gap and 6 eV.

The transition probability is highest at critical points known as Van Hove singularities. These occur for the condition, $\nabla_{\underline{k}}(E_c - E_v) = 0$ where E_c and E_v are the energies of conduction and valence bands respectively. The strong reflection peak in the reflectivity spectrum of III-V compounds above the band gap is thought to arise from direct transitions in the Λ, [111] direction towards the L point where valence and lowest conduction bands are parallel over a large region of the Brillouin zone. Five sixths of this direction is retained in chalcopyrite, figure 1.7. The L point itself, however, maps to N which is along [110]. Zinc blende compounds show a doublet, E_1 and $E_1 + \Delta_1$, due to the splitting of the V_1 valence bands. This is to be compared with the four peaks, which are made up of two doublets, in this region for chalcopyrite compounds.

Several possible explanations have been given. Two of the peaks may correspond to E_1 and $E_1 + \Delta_1$ peaks of zinc blende in the retained section of the Λ direction, and the other two derive from the N point (162). Alternatively, it has been suggested by Kavaliauskas et al (163) that all four peaks derive from the N points. Shay (164) has pointed out that both V_1 valence bands will be further split in chalcopyrite due to spin-orbit and crystal field splittings.

Two doublets would then be observed which originate from the Λ-direction.

6.3 Review of previous work

Various optical techniques such as absorption (165), reflection (162, 166, 167), electroreflectance (168-185), thermoreflectance (183, 186) and wavelength modulation (187) have been used to study the band structures of II-IV-V_2 compounds in the last few years.

Electroreflectance has given the position of the direct transitions accurately in most materials and the results have been compared with the measured absorption edges to decide whether the lowest transition is direct or indirect.

A study of the absorption edges and their hydrostatic pressure dependences has been carried out by Bendorius et al (165) for eleven compounds. The results show that the absorption edges are quite different for the high band gap compounds, $ZnGeP_2$, $ZnSiP_2$, $CdSiP_2$ and $ZnSiAs_2$. The comparison of the pressure dependences of these edges with III-V compounds shows that the absorption edge is due to either indirect or pseudodirect transitions deriving from the X point in zinc blende.

Shay et al (168) observes the lowest strong electroreflectance peaks for $ZnGeP_2$ at 2.33, 2.40 and 2.48 eV and weak peaks at 2.05eV and 2.11eV, which are attributed to pseudodirect transitions. Thermoreflectance also showed weak structure in the vicinity of 2.06 and 2.3eV(186). Wavelength modulation experiments by Babonas et al (187) in the same material gives three distinct peaks at 1.99, 2.05 and 2.12 eV at room temperature, which correspond well with the energy splitting of the valence bands measured by Shay with electro-reflectance.

Shay et al (169) obtained electroreflectance structure at 1.72, 1.90 and 1.99eV for $CdGeP_2$. The absorption edge measured by Shay et al (169) and Gorban et al (188) shows a steep rise close to 1.72eV indicating a direct band gap. A shoulder on the absorption edge is interpreted as being due to a free exciton with a binding energy of 7.7 meV.

Sobolev et al (166) and Stockowski (162) have observed higher energy band transitions in several compounds by reflectivity measurements. Petroff et al (167) measured the reflectivity of $ZnGeP_2$ between 2 and 6 eV with polarised light, and compared the results with the pseudopotential calculations made by de Alvarez and Cohen (161), figure 6.3, to interpret the position of the structure in the Brillouin zone.

The polarisation technique has only previously been used by Bettini (189) for the investigation of $CuAlS_2$, $CuGaS_2$ and $CuInS_2$.

6.4.1 The electroreflectance technique

This technique is but one of a series of active modulated reflectance methods possible for the study of the electronic band structure of semiconductors (190, 191). All have the common feature of modulating the reflectance of a sample through a periodic change of some external parameter of the material. Phase sensitive detection separates the modulated reflectance from the background reflectance. The main advantage of modulation is in the spectral width of the structure which may be 20 to 50 times smaller than the width of the reflectance structure. There is no response over large regions of the spectrum, suggesting that only limited areas of the Brillouin zone are affected by the modulation.

In electroreflectance, an a.c. electric field is applied to the material. The result of an extra potential energy term, -E.x, in the one electron Hamiltonian of the unperturbed crystal destroys the invariance to lattice translation in the x direction of the electric field, $\underline{E}$. Franz (192) and Keldysh (193) considered the effect of a static field on band structures. If it is assumed that the perturbing field is smaller than the crystalline fields, then a local band structure exists at every point in real space. In real space, the energy gap disappears, figure 6.4, over the whole crystal, but because of the decreasing overlap of the valence band and conduction band wave functions, the absorption coefficient decays exponentially with $(\hbar\omega - E_g)$. The energy gap is thus apparently decreased in a transmission experiment due to the tunnelling effect

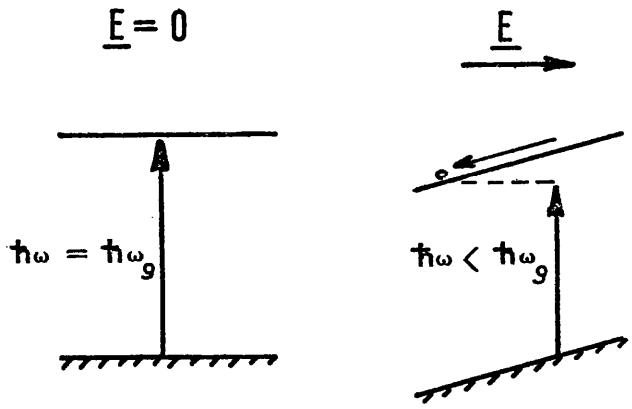

Figure 6.4 The effect of an electric field on the band gap in real space.

of the overlapping wavefunctions. The tunnelling probability is given in terms of Airy integrals (194) which give an oscillating component to the real and imaginary parts of the dielectric constant as a function of photon energy. Theory shows (194) that the maxima of these oscillations vary in energy with increasing field except for the peak near to the band gap. Thus, when a modulating field is applied, this causes a modulation in the absorption or reflection spectrum. This situation is also found at Van Hove singularities in the joint density of states other than at the band gap.

The quantity measured in electroreflectance is the fractional change in reflectivity, $\Delta R/R$, produced by applying the voltage. The analysis of the peak shape is complicated by other contributing effects. The modulation of the electric field also influences the electron-lattice and electron-hole interactions and the relation between $\Delta R/R$ and the dielectric constant is not easy to derive because of effects such as inhomogeneities in the field. However, because of the sharpness of the spectra, the maximum position of the peak in $\Delta R/R$ is assumed close to the energy of the singularity.

6.4.2 . Electrolytic electroreflectance experimental method

The transitions to be investigated by the electroreflectance technique are in the high absorption region at and above the band gap. The absorption coefficient may be 10^4 to 10^6 cm^{-1} so that the depth of material contributing to the reflection will be less than one micron. The electric field will have most affect on the reflectivity if it is applied only in this region. This can be done conveniently using a semiconductor-electrolyte junction (195).

When a semiconductor is used as one of the electrodes in an electrolytic cell, the situation at the boundary is rather like a p-n junction. There will be a depletion layer in the semiconductor and

a surface charge layer (Gouy layer) in the electrolyte. A very thin layer, called the Helmholtz layer, also exists in the electrolyte very close to the semiconductor but may be neglected. For a high conductivity electrolyte, the Gouy layer can be made very small ~ 5 Å whereas the width of the depletion layer is of the order of a micron. The second electrode is normally platinum, so that one volt applied across the cell may introduce a field of 10^4 volts. cm^{-1}. across this layer.

The electrolytic electroreflectance technique developed by Cardona et al (196) is suitable for room temperature measurements with aqueous electrolytes. The apparatus is shown in figure 6.5. The solution was 0.10M K_2SO_4, cleaned by gettering with freshly crushed germanium. Electrical contact was made to the crystal by attaching it to a copper rod with silver paste. An ohmic contact was not necessary. The bar and all but the reflecting face were then potted with epoxy resin and the crystal face finally cleaned by an etch in 1 conc. HNO_3 : 1 conc. HCℓ. The current-voltage characteristic of the cell was observed on an x-y oscilliscope when an a.c. voltage from an audio frequency generator was superimposed on a d.c. bias.

A quartz iodine, 250 W. lamp and a Leiss monochromator were used, and the light focussed onto the sample, as shown in figure 6.5, after passing through a polariser. The quartz sample cell was rotated slightly to minimise the light reflected from the cell window into the collecting system. The signal from the photomultiplier was first taken to the control circuit shown in greater detail in figure 6.6. This is a feedback device which controls the voltage across the dynode chain of the photomultiplier to keep the output d.c. signal constant at the value of a reference voltage applied to a differential amplifier in the circuit. The signal was taken to a low noise amplifier and phase sensitive detection system using the A.F.O. frequency

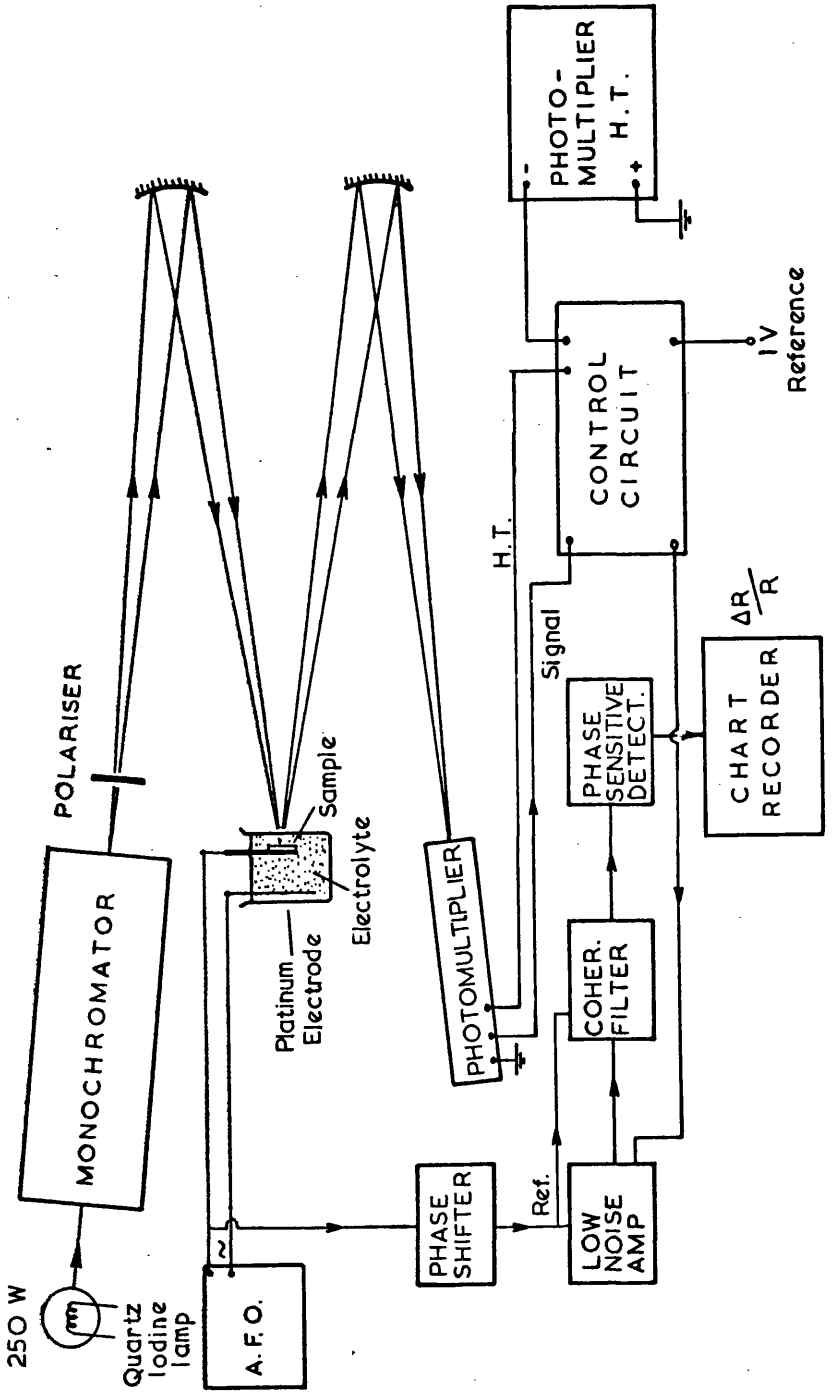

Figure 6.5 Electroreflectance apparatus

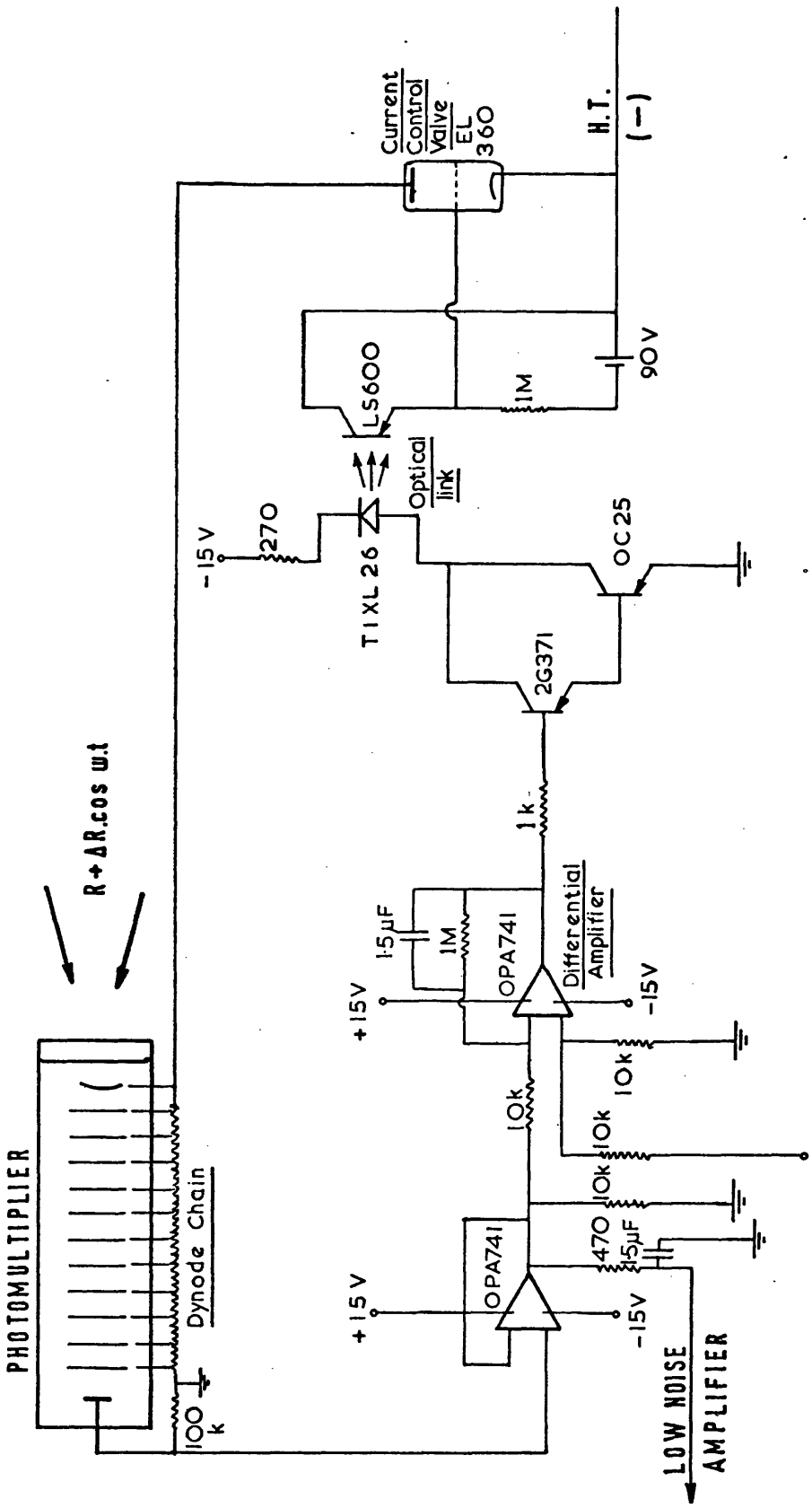

Figure 6.6 Electroreflectance control circuit

as a reference. By fixing the reference at one volt, the output from the p.s.d. in volts, gave the value of $\Delta R/R$.

6.4.3 Electroreflectance results

The use of the electrolytic electroreflectance technique usually depends on low resistivity crystals to obtain the high electric field in the surface depletion layer. The electrical results of section 2.5.2 give room temperature resistivities of 10^3 Ω.cm for $ZnGeP_2$ and 10^5 Ω.cm for $CdGeP_2$. These values are rather high but successful results were obtained for both materials as shown in figures 6.7 and 6.8.

The spectra were measured using (112) faces so that only 2/3 of the light intensity lies along the c-axis for the spectrum labelled E||c, as discussed in section 4.3.1. The two polarisations of each sample were taken under identical conditions.

The $ZnGeP_2$ spectra were obtained with applied voltages, -2V d.c. and 4V a.c. peak to peak. This lay in the rectifying part of the I-V characteristic of the cell. The modulation frequency was 920 Hz. The peaks A, B and C were the lowest energy structure observed and show the three-fold splitting of the valence band at the zone centre. They agree with the polarisation dependences for transitions to the Γ_6 conduction band shown in figure 6.2. Table 6.1 shows the results compared to the electroreflectance results of Shay et al (168) measured on crystals grown from the m elt with gallium diffused into reduce the resistivity to 10 Ω.cm. Good agreement is obtained but both sets of results show a slight divergence from thermoreflectance measurements by Raudonis et al (186). This may be due to the difference in method. The spin orbit and crystal field splittings calculated from equation 6.1 are also given in Table 6.1.

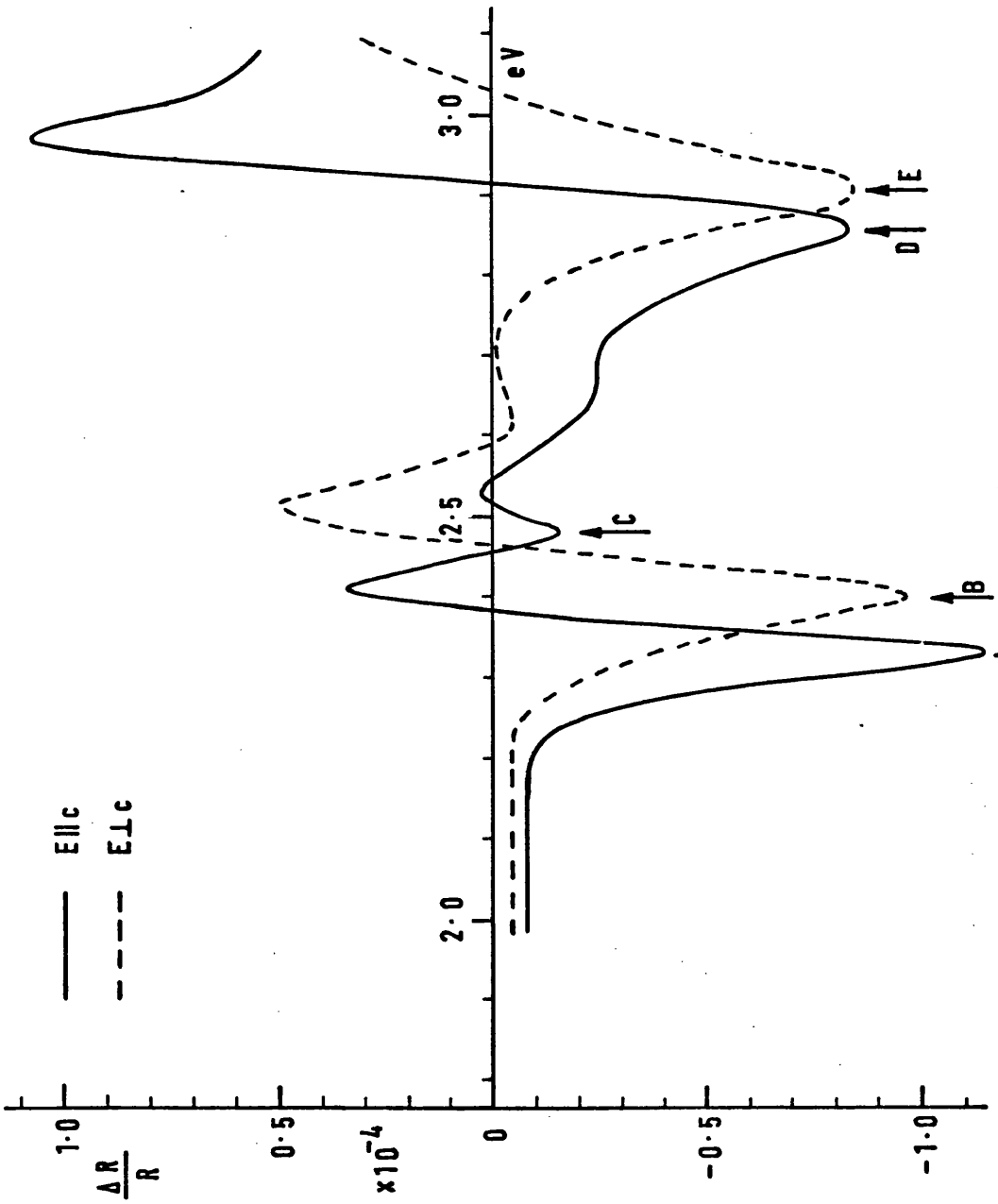

Figure 6.7 Electroreflectance spectra of $ZnGeP_2$

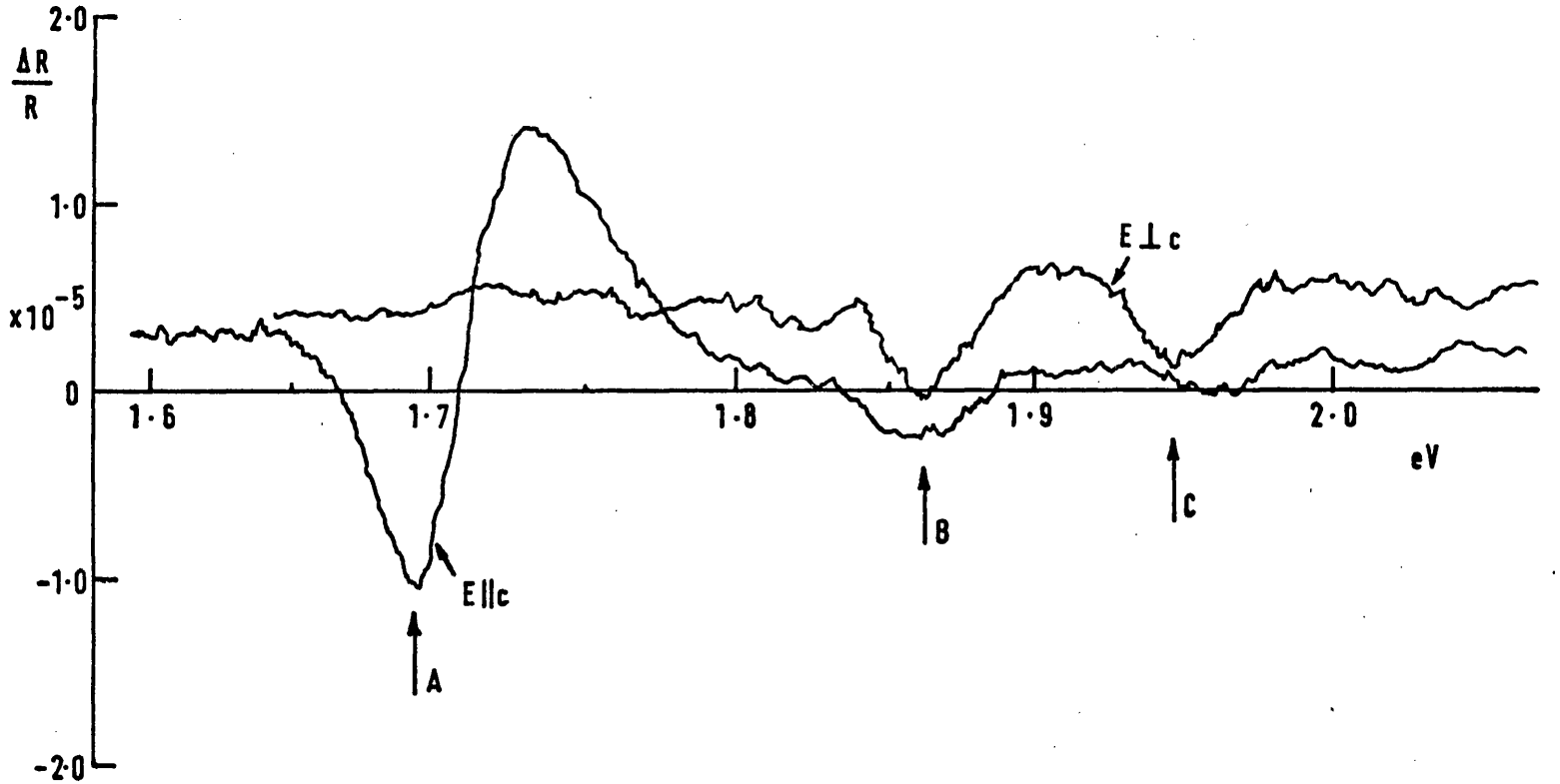

Figure 6.8 Electroreflectance spectra of $CdGeP_2$

Table 6.1 Electroreflectance results for $ZnGeP_2$

Peak	pol.	This work (eV)(300^oK)	Shay et al (168) Electrorefl.(300^oK)	Raudonis(186) Thermorefl.(320^oK)
A	$\parallel$	2.33	2.34	2.39
B	$\perp$	2.40	2.40	2.46
C	$\parallel$	2.48	2.48	2.52
D	$\parallel$	2.86		
E	$\perp$	2.91		
Δ_{so}		0.074		
Δ_{cr}		-0.064		

Table 6.2 Electroreflectance results for $CdGeP_2$

Peak	pol.	This work (eV)	Shay et al (169) Trans. electro.
A	$\parallel$	1.70	1.72
B	$\perp$	1.86	1.90
C	$\perp$ ($\parallel$)	1.95	1.99
Δ_{so}		0.12	0.11
Δ_{cr}		-0.19	-0.20

The pseudodirect transitions which were observed weakly by Shay at around 2.1eV and more strongly by Raudonis were not detected above the noise level in $\Delta R/R$ of 10^{-6}. The peaks D and E derive from transitions elsewhere in the Brillouin zone as discussed in section 6.2 and will be considered in section 6.6.2.

The electroreflectance spectrum of $CdGeP_2$ is shown in figure 6.8. Due to the high resistivity of the crystals, the spectrum is rather weak, but is comparable in strength to transverse electroreflectance measurements made on this material by Shay et al (169). Table 6.2 compares the results of the two studies. Only the three lowest zone centre transitions A, B and C were observed in both cases. The values obtained in the present work are seen to be slightly lower than those of Shay. This could arise from the difference in method used but may also be due either to crystal purity or the lower resolution of this work.

6.5.1 Absorption apparatus

The steep rise in the absorption coefficient due to lowest band gap transitions was investigated by measuring the transmission and reflectance properties of plane parallel platelets. Crystals were first mounted on a stainless steel polishing jig shown in figure 6.9. Two outer rings were adjusted to the crystal thickness and initial polishing was on 600 grade silicon carbide paper. This was followed by a polish on paper impregnated with six micron diamond paste and a final polish was carried out on one micron diamond until no scratches were visible on the crystal face when inspected under a microscope with magnification x 40. The crystal was then turned over and the procedure repeated. The thicknesses of the platelets were measured by comparing the edge of the crystal with standard sizes of platinum wire under a microscope.

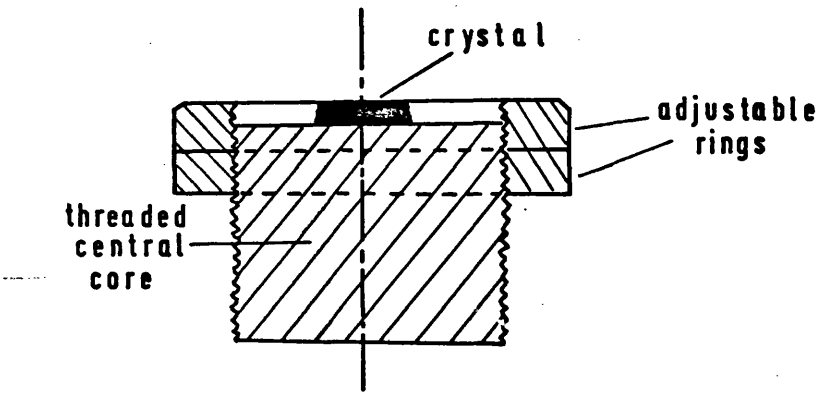

Figure 6.9 Cross section of polishing jig

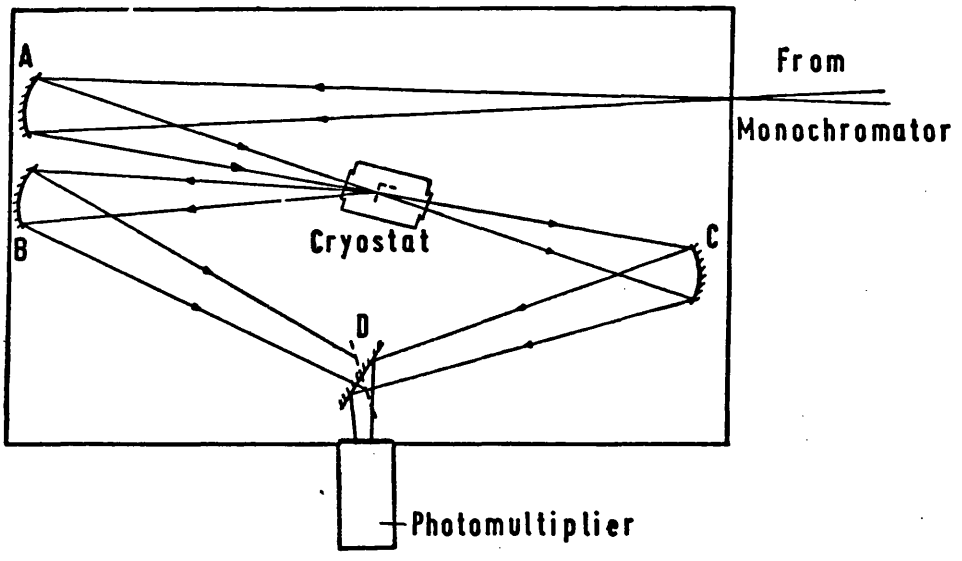

Figure 6.10 Absorption apparatus

The apparatus used to measure the transmission and reflection of the samples is shown in figure 6.10. Light from a Leiss double prism monochromator was focussed onto the sample by a spherical mirror, A. The crystal platelet covered a hole in a thin brass plate inside a cryostat. The plate was attached to a central rod which extended from the top of the cryostat so that the brass plate could be rotated about a vertical axis. Another plate with an identical hole was mounted at 90° to the sample plate so that, for transmission measurements, the intensity of light transmitted through the crystal could be compared with an empty hole, and for reflection measurements the reflected intensity could be compared to the intensity reflected from a freshly aluminised plane mirror mounted behind the hole. The holes had been cut together by spark erosion. Transmitted or reflected light was collected by mirrors C or B and directed towards a plane mirror, D, and then into a photomultiplier with either an S1 or S20 photocathode response. The mirror, D, had two positions to collect either the transmitted or the reflected light. The entire system was enclosed in a black box with baffles placed between the various light paths to cut down scattered light.

A water cooled 150 W quartz iodine incandescent lamp was used as source and the light was mechanically chopped at 800 Hz before entering the monochromator. A reference signal was taken from a photocell in the chopper and used to compare with the signal from the photomultiplier in a Brookdeal 411 phase sensitive detector.

The voltage stability of the Oltronix A2.5K - 10R photomultiplier supply was 0.02 per cent per hour, and after the lamp had been on for an hour, the stability of the light intensity measured with the photomultiplier was 0.2 per cent per hour.

6.5.2 Determination of the absorption coefficient

The transmission and reflection coefficients were measured at 0.01 eV intervals up to the limits of detection of the signal over the background in the high absorption region. The background was typically 10^{-4} of the intensity of the light passing through the empty hole. A background correction was made by measuring the intensity of light reaching the detector when the sample was rotated on its mount, out of the light beam. Above the high absorption limit, this background followed the same curve as the measured light intensity with the crystal in the transmission position, showing that monochromatic light scattering in the absorption apparatus was more significant than scattered light from the monochromator.

The transmission coefficient for a plane parallel sided crystal is modified by multiple reflections (125), so that the measured value is,

$$T = \frac{(1 - R)^2 . \exp(-\alpha.d)}{1 - R^2 . \exp(-2.\alpha.d)} \qquad 6.3$$

where α is the absorption coefficient, d is the crystal thickness, and R is the surface reflection coefficient. The measured reflectivity, r, is given by,

$$r = R(1 + T.\exp(-\alpha.d.)) \qquad 6.4$$

Combining equations 6.3 and 6.4, gives,

$$\alpha = \frac{1}{d} . \ln \left[\frac{T(A+2) - T(A^2 + 4T^2)^{\frac{1}{2}}}{A - 2T^2 + (A^2 + 4T^2)^{\frac{1}{2}}} \right] \qquad 6.5$$

where $A = T^2 - (r - 1)^2$

6.5.3 Absorption results

The variation of the absorption coefficient with incident photon energy for E||c and E $\perp$ c using 50 micron (112) platelets at both room temperature and 90K are shown in figures 6.11 and 6.12 for $ZnGeP_2$ and $CdGeP_2$ respectively.

The large difference in the slopes of these curves for the two

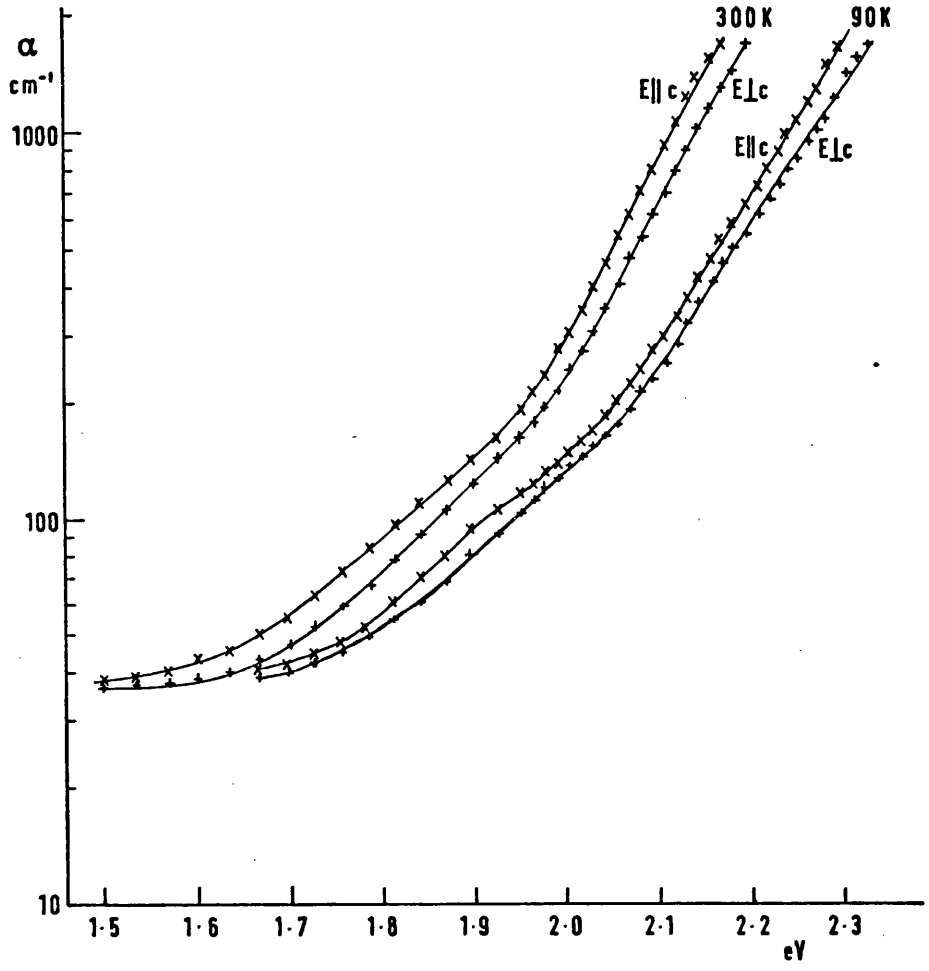

Figure 6.11 Absorption edge of $ZnGeP_2$

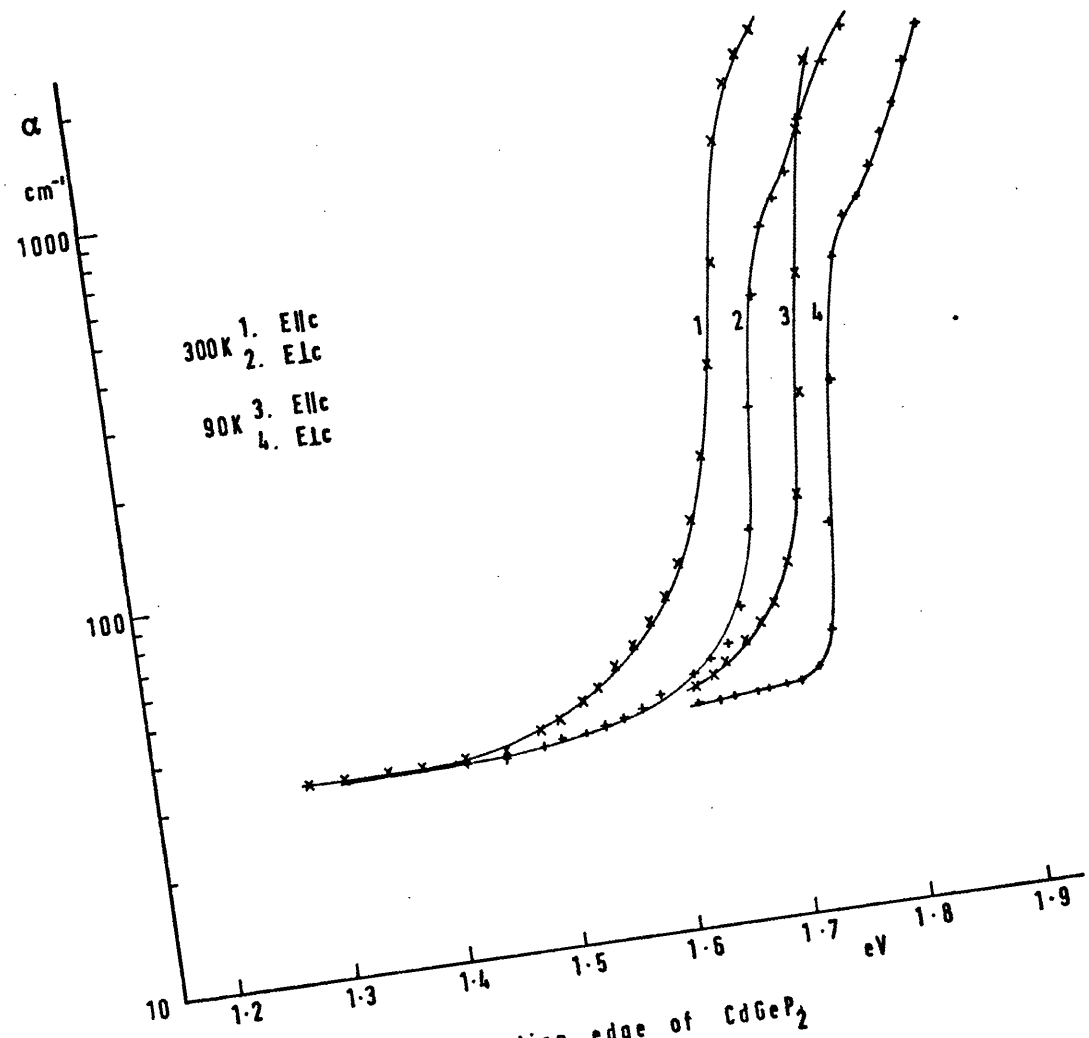

Figure 6.12 Absorption edge of $CdGeP_2$

materials indicates different origins for the absorptions. The $CdGeP_2$ absorption edge is very sharp and near to the value of the A peak of electroreflectance, figure 6.8, confirming that $CdGeP_2$ is a direct gap material. At first sight it might be thought that the polarisation dependence of the absorption edge would be due to the transitions A and B observed in electroreflectance. However these peaks are separated by 0.16 eV in figure 6.8, whereas the observed splitting in the absorption is at most 0.08 eV. Shay et al. (168) interprets the polarisation dependence of the absorption edge in $CdSnP_2$ to be entirely due to the polarisation dependence of the A transition, given by equation 6.2. Substituting the values obtained from the electroreflectance of $CdGeP_2$ into equation 6.2 gives $I_{||}/I_{\perp} = 36$. E||c is only nominal so that $\alpha_{||}$ must be multiplied by 1.5, but the result for $\alpha_{||}/\alpha_{\perp}$ is much less than 36. This may be due to an impurity band tail obscuring the polarisation dependence. A shoulder is observed in all of the absorption curves and has been interpreted as being due to a free exciton by Shay et al (169). The shoulder appears in both polarisations at the same energy indicating that the curves do derive from the same source. The measured temperature dependence of the edge is $4{\cdot}4.10^{-4}$eV/K from 300 to 90 K and the slope given by the parameter $S = \Delta \ell n \alpha / \Delta \hbar\omega$ is 43 at 300K, measured for the steepest portion of E||c. This compares with published values of 45(169) and 28(165).

The slopes of the $ZnGeP_2$ absorption edges in figure 6.11 are much less steep, the polarisation dependence is much smaller than for $CdGeP_2$ and the rise in absorption begins well below the lowest transitions observed in electroreflectance in section 6.4.3. The room temperature value of 10 for the slope measured above 200 cm^{-1} compares with published values of 8 (165) and 6(34). The electronic

transition giving rise to absorption in $ZnGeP_2$ is not easy to identify from these results. From the argument of section 6.2, the lowest transition should be pseudodirect with an indirect transition to the T point close above it. The absorption of an allowed direct transition should vary as the square root with photon energy and an indirect allowed transition as the square. Plotting either of these functions of the absorption coefficient did not produce a linear dependence in the high absorption region. The absorption edge may thus be a combination of both of these transitions if they are close in energy. A significant steepening of log α is observed at 1.96eV at room temperature, which is near to the energy of the lowest pseudo-direct transition reported by Babonas et al (187) at 1.99eV. Bendorius et al (165) quote an energy gap of 2.0eV at room temperature by extending to zero a plot of the absorption coefficient which is fairly linear with energy at high values. Use of this method gives a value of 2.05eV at room temperature and 2.20eV at 90K in this work. The shift of the absorption edge with temperature is 6.5×10^{-4} eV/K measured at the highest absorption values. This is very close to the value of 6.2×10^{-4} eV/K for GaP (130).

6.6.1 The polarisation modulation technique

This method is conveniently carried out with the use of a device called a piezo-optical birefringence modulator manufactured by Morvue Electronic Systems (197). The polarisation of a beam of light is modulated by a high frequency 50 kHz modulation of the optical properties of a normally isotropic block of fused quartz through which the light passes. This is attained by a uniaxial strain produced in the fused quartz by a piezoelectric transducer of crystal quartz cemented to one end as shown in figure 6.13.

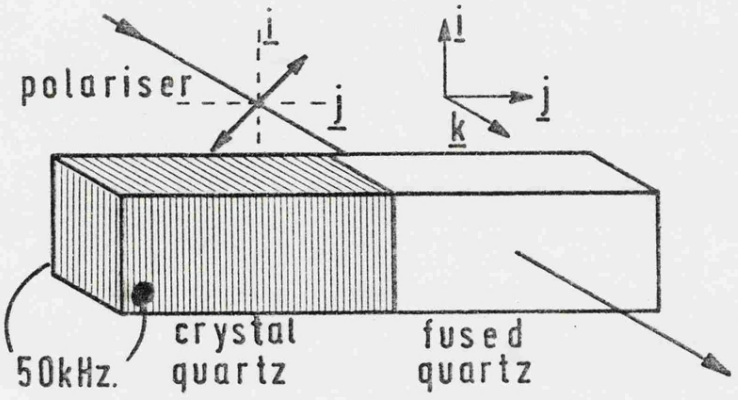

Figure 6.13 Polarisation modulator

The change in refractive index is a linear function of strain so that if one considers an incident beam of light travelling in the $\underline{k}$ direction, polarised at 45° to the strain direction along $\underline{j}$ then the phase difference between $\underline{i}$ and $\underline{j}$ components of the polarisation after traversing a thickness, d, of the quartz is given by,

$$\delta = \frac{2\pi d}{\lambda} .P. \sin \omega.t \qquad 6.6$$

where λ is the wavelength of the light and P is a number proportional to the peak strain amplitude.

With a suitable modulation amplitude, the emitted light can be made circularly polarised, $\delta = \pm^{\pi}/2$, at maximum strain amplitude, $\sin \omega.t = \pm 1$. The cycle of the modulated light will be from right circular polarised, through linear polarisation at 45° to $\underline{i}$ and $\underline{j}$, and then to left circular polarisation and back again. If a

circularly dichroic material is placed in this beam, then a phase shift will result between the left and right circularly polarised halves of the cycle. This phase shift is recorded by detection of the light with a photomultiplier and comparison of the intensity of the two halves of the cycle by phase sensitive detection locked to 50 kHz. If the material is linearly dichroic, with the axis placed along $\underline{i}$ or $\underline{j}$, then the same experimental set up gives the phase change due to the linear polarisation in the material if the phase sensitive detector is locked to twice the modulation frequency, 100 kHz.

Experiments were carried out by this method, except that the materials were observed in reflection instead of transmission due to the very high absorption in the materials. A 75 W quartz halogen lamp was used as source. The birefringences of $ZnGeP_2$ and $CdGeP_2$ are large and easily measurable at 100 kHz. The point group $\bar{4}2m$ is also optically active (47), so that light travelling along x and y crystal axes have opposite senses of rotation. The interband transitions could thus be observed by the anomalous optical activity at these frequencies. The results were normalised by dividing by the measured intensity of reflected light from the crystal at each wavelength. These experiments, at room temperature and 20K were carried out with Dr. C.R. Pidgeon at Heriot Watt University.

A third method, employed by Bettini (189) used small modulation amplitudes. The relation between the change of phase, θ, upon reflection and the dielectric constant is given by,

$$R^{\frac{1}{2}} . e^{i\theta} = \frac{\sqrt{\varepsilon} - 1}{\sqrt{\varepsilon} + 1} \qquad 6.7$$

where $\varepsilon = \varepsilon' + i.\varepsilon''$. At the E_o gap, ε' is fairly constant, and has a magnitude of about 10, section 4.4.1, thus one may expect $\varepsilon''^2/\varepsilon'^2 \ll 1$ and $\tan\theta \simeq \theta$ to be valid, in which case equation 6.7 can be expanded in a power series in $\varepsilon''/\varepsilon'$ and the phase change is

then approximately given by,

$$\theta = \frac{\varepsilon''}{(\varepsilon' - 1).\sqrt{\varepsilon'}} \qquad 6.8$$

The difference in phase shift for light polarised parallel and perpendicular to the optic axis is approximately,

$$\begin{aligned} \Delta\theta\ (\omega) &= \theta_{||}(\omega) - \theta_{\perp}(\omega) \\ &= \frac{\varepsilon''_{||}\ (\omega) - \varepsilon''_{\perp}\ (\omega)}{(\varepsilon' - 1)\ \sqrt{\varepsilon'}} \end{aligned} \qquad 6.9$$

where ε' is assumed to be equal for both polarisations and constant in wavelength.

After reflection from the crystal, the light is passed through an analyser crossed with the polariser shown in figure 6.13. The measured signal then consists of a 100 kHz component, which is proportional to the amplitude of the modulation, and a 50 kHz component which is proportional to the phase shift and the modulation amplitude. The ratio of the signals, I_{50kHz} / I_{100kHz} then gives the phase shift on reflection in arbitrary units. This method was carried out at room temperature and 5K at the Max Planck Institute, Stuttgart with M. Bettini.

6.6.2 Polarisation modulation results

All three methods described in the previous section produced very similar results. The A, B and C peaks observed in electroreflectance were not resolved in either $ZnGeP_2$ or $CdGeP_2$. This is surprising since Bettini resolved these transitions in similar work on four I-III-VI_2 compounds (189). The spectra obtained by the latter method, using small modulation amplitudes, are shown in figures 6.14 and 6.15. At the positions of the lowest direct transitions, the reflectivity shows broad peaks slightly higher in energy than the A peaks of electroreflectance. In both materials, $R_{||} > R_{\perp}$, so that the A transitions, which absorb light mostly with polarisation E||c, seem to dominate the spectra in this region. The changes in energy of the maxima of the peaks with temperature are very similar at about 3.3×10^{-4} eV/K, which is nearer to the measured shift of the absorption edge of the direct gap $CdGeP_2$, 4.4×10^{-4} eV/K, than to that of $ZnGeP_2$, 6.5×10^{-4}eV/K, section 6.5.3.

Both materials show the same type of structure at higher energy. Two positive peaks are observed near to 3eV and are well resolved in $ZnGeP_2$ at 5K. These are followed by a broad negative peak. These spectra may be compared to the structure observed by other reflectance methods and also the calculated reflectivity curves of de Alvarez and Cohen for $ZnGeP_2$, figure 6.3 (161). The calculated curves for parallel and perpendicular polarisations predict the shape observed in figure 6.14 with a room temperature zero cross over at 3.2eV. This structure arises from transitions at the N point of the Brillouin zone and is consistent with the results of similar calculations made by Poplavnoi (158). Table 6.3 shows the predicted reflectivity peaks compared to polarisation modulation and electroreflectance spectra. The wavelength modulation results of Petroff

(167) and the thermoreflectance results of Raudonis (186) are also shown for comparison. Results vary between the different experimental techniques so that a detailed analysis of shape of the spectra obtained from each method is probably required before further comparison can be made.

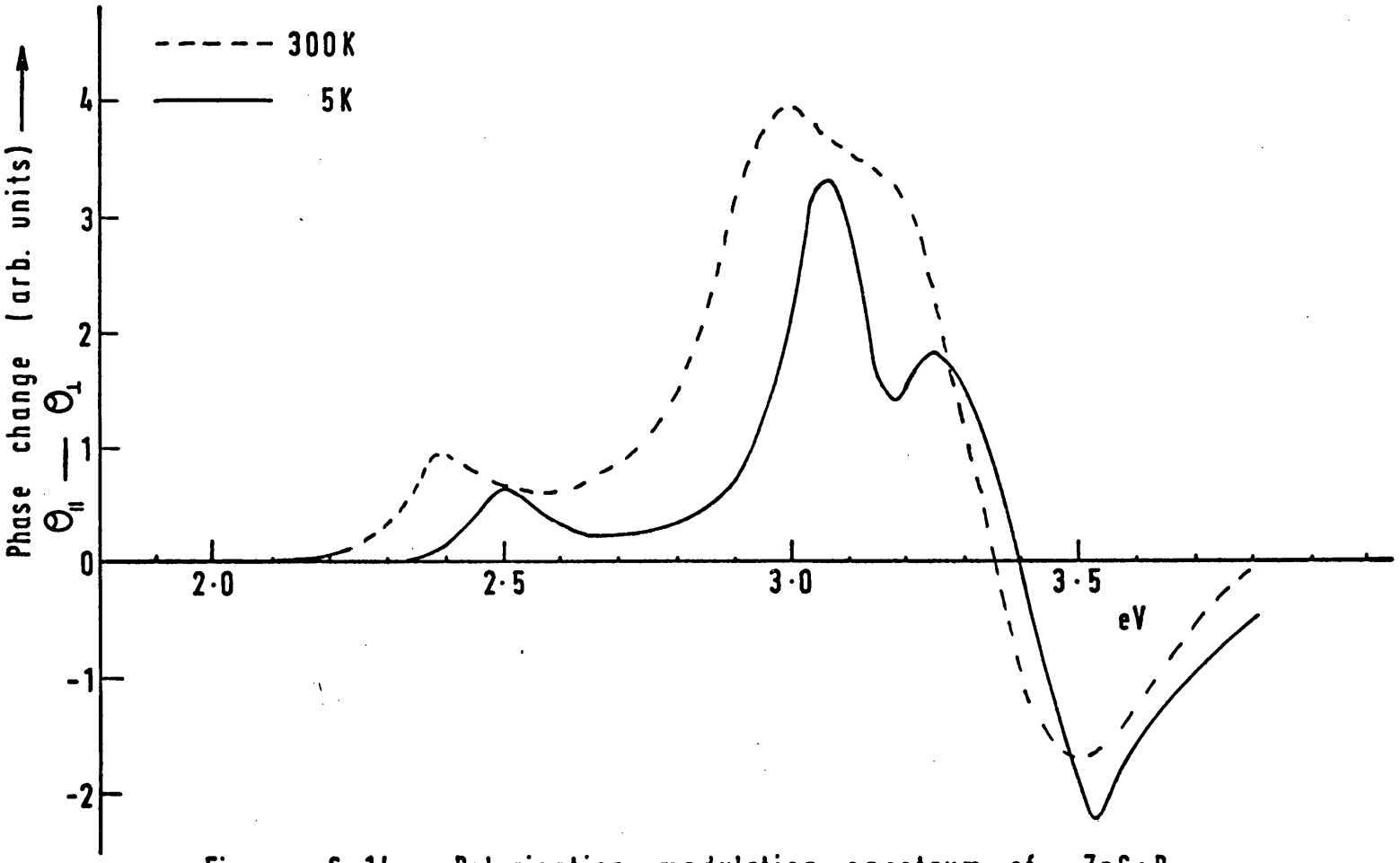

Figure 6.14 Polarisation modulation spectrum of $ZnGeP_2$

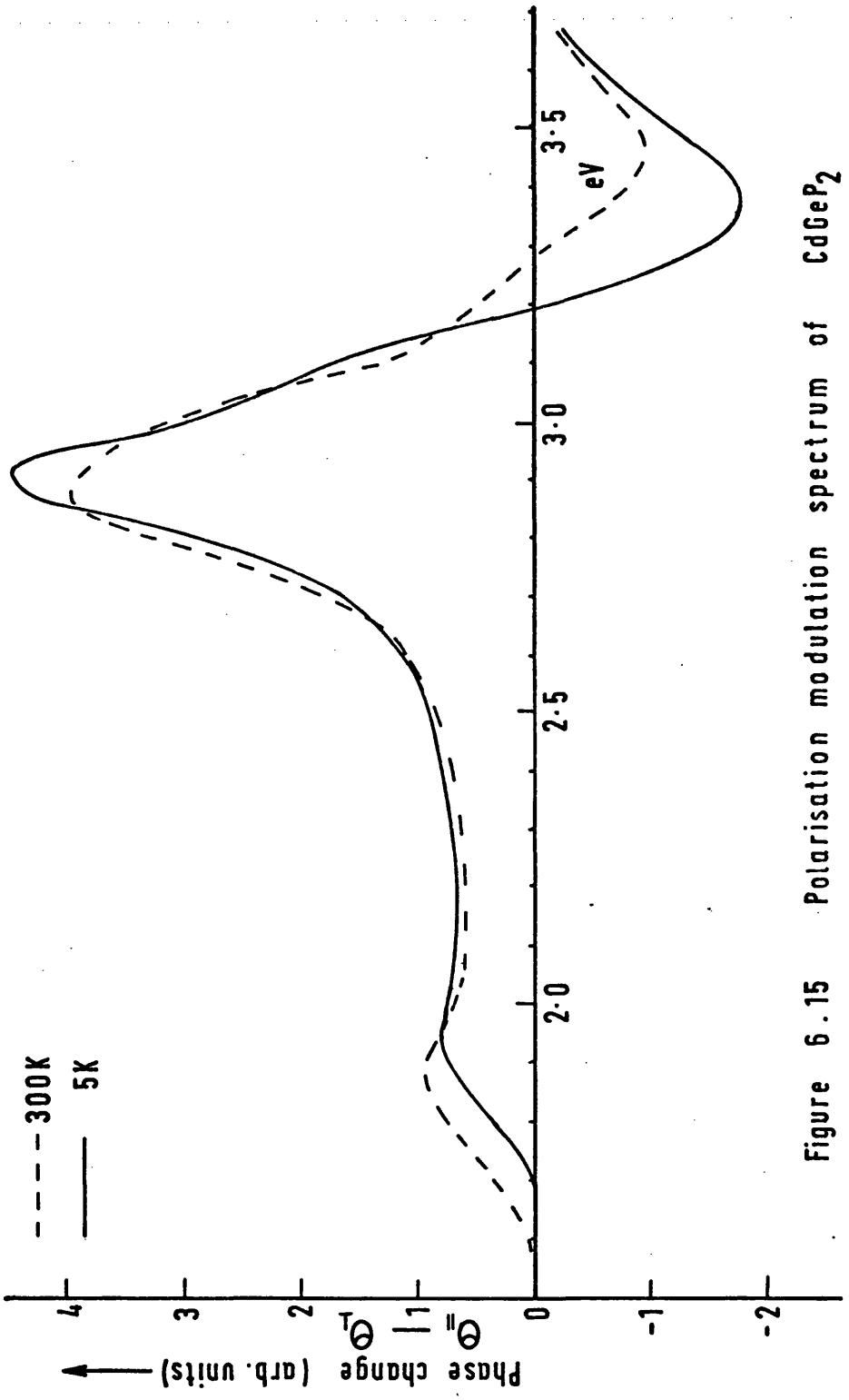

Figure 6.15 Polarisation modulation spectrum of $CdGeP_2$

Table 6.3 Higher energy structure in $ZnGeP_2$ (eV)

Theory (161)	Theory (158)	Pol.mod. 5K	Pol.mod. 300K	El.refl.(6.4.3) 300K	Wave.mod.(167) 5K	Thermoref.(186) 120K	Thermoref.(186) 300K
3.05		3.06 ||	3.01	2.86 ||	3.02 3.03	3.02 || ⊥	2.97
				2.91 ⊥	3.08(v.weak)	3.15 ⊥	3.09
	3.26	3.26 ||	3.15		3.20	3.22 ||	3.13
3.36 ⊥							
3.37 || ⊥					3.41		
3.45 || ⊥						3.48 ⊥ (||)	3.41
	3.52	3.52 ⊥	3.49				
3.75					3.74	3.75	3.71

CHAPTER 7 Conclusions

7.1 Growth and Crystal assessment

The solution growth method described in Chapter 2 produced single crystals which were large enough for optical and electrical measurements. The room temperature lattice parameters agreed well with published values. Small discrepancies may be caused by variations from stoichiometry. Large faces were of type {112} and {101}, which have the disadvantage that light reflected from them cannot be completely polarised parallel to the c-axis. However, this was not found to be a major problem in the interpretation of optical data. The resistivities of the materials were rather high, but much less than crystals grown from the melt. $ZnGeP_2$ was p-type which is consistent with all previous reports and so a self compensating mechanism may be inhibiting the formation of an n-type material. The acceptor activation energy of 0.206eV is lower than in other published work, indicating the introduction of a different defect or impurity in growth from lead solution. The acceptor activation energy of 0.202eV in $CdGeP_2$ is very near to that of $ZnGeP_2$ and is thus likely to be associated with a similar defect. The transition from p-type to n-type conduction in $CdGeP_2$ makes this material interesting for further study and may mean that the type of majority carrier at room temperature could be easily controlled by doping. This gives the possibility of the growth of a p-n homo-junction which has not been achieved in a II-IV-V_2 compound to date.

Larger crystals of both materials have been reported recently (32, 33) in the literature. These have been grown from the melt by directional cooling. The aim here was to grow crystals large enough for nonlinear optical applications, but the method may also produce

crystals large enough for the study of lattice dynamics by neutron scattering. The solution method used in this work is unlikely to produce crystals appreciably larger than those already obtained unless an effort is made to control the random nucleation of the crystals on the ampoule walls. This might be possible by either seeding or local cooling. The solubility of both materials in lead should also be investigated to determine the optimum slow cooling rate.

The results of the high temperature lattice parameter determination in $ZnGeP_2$ are interesting and this is worth extending to other chalcopyrite materials. No evidence of the solid state phase transition reported from differential thermal analysis was observed. The increase in the tetragonal compression with temperature could be explained in terms of the different thermal expansions of the II-V and IV-V bonds. It would be interesting to study a material in which a solid state phase transition is observable to give the change in the tetragonal compression just below the transition to zinc blende. Some useful knowledge may also be gained by studying the compounds $ZnSnP_2$ and $ZnSnAs_2$, which have no tetragonal compression at room temperature.

7.2 Lattice dynamics

Infrared reflection and Raman scattering measurements have now been made on five II-IV-V_2 compounds. The results have been interpreted in terms of Γ , X and W modes of their III-V analogues, which become zone centre modes in chalcopyrite. This predicts nine infrared active modes, six with E irreducible representation and three with B_2 irreducible representation.

In the infrared, $ZnGeP_2$ showed four E modes and two B_2 modes.

The missing modes were low frequency vibrations corresponding to zone boundary acoustic modes in GaP. $CdGeP_2$ spectra were similar except that one of the low frequency E modes was observed in this case.

A_1, B_1, B_2 and E modes are Raman active in chalcopyrite, predicting thirteen observable modes. In $CdGeP_2$, the complete spectrum was observed while in $ZnGeP_2$, one low energy B_2 mode and one high energy E mode were missing.

Table 7.1 shows the frequencies of the modes observed in $ZnGeP_2$ and $CdGeP_2$, and for comparison, the frequencies of the other compounds studied, $ZnSiP_2$ (101, 60), $CdSiP_2$ (121) and $ZnSiAs_2$ (120). The transverse frequencies are used to represent the polar modes. It is interesting to compare the frequencies of equivalent modes with the assumption that the modes are very near to the normal modes of the III-V analogues. It must be remembered however, that modes with the same irreducible representation may be mixed to an appreciable degree.

The unique A_1 mode is the simplest to compare as it corresponds to a motion of only the group V atoms. The frequencies are close in the phosphides, but lower in $ZnSiAs_2$ due to the heavier arsenic atom. The frequency of this mode in GaP was calculated to be $324.5cm^{-1}$(104). If $ZnSiP_2$ is compared to $ZnSiAs_2$, the distribution of the frequencies of the modes is very similar, but the magnitudes are all displaced to lower values.

The low frequency modes of the phosphides, such as $E(X_5)$ and $B_1(W_2)$ are seen to be comparable in the two cadmium compounds and in the two zinc compounds showing as expected the dominance of the heavier masses in these acoustic-like modes. On the other hand, the high frequency motions can be compared in the two germanium

Table 7.1 Frequencies (cm^{-1}) of modes in 5 II-IV-V_2

irrep.	z.b.	$ZnGeP_2$	$CdGeP_2$	$ZnSiP_2$	$CdSiP_2$	$ZnSiAs_2$
A_1	W_1	328	321	344	-	202
B_1	W_2	120	85	131	88	109
	X_3	247	255	-	-	-
	W_2	389	373	-	-	-
	W_2	-	88	-	111	149
B_2	W_2	343	299	347	305	242
	Γ_{15}	396	391	491	486	389
	X_5	94	63	105	-	75
	W_4	141	121	185	155	131
E	W_3	203	183	260	252	207
	X_5	303	291	320	284	233
	W_4	369	354	477	452	-
	Γ_{15}	386	383	500	486	400

compounds and in the two silicon compounds. These antiphase, optic vibrations will be mostly a motion of the lightest atoms. Since the Γ_{15} motion in $CdGeP_2$ will be mostly the displacement of the phosphorus atoms, the germanium contribution being smaller and the cadmium very small, the frequency is fairly close to the frequency of the A_1 phosphorus motion.

One of the effects of the perturbation in going from the zinc blende to the chalcopyrite structure is the splitting of the W_2 modes with B_1 and B_2 representations. This splitting gives an indication of the difference between the strengths of the II-V and IV-V bonds of $ZnGeP_2$ in which the masses of zinc and germanium are close. The two modes are similar except that in the B_1 mode, the phosphorus moves towards two zinc atoms or two germanium atoms while in the B_2 mode, the phosphorus moves towards a zinc and a germanium atom, figure 3.9. The low frequency B_2 (W_2) modes were not observed in $ZnGeP_2$ or $ZnSiP_2$ which may mean that they could not be resolved from the stronger $B_1(W_2)$ mode. The other three compounds show an appreciable splitting. The $B_1(W_2)$ high frequency modes were only observed in $ZnGeP_2$ and $CdGeP_2$ and show a considerable splitting from the $B_2(W_2)$ modes.

Further progress in the interpretation of these results awaits a quantitative model to predict the frequencies of the modes from known values of the atomic masses and trial force constants and ionic charges. The number of parameters required would be quite large, and so the most straightforward method may be to extend an existing model for the III-V analogues. More experimental information at other points in the Brillouin zone away from the zone centre may be obtained from neutron scattering when crystals of suitable size and quality are available. Other II-IV-V_2 compounds may be investigated

by the infrared reflectivity technique, but Raman measurements are limited by the availability of lasers in the transmission region of the lower band gap materials. The second order Raman scattering of the five materials already studied and also two phonon absorption may be measured to obtain information at $\underline{k} \neq 0$ now that the frequencies of most of the zone centre modes are known.

7.3 Electronic band structure

Embedding the energy band structure of zinc blende compounds into the smaller chalcopyrite Brillouin zone gives a general understanding of the band structure of II-IV-V_2 compounds. Spin-orbit and crystal field effects on the upper valence bands give three direct zone centre transitions. The lowest conduction bands consist of zone centre bands of zinc blende and also X and W zone boundary bands of the analogues. Two types of energy band gap result. A direct gap is obtained when the lowest band is the zone centre energy band of the analogue, and an indirect or pseudo-direct gap is obtained when a band deriving from the X-point of the analogue is the lowest.

The results of absorption and electroreflectance measurements in the region of the lowest direct transition show the nature of the band gap for a particular material. $CdGeP_2$ showed a steeply rising edge, figure 6.12, very close to the lowest direct transition shown in electroreflectance at 1.7eV, figure 6.8. This is a general feature of direct gap semiconductors and is the expected result from consideration of the energy band structure of the analogue, $Ga_{0.5}\ In_{0.5}\ P$. On the other hand, $ZnGeP_2$ has an indirect analogue, GaP, with its lowest minimum in the X direction. The observed absorption edge in $ZnGeP_2$, figure 6.11, was much less steep and has reached 200 cm^{-1} by 0.4eV below the first direct transition observed

in electroreflectance, figure 6.7. No evidence of the pseudodirect transitions were observed in electroreflectance and whether the pseudodirect gap at Γ , or the indirect gap at T is the smaller could not be determined from absorption measurements. An investigation of the anisotropy of the effective electron mass could determine this.

The electroreflectance method also gave structure at energies above the band gap in $ZnGeP_2$. The experimental limit on observation was at 3.1eV, and up to this energy two peaks were observed with opposite polarisations of the incident light. More information in this region was obtained from polarisation modulation, figures 6.14 and 6.15. The results of this technique may be easier to interpret for theoretical investigations of the energy band structure, as it can give the difference in the reflectivity of light polarised parallel and perpendicular to the c-axis. This can be calculated from a theoretical band structure, whereas an active modulation technique such as electroreflectance requires a detailed analysis of the processes involved to obtain values of the optical constants of the material. In fact, the polarisation modulation results can be compared with the theoretical reflectivity spectrum for $ZnGeP_2$ by de Alvarez and Cohen (161), and they show general agreement. It thus seems likely that the structure in this region arises from transitions at the N point of the Brillouin zone.

The general features of the optical properties of these two compounds are consistent with measurements on other II-IV-V_2 compounds. $ZnSiP_2$, $CdSiP_2$, $MgSiP_2$ and $ZnSiAs_2$ have shown absorption edges similar to $ZnGeP_2$ while all materials with band gaps lower than $CdGeP_2$ are generally believed to be direct. Further progress may be made by studying the effect on the optical properties in a magnetic field.

$CdGeP_2$ has a larger direct band gap than any of the III-V compounds, apart from the nitrides. As $CdGeP_2$ can be grown both

p-type and n-type, the possibility of a useful light emitting diode exists although $CdGeP_2$ has not yet been reported to emit light by photoluminescence or by cathodoluminescence due to interband transitions.

The alloy system between $ZnGeP_2$ and $CdGeP_2$ would be useful for study of the intermediate band structure if growth difficulties could be overcome. The transition from a direct gap to either an indirect or a pseudo-direct gap may give more information on the structure at the bottom of the conduction band in $ZnGeP_2$. It may also produce a direct gap material with an energy in the red or orange region of the spectrum.

APPENDIX A

$\bar{I}42d$ space group translations,

$$E = \{ x, y, z \mid 0 \}$$

$$C_2 = \{ \bar{x}, \bar{y}, z \mid 0 \}$$

$$S_4^a = \{ \bar{y}, x, \bar{z} \mid 0 \}$$

$$S_4^b = \{ y, \bar{x}, \bar{z} \mid 0 \}$$

$$C_2^{a/} = \{ \bar{x}, y, \bar{z} \mid \underline{\tau} \}$$

$$C_2^{b/} \{ x, \bar{y}, \bar{z} \mid \underline{\tau} \}$$

$$\sigma_d^a = \{ y, x, z \mid \underline{\tau} \}$$

$$\sigma_d^b = \{ \bar{y}, \bar{x}, z \mid \underline{\tau} \}$$

where $\underline{\tau} = \frac{a}{2} (0, 1, 1)$

APPENDIX B

Raman selection rules for backscattering configuration from a (101) face with a 30° angle of incidence and scattered light collected normal to the crystal face

irrep.	$\perp\perp$	$\perp\parallel$	$\parallel\perp$	$\parallel\parallel$
A_1	$0.98a^2$	$(-0.068a+0.062b)^2$	$0.0001a^2$	$(0.177a+0.820b)^2$
B_1	$0.98c^2$	$0.000462c^2$	$0.0001c^2$	$0.0313c^2$
B_2	$0.023d^2$	$0.2d^2$	$0.15d^2$	$0.00003d^2$
E(y)	0	$0.01e^2$	0	$0.59e^2$
E(x)	$0.005e^2$	$0.778e^2$	$0.846e^2$	$0.00008e^2$

REFERENCES

1. J. Bardeen, W.H. Brattain Phys. Rev. 74 230 (1948)

2. A.N. Blum, N.P. Mokrovskii, A.R. Regel
Seventh All-Union Conference on the Prop. of Semicond. (Kiev, 1950).

3. N.A. Goryunova, A.P. Obukhov
Seventh All-Union Conference on the Prop. of Semicond. (Kiev, 1950).

4. H.G. Grimm, A. Sommerfeld Z. Physik 36 36 (1926)

5. H. Hahn, G. Frank, W. Kingler, A. Meyer, G. Storger
Z. Anorg, Allg. Chem. 271 153 (1953).

6. C.H.L. Goodman Nature 179 828 (1957).

7. C.H.L. Goodman J. Phys. Chem. Solids 6 305 (1958)

8. N.A. Goryunova The Chemistry of Diamond-like Semiconductors.
Ed. J.C. Anderson, M.I.T. Press, Cambridge Mass. (1965).

9. A.S. Borshchevskii, N.A. Goryunova, F.P. Kesamanly, D.N. Nasledov
Phys. Status Solidi 21 9 (1967).

10. N.A. Goryunova, A.S. Poplavnoi, Yu. I. Polygalov, V.A. Chaldeshev
Phys. Status, Solidi 39 9 (1970).

11. U. Kaufmann, J. Schneider
Festkörperprobleme XIV p.229, Stuttgart (1974).

12. R.C.J. Draper, A. Miller, R.G. Humphreys
1st Inter. Conf. on ternary semiconducting compounds (Bath 1973).

13. B. Ray J. Mater. Sci. 2 284 (1967)

14. J.L. Shay, J.H. Wernick
Ternary chalcopyrite semiconductors - Growth, electronic properties and applications (Pergamon, New York, 1974)

15. S.C. Abrahams, J.L. Bernstein
J. Chem. Phys. 52 5607 (1970)

16. S.C. Abrahams, J.L. Bernstein
J. Chem. Phys. 55 796 (1971)

17. S.C. Abrahams, J.L. Bernstein
J. Chem. Phys. 61 1140 (1974)

18. M.D. Lind, R.W. Grant
J. Chem. Phys. 58 357 (1973)

19. R. Grigorovici, R. Mănăilă
Acta Cryst. B24 535 (1968)

20. L. Pauling, M.H. Huggins
Z. Krist. 87 205 (1934)

21. J.A. Van Vechten, J.C. Phillips
Phys. Rev. B2 2160 (1970)

22. J.C. Phillips J. Phys. Chem. Solids 35 1205 (1974)

23. J.C. Phillips Covalent bonding in crystals, molecules and polymers, p 232.
Univ. of Chicago Press, Chicago.

24. C. Varae de Alvarez, M.L. Cohen, L. Ley, S.P. Kowalczyk, F.R. McFeely, D.A. Shirley, R.W. Grant.
Phys. Rev. B 10 596 (1974)

25. B.F. Levine J. Chem. Phys. 59 1463 (1973)

26. J.C. Phillips Rev. Mod. Phys. 42 317 (1970)

27. J.A. Van Vechten Phys. Rev. 182 891 (1969)

28. B.F. Levine Phys. Rev. B 7 2600 (1973)

29. D.B. Gasson, P.J. Homes, I.C. Jennings, B.R. Marathe, J.E. Parrott J. Phys. Chem. Solids 23 1291 (1962)

30. O.G. Folberth, H. Pfister Acta Cryst. 14 325 (1961)

31. A.A. Vaipolin, E.O. Osmanov, D.N. Tret'yakov
Inorganic Mater. 3 231 (1967)

32. E. Buehler, J.H. Wernick, J.D. Wiley
J. Electronic Mater. 2 445 (1973)

33. E. Buehler, J.H. Wernick
National Bureau of Standards Special Publ. 364, Solid State chemistry, Proc. 5th. Mater. Res. Symp.(1972)

34. K. Masumoto, S. Isomura, W. Goto
J. Phys. Chem. Solids 27 1939 (1966)

35. C.C.Y. Kwan, J.C. Woolley
Can. J. Phys. 48 2085 (1970)

36. P. Leroux - Hugon J. Phys. Chem. Solids 27 1205 (1966)

37. R.S. Fiegelson Proc. 2nd. Amer. Nat. Conf. Crystal Growth p. 69(Princeton, N.J. 1972)

38. B.J. Curtis, P. Wild Mat. Res. Bull. 5 69 (1970)

39. A.J. Springthorpe, B.R. Pamplin
J. Cryst. Growth 3 313 (1968).

40. Y.A. Valov Izv. Akad. Nauk SSSR Neorg. Mater
5 1802 (1969)

41. B. Ray, A.J. Payne, G.J. Burrell.
Phys. Status. Solidi 35 197 (1969)

42. S.A. Mughal Ph. D. thesis University of St. Andrews(1971)

43. N.A. Goryunova, V.I. Sokolova, Bin-si Tszyan
Dokl.Akad. Nank. SSSR 152 363 (1963)

44. E.H. Turner, E. Buehler, H. Kasper
Phys. Rev. B 9 558 (1974)

45. S. Knight, E. Buehler, I. Cantibel
J. Appl. Phys. 43 3422 (1972)

46. N.A. Goryunova, E.I. Leonov, V.M. Orlov, L.F. Rodionov,
V.P. Sandaevskii ZETP Letters 12 459 (1970).

47. M.V. Hobden Acta Cryst. A 24 676 (1968)

48. V.A. Chaldeshev, B. N. Pokrovskii
Izv. Viz. Fiz. 2 173 (1960).

49. V.A. Chaldeshev, F.G. Karavaev
Izv. Viz. Fiz. 5 103 (1963)

50. D.A. Kleinman, W.G. Spitzer Phys. Rev. 118 110 (1960).

51. B.A. Weinstein, M. Cardona Phys. Rev. B8 2795 (1973)

52. A.S. Borshchevskii, Yu. A. Valov, N.A. Goryunova, E.O. Osmanov,
S.M. Ryvkin, G.P. Shpenkov. Sov. Phys. Semicond. 2 1145 (1968)

53. J.L. Shay, W.D. Johnston, E. Buehler, J.H. Wernick
Phys. Rev. Lett. 27 711 (1971)

54. J.L. Shay, K. Bachmann, E. Buehler, J.H. Wernick
App. Phys. Lett. 5 226 (1973)

55. G.D. Boyd, E. Buehler, F.G. Storz
App. Phys. Lett. 18 301 (1971)

56. G.D. Boyd, E. Buehler, F.G. Storz, J.H. Wernick
IEEE J. Quant. Electron 8 419 (1972)

57. G.D. Boyd, H.M. Kasper, J.H. McFee, F.G. Storz
IEEE J. Quant. Electron. 8 900 (1972)

58. G.D. Boyd, W.B. Gandrud, E. Buehler
App. Phys. Lett. 18 446 (1971)

59. G.D. Boyd, T.J. Bridges, C.K.N. Patel, E. Buehler
App. Phys. Lett 21 553 (1972)

60. G.D. Holah J. Phys. C 5 1893 (1972)

61. J. Gelbwachs, R.H. Pantell, H.E. Puthoff, J.M. Yarborough
App. Phys. Lett. 14 258 (1969)

62. S.A. Mughal, A.J. Payne, B. Ray
J. Mater. Sci. 4 895 (1969)

63. A.A. Vaipolin, F.M. Gashimzade, N.A. Goryunova,
F.P. Kesamanly, D.N. Nasledov, E.O. Osmanov, J.V. Rud.
Izv. Akad. Nauk. SSSR Fiz. 28 1085 (1964)

64. A.S. Borshchevskii, A.A. Vaipolin, S.G. Konnikov,
N.K. Takhtareva, Yu. K. Undalov.
Inorganic Mater. 9 506 (1973)

65. E. Buehler, J.H. Wernick
J. Cryst. Growth 8 324 (1971)

66. J.D. Wiley, E. Buehler, J.L. Shay, J.H. Wernick
J. Electronic Mater. 2 601 (1973)

67. I.I. Tychina, V.G. Fedotov, I.M. Ivanova
Chemical bonds in solids Vol. 4 p.158
Ed. N.N Sirota (Consultants Bureau 1972)

68. I.M. Ivanova, E.K. Ivanov, L.B. Zlatkin, V.D. Prochukhan
Sov. Phys. Semicond. 3 1587 (1970)

69. A.L. Gentile, O.M. Stafsudd
Mat. Res. Bull. 9 105 (1974)

70. B. Ray, S.A. Mughal, A.J. Payne
Thermal analysis 2 Proc. 3rd ICTA (Davos 1971)

71. I. Bertoti, K. Somogyi
Phys. Status Solidi (a) 6 439 (1971)

72. A.S. Borshchevskii, Yu. V. Rud, Yu. K. Undalov
Sov. Phys. Semicond. 7 1047 (1974)

73. J.J. Gilman The art and science of crystal growth
(Wiley, N.Y., 1963)

74. E.E. Alekperova Izv. Akad. Nauk. Neorg. Mater.
5 146 (1969)

75. H.J. Scheel, E.O. Schulz - Dubois
J. Cryst. Growth 8 304 (1971)

76. B.R. Pamplin, R.C.J. Draper, R.G. Humphreys.
Mat. Res, Bull, to be published.

77. International critical tables for X-ray crystallography Vol. 1 p. 212 (Kynock, Birmingham, 1952).

78. J.B. Nelson, D.P. Riley
Proc. Phys. Soc. (London) 57 160 (1945)

79. Y.L. Lee Ph. D. thesis, Bath University (1970).

80. Y.A. Valov, N.A. Goryunova, E.I. Leonov, V.M. Orlov
Act. Phys. Acad. Sci. Hung. 33 1 (1973).

81. A.A. Vaipolin Sov. Phys. Solid State 15 965 (1973)

82. R.G. Humphreys Private communication

83. H. Welker, H. Weiss Solid State Physics Vol. 3 p.51
(Ed. Seitz and Turnbull, Acad. Press, 1956)

84. S.I. Novikova Semiconductors and Semimetals Vol. 2 p. 33
(Ed. Willardson and Beer, Acad. Press, 1966)

85. L.J. Van der Pauw Phillips Res. Repts. 13 1 (1958)

86. R.A. Smith Semiconductors
(Cambridge University press, 1959)

87. S. Isomura, K. Masumoto Phys. Status Solidi (a) 13
223 (1972)

88. K. Somogyi, I. Bertoti
Jap. J. Appl. Phys. 11 103 (1972)

89. K. Somogyi Phys. Status Solidi (a) 18 K95 (1973)

90. O.V. Emelyanenko, I.K. Polushina
Phys. Status Solidi 36 K13 (1969)

91. H.N. Leifer, W.C. Dunlap
Phys. Rev. 95 51 (1954)

92. J.S. Blakemore Solid State Physics
(Saunders Company, 1970)

93. M. Born, K. Huang Dynamical theory of crystal lattices,
(Oxford University press, 1954)

94. F.A. Johnson Progress in semiconductors 9 181 (1965)

95. F.A. Johnson, W. Cochran
Proc. Int. Conf. on the Phys. of Semicond, p.498
(Exeter 1962)

96. R. Tubino, L. Piseri, G. Zerbi
J. Chem. Phys. 56 1022 (1972)

97. J.L.T. Waugh, G. Dolling
Phys. Rev. 132 2410 (1963)

98. J.L.T. Waugh, G. Dolling Lattice dynamics, p 19
Proc. Int. Conf. (Copenhagen, 1963)

99. J.L. Yarnell, J.L. Warren, R.G. Wenzel, P.J. Dean
Neutron inelastic scattering, Vol 1, p 301
(IAEA, Vienna, 1968).

100. R.M. Martin Phys. Rev. B 1 4005 (1970).

101. I.P. Kaminow, E. Buehler, J.H. Wernick
Phys. Rev. B 2 960 (1970).

102. G. Nilsonn, G. Nelin Phys. Rev. B 3 364 (1971)

103. M. Bettini Ph.D. Thesis, University of Stuttgart (1974)

104. M. Bettini, A. Miller Phys. Status Solidi (b)
in press, December 1974.

105. Von R. Sandrock, J.Treusch
Z. Naturforschg. 19 a 844 (1964)

106. R. Loudon Adv. Phys. 13 432 (1964)

107. G.F. Karavaev, A.C. Poplavnoi, B.G. Tyuterev.
Sov. Phys. J. 10 42 (1970)

108. G.D. Holah, J.S. Webb, H. Montgomery
J . Phys. C. in press, November 1974.

109. H. Montgomery Proc. Roy. Soc. A 309 521 (1969)

110. L.B. Zlatkin, Yu. F, Markov, A.I. Stekhanov, M.S. Shur
Phys. Status. Solidi 32 473 (1969)

111. N.A. Goryunova, L.B. Zlatkin, Yu. F. Markov, A.I. Stekhanov,
M.S. Shur. Sov. Phys. Solid State 10 1782 (1969)

112. L.B. Zlatkin, Yu. F. Markov, A.I. Stekhanov, M.S. Shur
J. Phys. Chem. Solids, 31 567 (1970)

113. N.A. Goryunova, L.B. Zlatkin, Yu. F. Markov, A.I. Stekhanov
Sov. Phys. - Dokl. 14 72 (1969)

114. N.A. Goryunova, E.F. Gross, L.B. Zlatkin, E.K. Ivanov
J. Non-Crystalline solids 4 57 (1970)

115. L.B. Zlatkin, Yu. F. Markov, V.M. Orlov, V.I. Sokolova
M.S. Shur Sov. Phys. Semicond. 4 1181 (1971)

116. N.S. Boltovets, B. Kh. Mamedov, É.O. Osmanov
Sov. Phys. Semicond. 4 499 (1970).

117. L.B. Zlatkin, Yu. F. Markov
Opt. and Spectrosc. 32 403 (1972)

118. Yu. F. Markov, N.B. Reshetnyak
Opt. and Spectrosc. 33 280 (1972).

119. Yu. F. Markov, V.S. Grigoreva, B.S. Zadokhin, T.V. Rybakova
Opt. and Spectrosc. 36 93 (1974)

120. W.H. Koschel, F. Sorger, J. Baars
Solid State Comm. 15 719 (1974)

121. M. Bettini W. Bauhofer, M. Cardona, R. Nitsche
Phys. Status Solidi (b) 63 641 (1974)

122. G.C. Bhar, R.C. Smith
Phys. Status Solidi (a) 13 157 (1972)

123. A. Miller, G.D. Holah, W.C. Clark
1st Int. Conf. on ternary semiconductors, (Bath 1973)

124. A. Miller, G.D. Holah, W.C. Clark
J. Phys. Chem. Solids 35 685 (1974).

125. G.D. Holah, J.S. Webb
Proc. Int. Conf. on Semicond. (Warsaw 1972)

126. G.D. Holah Opt. Comm. 5 10 (1972)

127. J. Baars, W.H. Koschel Solid State Comm. 11 1513 (1972)

128. J.P. Van der Ziel, A.E. Meixner, H.M. Kasper,
J.A. Ditzenburger Phys. Rev. B 9 4286 (1974)

129. W.H. Koschel, V. Hohler, A. Rauber, J. Baars
Solid State Comm. 13 1011 (1973).

130. T.S. Moss, G.J. Burrel, B. Ellis, Semiconductor Opto-electronics
(Butterworths, London, 1973)

131. H.W. Bode Network analysis and feedback amplifier design
(Van Nostrand, New York, 1945)

132. T.S. Robinson Proc. Phys. Soc. (London) B65 910 (1952)

133. G. Peckham Computer J. 13 418 (1970).

134. R.H. Lyddane, R.G. Sachs, E. Teller
Phys. Rev. 59 673 (1941)

135. L. Merten Z. Naturf. A 15 47 (1960)

136. L. Merten Z. Naturf. A 17 65 (1960)

137. W. Cochran, R.A. Cowley J. Phys. Chem. Solids 23 447 (1962)

138. B. Szigetti Trans. Far. Soc. 45 155 (1949)

139. B. Szigetti Proc. Roy. Soc.(London) A 204 51 (1950)

140. M. Hass Semiconductors and semimetals Vol. 3 p.3 (Ed. Willardson and Beer, Acad. Press 1967).

141. T. Hidaka J. Phys. Soc. Jap. 36 800 (1974)

142. J.J. Hopfield Phys. Rev. 112 1555 (1958)

143. C.V. Raman, K.S. Krishnan Nature 121 501 (1928)

144. C.V. Raman, K.S. Krishnan Proc. Roy. Soc. (London) A 122 23 (1928)

145. C.V. Raman Indian J. Phys. 2 387 (1928)

146. Smekal Naturwissenschaften 11 873 (1923)

147. R. Loudon Proc. Roy. Soc. A275 218 (1963)

148. M. Born, M. Bradburn, Proc. Roy. Soc. A188 161 (1947)

149. C.G.B. Garrett J. Quant. Electron 4 70 (1968)

150. A.S. Barker Far infrared properties of solids (Ed. Mitra and Nudelman, Plenum press, 1970).

151. A. Nussbaum Applied group theory for chemists, physicists and engineers (Prentice-Hall, 1971)

152. P.N. Keating Phys. Rev. 145 637 (1966)

153. C. Albert, G. Bordure, A. Laugier, J. Chevallier Phys. Rev. B 6 1301 (1972)

154. R.H. Parmenter Phys. Rev. 100 573 (1955)

155. J.J. Hopfield J. Phys. Chem. Solids 15 97 (1960)

156. J.E. Rowe, J.L. Shay Phys. Rev. B 3 451 (1971)

157. A.S. Poplavnoi, Yu. I. Polygalov, V.A. Chaldeshev Izv. Vys. Ucheb. Zaved. SSSR. Fiz. 11 58 (1969)

158. A.S. Poplavnoi, Yu. I. Polygalov, V.A. Chaldeshev Izv. Vys. Ucheb. Zaved. SSSR Fiz. 6 95 (1970)

159. A.S. Poplavnoi, Yu. I. Polygalov, V.A. Chaldeshev Izv. Vys. Ucheb. Zaved. SSSR Fiz 7 17 (1970).

160. D.J. Morgan Phys. Status Solidi (b) 48 771 (1971)

161. C. Varae de Alvarez, M.L. Cohen Phys. Rev. Lett. 30 979 (1973).

162. S.E. Stokowski Phys. Rev. B 6 1294 (1972)

163. J. Kavaliauskas, G.F. Karavaev, E.I. Leonov, V.M. Orlov, V.A. Chaldeshev, A. Shileika. Phys. Status Solidi (b) 45 443 (1971).

164. J.L. Shay Phys. Rev. Lett 29 1008 (1972)

165. R. Bendorius, V.D. Prochukhan, A. Šileika
Phys. Status Solidi (b) 53 745 (1972)

166. V.V. Sobolev, V.I. Donetskikh
Sov. Phys. Solid State 12 2183 (1971)

167. Y. Petroff, S. Kohn, Y.R. Shen
Proc. 1st. Int. Conf. Modulation Spectroscopy, Arizona. Surface Science 37 540 (1973).

168. J.L. Shay, B. Tell, E. Buehler, J.H. Wernick
Phys. Rev. Lett. 30 983 (1973)

169. J.L. Shay, E. Buehler, J.H. Wernick
Phys. Rev. B 4 2479 (1971)

170. J.L. Shay, E. Buehler, J.H. Wernick
Phys. Rev. Lett. 24 1301 (1970)

171. J.L. Shay, E. Buehler, J.H. Wernick
Phys. Rev. B 2 4104 (1970)

172. J.L. Shay, E. Buehler
Phys. Rev. Lett. 26 506 (1971)

173. J.L. Shay, E. Buehler
Phys. Rev. B 4 2479 (1971)

174. J.L. Shay, E. Buehler, J.H. Wernick
Phys. Rev. B 3 2004 (1971)

175. J.L. Shay, E. Buehler
Phys. Rev. B 3 2598 (1971)

176. G.Z. Krivaite, A. Yu. Šileika
Sov. Phys. Semicond. 7 1198 (1974)

177. G.Z. Krivaite, L.V. Kradinova
Sov. Phys. Semicond. 6 1945 (1973)

178. G.Z. Krivaite, E.F. Korneev, A. Yu. Šileika
Sov. Phys. Semicond. 5 1961 (1972)

179. I.P. Akimchenko, V.S. Ivanov, A.S. Borshchevskii
Sov. Phys. Semicond. 7 309 (1973)

180. J. Kavialaskas, S.P. Vul, A. Yu. Šileika
Sov. Phys. Semicond. 5 1925 (1972)

181. F.G. Karavaev, G.Z. Krivaite, Yu. I. Polygalov, V.A. Chaldyshev, A. Yu. Šileika
Sov. Phys. Semicond. 6 1863 (1973)

182. G.Z. Krivaite Phys. Status Solidi 57(b) K39 (1973)

183. C.C. Y. Kwan, J.C. Woolley
App. Phys. Lett. 18 520 (1971)

184. C.C.Y. Kwan, J.C. Woolley
Phys. Status, Solidi(b) 44 K93 (1971)

185. C.C.Y. Kwan, J.C. Woolley
Can. J. Phys. 48 2085 (1970)

186. A. Raudonis, V.S. Grigoreva, V.D. Prochukhan,
A. Šileika. Phys. Status Solidi (b) 57 415 (1973)

187. G. Babonas, G. Ambrazevičius, V.S. Grigoreva, V. Neviera,
A. Šileika.
Phys. Status Solidi(b) 62 327 (1974)

188. I.S. Gorban, I.P. Zharkov, V.V. Lugovskii
I.I. Tychina, V.I. Seryi
Sov. Phys. Solid State 15 1497 (1974)

189. M. Bettini Solid State Comm. 13 599 (1973)

190. M. Cardona Solid State Physics Suppl. 11, Modulation spectroscopy
(Ed. Seitz and Turnbull, Acad. press, 1969)

191. Willardson and Beer Semiconductors and semimetals Vol. 9
Modulation techniques (Acad.press, 1972)

192. W. Franz Z. Naturforsch. 13 484 (1958)

193. L.V. Keldysh, Zh. Ekspermi
Sov. Phys. JETP 7 788 (1958)

194. D. Aspnes Phys. Rev. 147 554 (1966)

195. J.T. Law Semiconductors p.682
(Ed. N.B. Hannay, Reinhold Publ. Co., 1959)

196. M. Cardona, K.L. Shanklee, F.H. Pollak
Phys. Rev. 154 696 (1967)

197. J.C. Kemp J. Opt. Soc. Am.59 950 (1969).